L'impact du cratère du lac Bosumtwi : l'utilisation de la tomographie de la résistivité électrique (TRE) pour tracer la carte géométrique de la paroi internet du cr&tère et de l'impact associé à la structure

Akwasi Acheampong Aning

Département des Sciences de la Terre.
UMR 8148 IDES

Department of Physics, College of Science.

BOSUMTWI IMPACT CRATER: USE OF ELECTRICAL RESISTIVITY TOMOGRAPHY (ERT) TO MAP THE GEOMETRY OF THE INNER WALL OF THE CRATER AND THE IMPACT RELATED STRUCTURES

A dissertation by

Akwasi Acheampong Aning

Submitted to the

UNIVERSITÉ PARIS-SUD, FRANCE

for the degree of

Docteur de l'Université Paris-Sud

and

KWAME NKRUMAH UNIVERSITY OF SCIENCE AND TECHNOLOGY, GHANA

for the degree of

Doctor of Philosophy of KNUST

25th July, 2012

Subject: Geophysics

Directors of Thesis: Piotr Tucholka and Sylvester K. Danuor

JURY

TABBAGH Alain	Université Paris VI	Rapporteur
WILLIAMSON David	IRD/ICRAF, Nairobi	Rapporteur
MENYEH Aboagye	KNUST, Kumasi	Examiner
LEGTCHENKO Anatoly	IRD/LTHE, Grenoble	Examiner
BONINI Bernard	Université Paris XI	Examiner
TUCHOLKA Piotr	Université Paris XI	Director of thesis
DANUOR Sylvester K.	KNUST, Kumasi	Director of thesis

Dedication

This work is dedicated to Mercy, Adoma, Acheampong, Nti and Owusua.

Abstract

Electrical resistivity tomography (ERT) and geological field surveys have been used to map the sediment/bedrock contact and impact related structures of the 1.07 Myr old Bosumtwi impact crater. The 10.5 km complex crater excavated in 2.1–2.2 Gyr Precambrian metasedimentary and metavolcanic rocks is filled by the 8.5 km Lake Bosumtwi. It is the source crater of the tektites and microtektites of the Ivory Coast strewn field. Electrical resistivity survey was carried out sixteen (16) profiles running from the shore of the lake towards the rim of the crater. The multi-electrode gradient array method with minimum electrode separation of 5 m was used. The data were corrected for topography and inverted using the L_1–norm (robust inversion) technique of the Res2DInv software. The area extending from the lake shore towards the crater rim contains essentially three formations. The low resistivity regions (< 64 Ω.m) represent the lake sediments. The moderately high resistivity regions with values between 128 and 200 Ω.m were interpreted as impact related breccias (dikes, allochthonous or parautochthonous) depending on their geometries. Lastly, the model clearly differentiate the resistive basement metamorphic rocks (> 128 Ω.m) from the lake sediments and the breccias due to their geometry and lateral extent. Also observed was a direct correspondence between the lithology on the surface and the subsurface resistivity structures at Dwamam in the southeast section of the lake. At Dwamam, the sediments were about 200 m away from the shore and stretch about 400 m towards the crater rim unlike in other areas where the sediments were mapped from the shore. The gradient of the sediments/bedrock contact shows a symmetry in the NE–SW direction and dips between the lowest of 16^{o} in the NE to the highest 36^{o} in the SW. Majority of the fractures marked were in the southwest and were filled with clasts or impact breccia matrix. The faults were mostly delineated in the west. Averagely, the dips of the faults are about 60^{o} and 80^{o} for the east and west sections of the crater respectively. The dips of the faults were statistically treated using the von Mises and Fisher statistics, it was found that the faults have a preferred direction and it is possible to determine at least two different orientations. The analysis of the results of the sediments/bedrock surface and the faults combined with the location of the tektite strewn field indicate that the about 0.8–1 km bolide that created the complex crater came from the NE. The findings have shown that the ERT is efficient and a useful tool in impact cratering science research.

Keywords: Bosumtwi; Impact crater; Electrical resistivity tomography; Gradient array; Inversion

Résumé

Des mesures de résistivité électrique et des campagnes d'observations géologiques ont été menées pour cartographier le contact sédiment/roche basale ainsi que les structures d'impact associées au cratère d'impact Bosumtwi datant de 1,07 millions d'années. Le cratère de 10,5 km de diamètre s'est formé dans des roches métamorphiques du Précambrien (2,1 à 2,2 milliard d'années), d'origine sédimentaire et volcanique. Il est actuellement rempli par le lac Bosumtwi de 8,5 km de diamètre. Ce cratère est la source des tektites et microtektites dispersées jusqu'en Côte - d'Ivoire et au large des côtes ouest africaine. La campagne de mesures géophysiques consiste en 16 tomographies de résistivité électrique effectuées radialement des rives du lac vers les bords du cratère d'impact. Chaque profil utilise un système d'acquisition multi - électrodes avec une distance minimum entre les électrodes de 5 m. Les données ont été corrigées des effets topographiques et inversées en utilisant le programme commercial d'inversion Res2DInv, avec la norme L1 considérée plus robuste. La zone comprise entre les rives du lac et le bord externe du cratère de divise en trois formations géologiques principales. Les régions de faibles résistivités (< 64 Ω.m) représentent les sédiments de lac. Les zones de resistivités moyennes (entre 128 et 200 Ω.m) sont interprétées comme des brèches liées à l'impact, en dikes, allochtones ou parautochtones. Les régions de hautes résistivités (> 128 Ω.m) représentent les roches métamorphiques sous-jacentes, d'origine volcanique ou sédimentaire. Les profils de résistivités permettent de retrouver la géométrie et l'extension latérale de ces trois types de roches. Une correspondance directe entre la lithologie observée en surface et les structures mises en évidence par les mesures de résistivité électrique dans le sous-sol est observée à Dwamam au Sud-Est du lac. À Dwamam, les sédiments sont environ à 200 m de la rive du lac et s'étendent environ sur 400 m vers les les bords du cratère, à la différence des autres zones où ont pu être cartographiés les sédiments. La topographie du contact sédiment/roche basale présente une direction particulière NE-SO avec un pendage variant entre 16^o au NE et 36^o au SO. Une majorité de fractures ont été remarquées dans le SO, remplies par des clasts et des brèches d'impacts. Les failles sont surtout présentent à l'Ouest du lac. En moyenne elles présentent un pendage variant entre 60^o à l'Est et 80^o à l'Ouest du cratère. Des analyses statistiques ont été effectuées sur les directions et les pendages des failles selon les loi de von Mises et Fisher. Elles démontrent que les failles s'alignent préférentiellement le long de deux directions principales. L'analyse cumulée de la surface de contact sédiment/roche, des failles et de la localisation du champ de dispersion des tektites indique que le bolide d'environ 0,8 à 1 km de diamètre responsable du cratère est arrivé du NE. Les résultats démontrent que les panneaux de résistivité électrique fournissent des informations utiles pour l'étude des cratères d'impact.

Mots-clés: Bosumtwi; Cratère d'impact; Tomographies de résistivité électrique; Inversion

Contents

List of Tables

List of Figures

Acknowledgement

My first and foremost appreciation goes to the Almighty God for His unending mercies and grace towards me throughout the duration of this work. Special thanks to my supervisors: Prof. Piotr Tucholka (Universitè Paris Sud (UPSUD), Orsay, France) and Prof. Sylvester K. Danuor (Kwame Nkrumah University of Science and Technology (KNUST), Kumasi, Ghana) for their excellent support and advice and encouragement throughout the thesis.

I also thank the French Embassy, Ghana and KNUST for sponsoring this split-site/split-cost programme. In particular, I thank Valérie Lesbros of the Embassy for the help she offered in processing my documents and making the trips much easier. I thank Mr. and Mrs. Asare and Dr. and Mrs. Donkor (KNUST) for their moral support, testing of the modified equipment and help with the latex programme. I thank the staff of the Geophysics Section of Département des Science de la Terres, UPSUD and Physics Department, KNUST, many of whom made contributions to the success of this work. I also thank Profs. Annick Suzor-Weiner, Piotr Tucholka, Aboagye Menyeh and Sylvester K. Danuor for the respective roles they played in securing this split-site/split-cost programme.

Without the support of the following people data acquisition would not have been possible: Evans Manu, Thomas Quansah, Reginald Noye, Sedoawu Obed, Worlanyo Ablordepey, Andrew Davidson, David Andorful, Boadi Benjamin, Amonoo Parker, Mohammed Hadi, Ben Kofi, Kwame Agyemang, Seth Mensah and Yaw Amofa. I also thank the Bosumtwi District Assembly, the chiefs and people of the communities around the lake for giving me the permission to work on their land. I appreciate the support and assistance from colleague doctoral students of the geophysics section of Interaction et Dynamique Environnements de Surface (IDES), UPSUD.

Lastly, I greatly thank my wife, children, family members and friends for their encouragement and support.

CHAPTER 1

INTRODUCTION

1.1 The Lake Bosumtwi Impact Crater

The Bosumtwi impact crater (Figure 1.1) is located about 30 km southeast of Kumasi in the Ashanti Region of Ghana. The complex terrestrial impact crater at Lake Bosumtwi in Ghana (06° 30′ N, 01° 25′ W) is the youngest (~1.07 Myr old) and best-preserved of about 95 terrestrial impact structures without modification of the crater morphology (Karp et al., 2002). It has a rim-to-rim diameter of about 10.5 km and is almost completely filled by Lake Bosumtwi which has a diameter of 8.5 km and a maximum depth of 75 m (Scholz et al., 2002). The crater is surrounded by a slight and irregular circular depression, as well as an outer ring of minor topographic height.

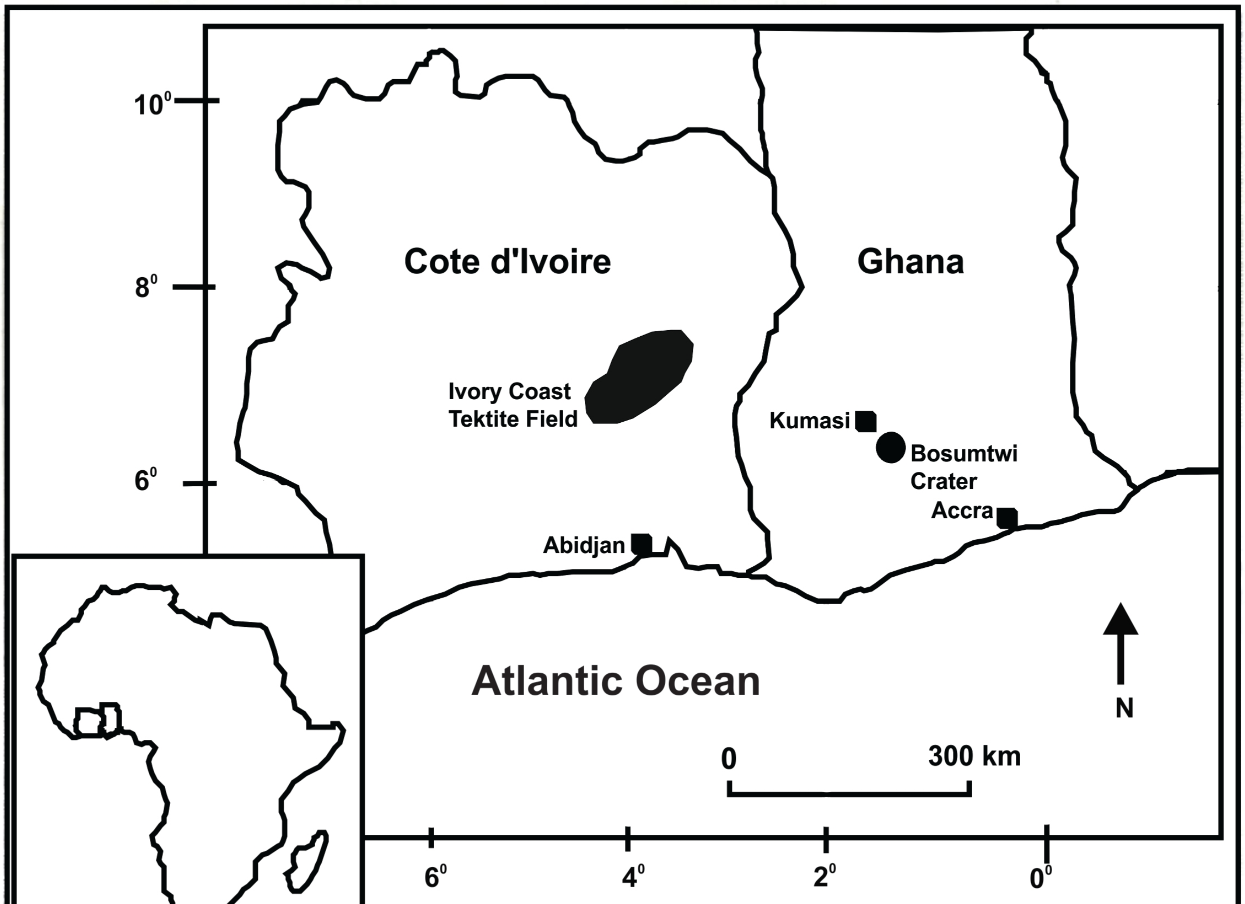

Figure 1.1 – Overview of the Bosumtwi crater location and relation to the Ivory Coast tektite strewn field (Koeberl et al., 1998)

The source of the Lake Bosumtwi crater (Figure 1.2) was a very contentious topic according to Junner (1937) and Jones (1985a) and it was caused partly by the incomplete understanding of impact cratering processes at that time (Bampo, 1963; Smit, 1964). Different hypotheses were advanced to explain the origin of the crater: Fergusson (1902) said that it was not of volcanic origin, Kitson (1916) explained that it was a subsidence feature, Rohleder (1936) preferred an endogenic (explosive) explanation and Maclaren (1931) was the first person to propose that the crater was of impact origin.

The citizens of Abono, a community at the shore of the lake have their own version of the origin of the lake. According to them the lake was discovered by hunter called Akora Bompe in 1640 when he was on a hunting expedition with his dog 'Daakyi' (meaning 'future') on an 'Akwasidae' (meaning 'sacred Sunday') afternoon. On his way home after spending the rest of the afternoon and whole night without a game he saw an antelope and shot it but it run away. He and his dog followed it by tracing the footprints and the blood stains. They later spotted the antelope by a small pond (the lake at that time) and it jumped into the pond upon seeing them. He searched for it and could not locate it and concluded that the antelope belonged to the lake. He called the pond 'Bosom Otwee' (meaning 'god's antelope') because he taught that the lake is a spirit (Danuor, 2004).

Figure 1.2 – Panoramic view of Bosumtwi crater (Koeberl and Reimold, 2005)

The discovery of an extraterrestrial component in impact-derived melt rocks or breccias can be of diagnostic value to provide confirming evidence for an impact origin of a geological structure (Koeberl et al., 1998; 2007a) and the discovery of meteoritic signatures at impact craters is important because, under ideal conditions, it allows constraints to be placed on the types of impactors that form terrestrial impact structures (McDonald et al., 2005). However, a large amount of evidence in support of the meteoritic impact origin of the crater that was first suggested as early as 1931 by Maclaren (1931), has been found (Jones et al., 1981) and its extraterrestrial origin is now generally accepted.

Lithostratigraphic, petrographic and other studies from International Continental Scientific Drilling Program (ICDP) drill core samples from Bosumtwi revealed sequences of impactites below the post-impact crater sediments (Coney et al., 2007a; Deutsch et al., 2007; Ferriére et al., 2007a; Schell et al., 2007) and evidence of shock metamorphism (Deutsch et al., 2007; Morrow, 2007).

Rattray (1923) and Danuor (2004) gave a detail account of the myths, customs and traditions about the lake which was discovered in 1640 by hunter called Akora Bompe.

1.2 Previous Work at the Lake Bosumtwi Impact Crater

Although a lot of work has been done at the Bosumtwi crater area spanning biological, ecotourism and many other areas, this section focuses on the geological, geophysical, the ICDP drilling and numerical modeling of the impact crater .

1.2.1 Geological Studies

Junner (1937), Woodfield (1966), Moon and Mason (1967), Jones et al. (1981) and Reimold et al. (1998) have carried out detailed geological studies around the Bosumtwi crater area. The researchers marked numerous breccia exposures some of which are likely to be a result of lateratization and secondary mass wasting process. Suevites and other rock types were recovered from core samples of seven short holes drilled in 1999 under a shallow drilling program by the University of Vienna with the cooperation of the Geological Survey Department of Ghana (GSD). The findings of the study are described by Boamah (2001); Boamah and Koeberl (2002; 2003). Koeberl et al. (1997b) and Reimold et al. (1997; 1998) reported of structural geological studies along a road cut on the NW–SE portion of the crater rim traverse. The detailed geology of the Bosumtwi crater area is given in chapter three.

1.2.2 Geophysical Studies at Bosumtwi

1.2.2.1 Magnetic Studies

The magnetic field studies by Jones et al. (1981) revealed a central negative anomaly of ~40 nT, and was attributed to a lens of low-density crater-fill breccia below the lake sediments. Koeberl et al. (1997b); Pesonen et al. (1998; 1999; 2003) reported a more detailed information of the subsurface structure below and beyond the lake from a high-resolution aerogeophysical survey data collected in 1997. Their findings include the posibility of a central uplift and delineation of two ring features, with one coinciding with actual crater rim (ca. 11 km diameter), but they could not determined the origin of the outer ring feature (ca. 18 km diameter).

The magnetic model for the Bosumtwi structure produced by Plado et al. (2000) shows a circumferential magnetic halo outside the crater, at a radial distance from the centre of ~6 km and a central negative magnetic anomaly with smaller positive side-anomalies N and S of it situated at the central north part of the lake. The model shows that the magnetic anomaly of the structure is presumably produced by one or several relatively strongly remanently magnetized impact melt rock or melt-rich suevite bodies in the crater. Plado et al. (2000) and Elbra et al. (2007) showed that there is a clear difference between the physical properties of pre-impact target rocks and impactites and that in the suevites, the remanent magnetization is higher than the induced magnetization. Plado et al. (2000) and Elbra et al. (2007) again reported that the normally magnetized remanence component in the suevites was acquired during the Jaramillo (starting at about 1.07 Myr) normal polarity epoch (Channell et al., 2002; Glass et al., 1991). Other researchers like Morris et al. (2007a), Elbra et al. (2007) and Ugalde et al. (2007b) did not find any evidence of the existence of the strongly magnetic impact-melt body underneath the lake sediments as reported by earlier researchers.

1.2.2.2 Gravity Studies

Jones et al. (1981) carried out gravity measurements around the lake and the results reflected only the regional trends. Grieve and Pilkington (1996) reported that there is a general gravity low over the structure caused by the lower-density breccia, as is typical for impact structures. Gravity modelling by Danuor (2004) and Danuor and Menyeh (2006) show that the gravity field of the Bosumtwi area is characterized by a negative Bouguer anomaly with an amplitude of about –18 mgal and a diameter of about 13 km. The results of the 3D gravity model by Ugalde et al. (2007a) agree well with the findings of Danuor (2004) and Karp (2002). The model exhibits lateral density variations across the structure and also shows that intervals comprising polymict lithic impact breccia and suevite, monomict lithic breccia and fractured basement is much smaller than that predicted by numerical modelling.

1.2.2.3 Seismic Studies

A high-resolution seismic survey was conducted in 1999 and 2000 and the data and their interpretations were published by Karp et al. (2002), Scholz et al. (2002), and Danuor (2004). They found that the central uplift structure has a width of 1.8 km and a maximum height of 120 m above the top of the breccia. They reported that fracturing may be responsible for the relatively low velocity of 3.8 kms^{-1} in the crater floor. The post-impact sediments covering the crater structure are 180 – 300 m thick. The apparent crater depth, defined as the difference between the original target surface and the top of the breccia layer, is ~550 m, slightly deeper than several other complex impact structures on Earth of larger diameter (Grieve, 1991). In this aspect, the Bosumtwi impact structure is a small complex crater that deviates slightly from trends predicted from classical scaling laws. Scholz et al. (2007), Schmitt et al. (2007) and Ugalde et al. (2007a), substantiated the findings of Danuor (2004) and Karp (2002) and reported that the central uplift has an overall irregular upper surface with a small graben structure. They also observe a series of normal faults that extend as much as 120 m into the sedimentary section above the central uplift and the decreasing density of fractures and microcracks with depth.

1.2.3 The ICDP Drilling Project

According to Koeberl et al. (2007b) the two main reasons for 2004 ICDP drilling are:

- to fill the data gap in paleoenvironmental record in Africa near the equator for the past one million years, and
- to acquire the catalogue of impactites at the central uplift and in the crater moat to ascertain the findings of earlier reseachers and for comparison with other structures.

For details of the studies the reader is kindly referred to Koeberl et al. (2007b), Karikari et al. (2007), Scholz et al. (2007), Coney et al. (2007a), Morrow (2007), Ferriére et al. (2007a), Deutsch et al. (2007), Petersen et al. (2007), Coney et al. (2007b), Ferriére et al. (2007b), Koeberl et al. (2007a), Goderis et al. (2007), McDonald et al. (2005), Schmitt et al. (2007), Morris et al. (2007b), Hunze and Wonik (2007), Morris et al. (2007a), Kontny et al. (2007), Elbra et al. (2007), Schell et al. (2007), L'Heureux and Milkereit (2007), Ugalde et al. (2007a), and Ugalde et al. (2007b) contained in the special issue of *Meteoritics and Planetary Science 42, Nr 4/5*.

Some of the major findings are:

1. the deep drilling results confirmed the findings of the pre-drilling seismic surveys
2. the impactites exhibit very high porosities (up to 30% vol), which has important implications for mechanical rock stability
3. both petrophysical core analyses and borehole vector magnetic data did not show the presence of the impact melt breccia as expected
4. the sequence of rocks and minerals in the two boreholes (LB – 07A and LB – 08A) are different (Figure 3.2)

It is clear from the findings of the ICDP project that there is the need to review modelling parameters for terrestrial impact craters and to have a second look at existing records of other craters.

1.2.4 Numerical Modelling of the Crater

Artemieva et al. (2004) carried out a numerical modelling of the Bosumtwi impact crater based on the pre-drilling geophysical models of the structure by Karp et al. (2002), Scholz et al. (2002), Danuor and Menyeh (2006) and Plado et al. (2000). They used the 2D SALEB and 3D SOVA numerical hydrocodes for the modelling and reported that in addition to the central uplift and the about 200 m thick coherent melt there is also abundant highly shocked target material within the central part of the crater. They also reported that the distribution of tektites assumes an impact angle of 30^{o} – 45^{o} and an impact direction from the N-NE. They estimated that the fallout ejecta layer inside the crater does not exceed 30 – 40 m.

According to Coney et al. (2007a), Deutsch et al. (2007) and Morrow (2007) there was total absence of a coherent melt sheet and a very low melt or diaplectic glass content in core suevite. Artemieva (2007) explained that the dispersion of impactites due to the vaporization of pore water, which was not included in the original numerical model is the most likely reason for the difference. In their model, they considered two types of targets: a simple granite and a granite basement covered by 40 m thick sand layer but the target rocks at Bosumtwi comprises of metagreywackes and phyllite to slate. This a major anomaly between the modelled results and the reality. These materials behave differently mechanically (Deutsch et al., 2007).

1.3 The Ivory Coast Tektites

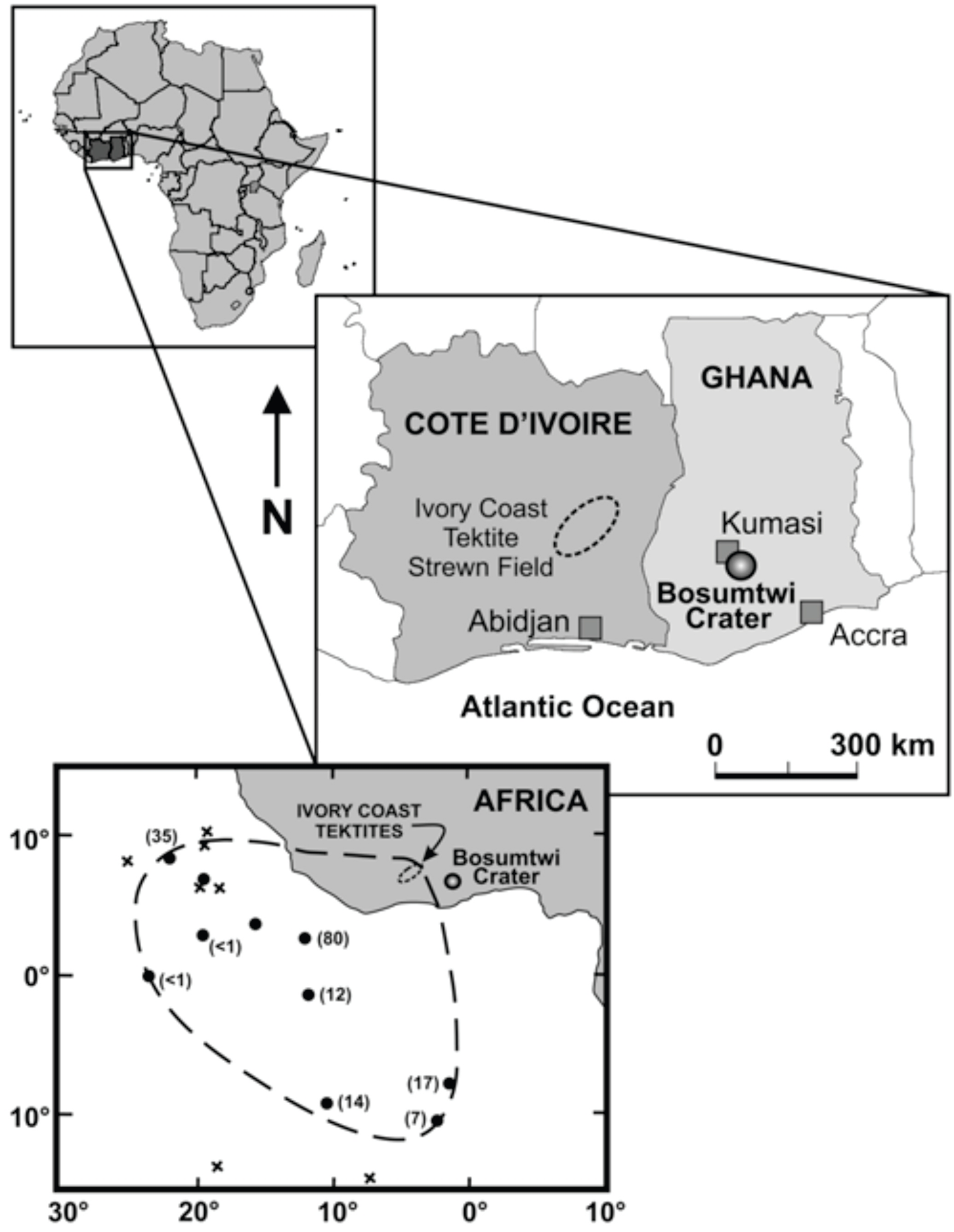

Figure 1.3 – Geographical distribution of microtektites in deep-sea cores in relation to Ivory Coast tektites and Bosumtwi Crater (Glass et al., 1991)

Tektites are distal ejecta produced by hypervelocity impact of meteorites. Tektites are centimeter-sized natural glasses and are found in only four strewn fields in the world (Koeberl et al., 1997a). Table 1.1 shows the four tektite strewn fields and their associated craters and corresponding ages. The Ivory Coast tektite strewn field (Figure 1.3) which is associated with the Bosumtwi impact crater (Koeberl et al., 1997a) was first reported in 1934 by Lacroix (1934), and three and a half decades later, more samples were recovered (Gentner, 1966; Saul, 1969). Microtektites were also found off the coast of West Africa (Glass, 1968; 1969) and are related to the tektites found on land. The geographical distribution of microtektite-bearing deep-sea cores off the coast Western Africa which is between (09° N, and 15° S and 00° and 23° W) has been used to determine the extent of the strewn field (Glass and Zwart, 1979; Glass et al., 1979; 1991), and the microtektite abundance (number cm^{-2}) and size distribution have also been used to accurately predict the size of the source crater located at Lake Bosumtwi (Glass and Pizzuto, 1994; Glass et al., 1991).

Table 1.1 – Strewn fields and their associated craters (Koeberl et al., 1997a)

Tektite Strewnfield	Age of Tektite (Myr)	Impact Crater
North American	35	Chesapeake Bay
Central European (Moldavites)	15	Ries
Ivory Coast	1.1	Bosumtwi
Australasian	0.78	No Crater Identified

There are a lot of evidence in support that the Bosumtwi is the source crater of the Ivory Coast tektite strewn field. These include similar chemical compositions (Schnetzler et al., 1967; Jones, 1985a; Dai et al., 2005; Koeberl et al., 2007a; Coney et al., 2007b), similar isotopic characteristics for the tektites and rocks found at the crater (Schnetzler et al., 1966; Lippolt and Wasserburg, 1966; Shaw and Wasserburg, 1982; Goderis et al., 2007), and similar age for the tektites and the Bosumtwi impact glass (Gentner et al., 1964; 1967; Storzer and Wagner, 1977; Koeberl et al., 1997a). The location of the Ivory Coast Tektites Strewnfield and the microtektites will have some links with the impact direction of the Bosumtwi meteorite.

1.4 Problem Statement

1.4.1 Unresolved Issues

Though extensive work has been done on various scientific aspects of the Bosumtwi impact crater as reported in section 1.2 of this report, no detailed mapping of the inner crater wall which will delineate the sediment/solid rock contact and therefore the exact crater geometry has been done. The geometry of the crater will have some links to the impact direction of the Bosumtwi meteorite which is still not resolved. The distribution of ejecta material, especially the two suevite locations in the NE and SW of the crater and the Ivory Coast tektites and microtektites may have some connection with the impact direction. The Bosumtwi crater drilling results from the two drilled sites (LB – 07A and LB – 08A) did not reveal the very high shock pressures (of about 60 GPa) that are expected from the impact of the Bosumtwi meteorite with diameter between 800 m – 1 km. As a result there is the need to provide additional information and knowledge to enhance numerical modelling of the impact process, the understanding of the high pressure shock waves effects in the target rocks and distribution of ejecta material both inside and outside of the crater.

1.4.2 Purpose of the Research

There is the need to reveal the actual crater geometry, which will provide information for constraints in modelling the impact direction of the meteorite and, therefore, the impact process. This will contribute to a better understanding of the distribution of ejecta materials both inside and outside the crater (e.g. the suevites around the crater and tektites found in Ivory Coast and the deep sea microtektites off the coast of West Africa) and the areas of the deeper crater structure most likely affected by the high pressure shock wave effects.

1.5 Project Objectives

The core objective of this geophysical investigation at the Bosumtwi Impact Crater is to use Electrical Resistivity Tomography (ERT) to map the inner wall of the crater. The specific objectives are:

- to delineate the sediment/solid rock contact of the crater wall
- to reveal the areas of the deeper crater structure most likely affected by the high pressure shock wave effects
- to reveal the actual crater geometry
- to reveal the fracture pattern/orientation in the target rocks
- to provide information for constraints in modelling the impact direction of the meteorite
- to contribute to a better understanding of the distribution of ejecta materials both inside and outside the crater (e.g. the suevites around the crater and tektites found in Ivory Coast and the microtektites off the coast of West Africa)

This research is a collaboration between the Kwame Nkrumah University of Science and Technology (KNUST), Kumasi, Ghana and Universitè Paris Sud, Orsay, France.

1.6 Methodology

Electrical resistivity tomography (ERT) data were acquired along profiles that were laid radially and perpendiculary to the lake shore, and extending through the terraces towards the rim area. The data were topographically corrected and inverted using Res2DInv algorithm proposed by Loke and Barker (1996b). The inferred faults were statistically treated using the von Mises and Fisher distributions.

1.7 Preliminary Studies at the Maar of Beaunit, France

The maar of Beaunit which is a miniature of Lake Bosumtwi was used as a prelude. The Maar of Beaunit is the most northerly volcano of the main “Chaîne des Puys”; its crater contains a strombolian cone, the Puy Gonnard. The crater is 1 km in diameter at its widest point. The maar of Beaunit project provided a crucial knowledge for the fieldwork and subsequent analysis and interpretations of this report. For details of the studies the reader is kindly referred to Chapter 9.

1.8 Outline of Thesis

The location of the Bosumtwi Crater, previous geological, geophysical and other works done at the Bosumtwi Crater area, the problem statement and the project objectives are covered in *Chapter 1*. *Chapter 2* gives an overview of Terrestrial Impact craters. *Chapter 3* is about the geology and structure of the Bosumtwi crater. The DC electrical resistivity technique, the forward modelling and the inversion method are presented in *Chapter 4*. The contruction of a roller, the modification of the ABEM cable and the methodology are discussed in *Chapter 5*. The results and discussions are presented in *Chapters 6 and 7*. *Chapter 8* gives the conclusion and recommendations of the work. *Chapter 9* discusses the preliminary studies that were carried out in Beaunit, France.

CHAPTER 2

IMPACT CRATERS

2.1 Impact Craters

Impact cratering has been recognized as a field of study for only the last few decades. The process itself and its results have, of course, been known far longer. As reported by Melosh (1989), impact cratering is the study of the physics of impact and explosion craters together with the astronomical and geological study of impact craters. Until recently, impacts by extraterrestrial bodies were regarded as an interesting but, perhaps, not an important phenomenon in the spectrum of geological process affecting the Earth. Our concept of the importance of impact processes, however, has been changed radically through planetary exploration, which has shown that virtually all planetary surfaces are cratered from the impact of interplanetary bodies. It is now clear from planetary bodies that have retained portions of their earliest surfaces that impact was a dominant geologic process throughout the early solar system. For example, the oldest lunar surfaces are literally saturated with impact craters, produced by an intense bombardment which lasted from 4.6 to approximately 3.9 billion years ago, at least a 100 times higher than the present impact flux. The Earth, as part of the solar system, experienced the same bombardment as the other planetary bodies (EarthImpactDatabase, 2012).

Craters are the principal physical features on the Moon, Mercury, Mars, and many other solar system bodies. Lunar craters range in size from μm (micrometers) to 2000 km in terms of diameter, while terrestrial impact craters have diameters up to about 200 km or possibly up to 300 km e.g., the Chicxulub crater in Yucatan, Mexico and the Vredefort structure, South Africa (Montanari and Koeberl, 2000; Grieve and Pesonen, 1992).

2.2 Terrestrial Impact Craters

The study of terrestrial impact craters began with the recognition that there are objects in space that occasionally strike the earth at high velocity (Melosh, 1989). Meteorite impacts have also been cited as the causes of extinction of species at various intervals of geologic time. The extinction of large numbers of species was inescapable if mountainlike asteroids or large comets struck the Earth (Erickson, 2003).

Evidence accumulated over the past three decades showed that the Chicxulub impact crater in Yucatan, Mexico which ocurred about 65 Myr ago caused the extinction of the dinosaurs and marked the boundary between the Cretaceous and Tertiary periods (Alvarez et al., 1980; Silver and Schultz, 1982; McLaren and Goodfellow, 1990; Sharpton and Ward, 1990; Ryder et al., 1996; Alvarez, 1997). The giant crater produced by that collision has now been definitely identified, a structure [Chicxulub (Mexico)] at least 180 km across, that is completely buried under the younger sediments of Mexico's Yucatan Peninsula (Hildebrand et al., 1991; Sharpton et al., 1992; Morgan et al., 1997).

Impact craters have not only created geological disturbances, but have produced several geological structures with actual economic value (Grieve and Masaitis, 1994). Some of the economic products of impact structures are local building stone, diamonds, uranium, hydrocarbons (petroleum and gas) (Donofrio, 1997; Johnson and Campbell, 1997), industrial limestone, oil shale, diatomite, gypsum, and lead-zinc ores, nickel and copper sulfide (Guy-Bray, 1972; Pye et al., 1984; Dressler et al., 1994; Lightfoot and Naldrett, 1994).

2.2.1 Formation of Terrestrial Impact Craters

Impact craters are produce when an asteroid, or comet hit the Earth with a cosmic velocity (between 11 and 72 kms^{-1}). The process is very fast and a large amount of kinetic energy is released upon the impact in a very short time (Melosh, 1989; Roddy et al., 1977; Koeberl and Anderson, 1996). Penetration craters or penetration funnels are produced when the speed of the impactor is less than the cosmic velocity. The heat and pressure produced by larger meteorites are substantially high to melt and even vaporize both the impactor and the immediate surrounding terrestrial rock and as a result fragments of the impacting body are not usually found near large impact craters. The crater is produced by intense shock waves that are generated at the point of impact and radiate outward through the target rocks. Peak shock pressures produced at typical cosmic encounter velocities may reach several hundred GPa which are far above the stress levels (about 1 GPa) at which terrestrial rocks undergo normal elastic and plastic deformation, and the shock waves produce unique and permanent deformation effects (known as shock metamorphic effects or shock effects) in the rocks through which they pass (French, 1998).

Shock metamorphism is the series of irreversible changes that occur when rocks are subjected to shock pressures above their Hugoniot elastic limit (HEL), which for most minerals and rocks is of the order of 5 to 10 GPa (Sharpton and Grieve, 1990; Koeberl and Anderson, 1996). In particular, an impact leads to the instantaneous generation of shock waves that penetrate the target area and attenuate in its environs (Melosh, 1989; Roddy et al., 1977; Koeberl and Anderson, 1996).

The formation of an impact crater by hypervelocity impact is divided into three stages with transitions from one stage to the other: contact and compression (or penetration) stage, excavation stage, and post-impact crater modification stage (Melosh, 1989; Gault et al., 1968; Roddy et al., 1977; Koeberl and Anderson, 1996).

2.2.1.1 Contact/Compression Stage

The impact cratering process starts when the projectile hits the target surface. The fleetly moving projectile then thrusts target material out of its path, compressing it and accelerating it to a large percentage of the impact velocity. The target's resistance to penetration lowers down, at the same time, as the projectile velocity (Melosh, 1989). High temperatures and pressures are generated as a result of the transfer of the huge kinetic energy of the projectile to the target rock (Kieffer and Simonds, 1980; O'Keefe and Ahrens, 1982; 1993; Ahrens and O'Keefe, 1977; Melosh, 1989).

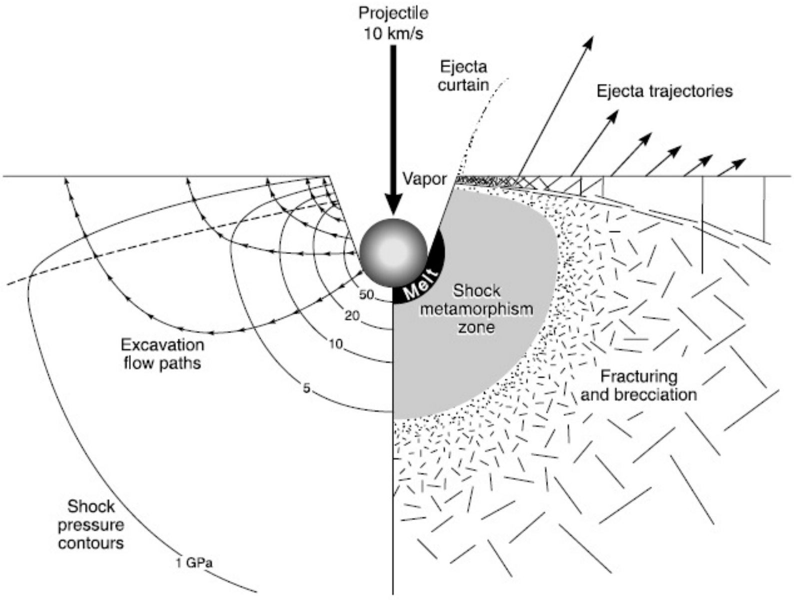

(a) Vertical impact

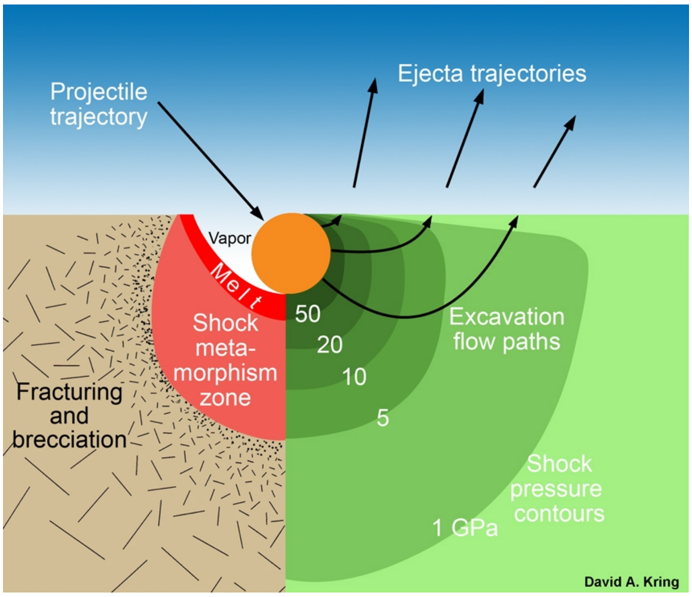

(b) Oblique impact (Kring, 2006)

Figure 2.1 – Contact and compression stage: initial shock wave pressures and excavation flow lines around impact point (French, 1998) modified from (Melosh, 1989)

From theoretical models and geological studies of shock-metamorphosed rocks in individual structures, the impact point can be regarded as being surrounded by a series of concentric and roughly hemispherical shock zones each with a range of peak shock pressure and temperature, and characterized by a unique suite of shock-metamorphic effects as shown in Figure 2.1a for a vertical impact and Figure 2.1b for an oblique impact (Melosh, 1989; Dence, 1968; Dence et al., 1977; Robertson and Grieve, 1977; Dressler et al., 1998; Kring, 2006) . The peak shock-wave pressures decreases from over 100 GPa at the impact point to elastic waves or seismic waves (1 – 2 GPa) near the crater rim (Kieffer and Simonds, 1980).

The duration of the contact and compression stage is determined by the behaviour of the shock wave that was reflected (release wave) back into the projectile from the projectile/target interface (Melosh, 1989). The point at which the release wave reaches the front of the projectile and begins to enter the adjacent compressed target, is taken as the end of the complete contact and compression stage (French, 1998).

No meteorite strikes a planetary surface exactly vertically. Even though some are so close to vertical that the deviation is negligible, the most probable angle of impact for a random incident projectile is 45°. Despite the fact that all but the most oblique (impact <10°) produce circular craters, their ejecta blankets have a bilaterally symmetric 'butterfly wing' pattern that becomes progressively more marked as the obliquity increases. The period of contact and compression for oblique impacts is longer than for vertical impact (Melosh, 1989).

2.2.1.2 Excavation Stage

The crater is opened up during the excavation stage by the complex interactions among the expanding shock waves and the original ground surface. The shock waves that travel upward are reflected downward as rarefactions (release waves) when they intersect the original ground surface. Part of the initial shock-wave energy is converted into kinetic energy and the rocks involved are accelerated outward, much of it as individual fragments travelling at high velocities. The actual flow directions (Figure 2.2) differ with locations within the target rocks.

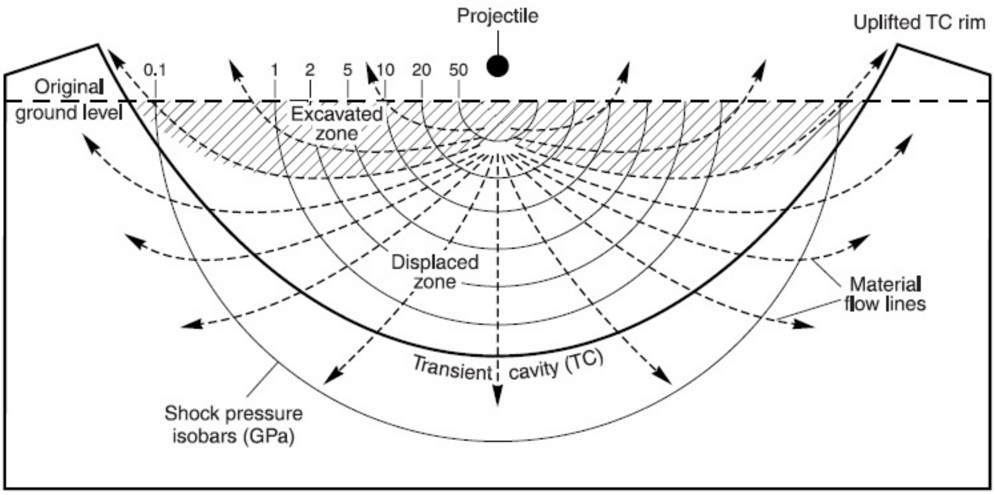

Figure 2.2 – Formation of transient crater in excavation stage (French, 1998) modified from (Grieve, 1987)

The transient crater is divided into approximately equal upper and lower zones (Figures 2.2 and 2.3). The materials in the upper zones mostly moves upward and outward whereas those in the lower zones is displaced downward and outward to form the zone of *parautochthonous* (in-situ) rocks below the floor of the final transient crater. Within the upper excavation zone (or ejection zone), velocities imparted to the target rocks may be as high as several kilometers per second, high enough to excavate the fragmented material and to eject it beyond the rim of the crater (Grieve et al., 1977; Dence et al., 1977; Kieffer and Simonds, 1980; Melosh, 1989). Some of the ejecta could be *suevites*, which are melt-bearing polymict (many components) impact breccias (impact-derived rocks) and *tektites*, which are centimetre-sized natural glasses produced by hypervelocity impact of meteorites and are ejected much earlier than the suevites, probably during the transient crater formation. The excavation stage ends when the shock and release waves can no longer excavate or displace target rock. The size of the final crater is many times larger (typically 20 – 30 times) than that of the projectile itself.

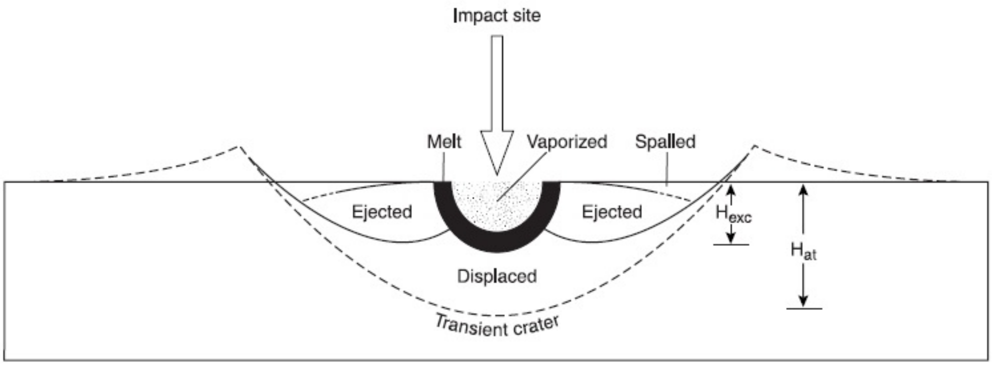

Figure 2.3 – Location of shocked metamorphosed materials in a transient crater (Melosh, 1989)

.

2.2.1.3 Modification Stage

The modification of the transient crater depends on its size, the structure and properties of the target rock. The modification stage begins when the transient crater has grown to its maximum size and the crater is immediately modified by gravity and rock mechanical processes. The transient crater is very unstable and its walls collapse inwards to form a pool on the floor of the final bowl-shaped depression for small craters and slump terraces on the walls and central peaks in larger craters. The modification stage has no clearly marked end, and the modification processes of uplift and collapse merge gradually into the normal processes of geological mass movement, isostatic uplift, erosion, and sedimentation (Melosh, 1989; French, 1998).

2.2.2 Crater Morphology

Morphology is one of the criteria for the recognition and confirmation of impact structures. The others are geophysical characteristics or anomalies, evidence for shock metamorphism and presence or traces of the meteorite (Pilkington and Grieve, 1992; Grieve and Pilkington, 1996; Koeberl and Anderson, 1996). Impact craters have two basic morphological forms: simple or complex (Melosh, 1989; Grieve and Pilkington, 1996). The circular, shallow, and rootless nature of impact craters distinguished them from volcanic craters. All impact craters have an outer rim and some crater infill e.g., brecciated and/or fractured rocks, impact melt rocks. The central structural uplift in complex craters consists of a central peak or of one or more peak ring(s), and exposes rocks that are uplifted from considerable depth. The central structural uplift usually contains severely shocked material and is often more resistant to erosion than the rest of the crater. In old eroded structures the central uplift may be the only remnant of the crater that can be identified (Grieve and Pesonen, 1992; Koeberl and Anderson, 1996; Melosh, 1989).

2.2.2.1 Simple Craters

Simple craters are bowl-shaped depressions and have diameter of less than about 2 km in sedimentary environment and about 4 km in massive crystalline rocks (these values apply only to Earth). The simple craters are filled, to perhaps half its original depth, by a mixture of fallback ejecta and debris slumped in from the walls and rim. Figure 2.4 shows the progressive development of a small, bowl-shaped simple impact crater in a horizontally layered target (French, 1998).

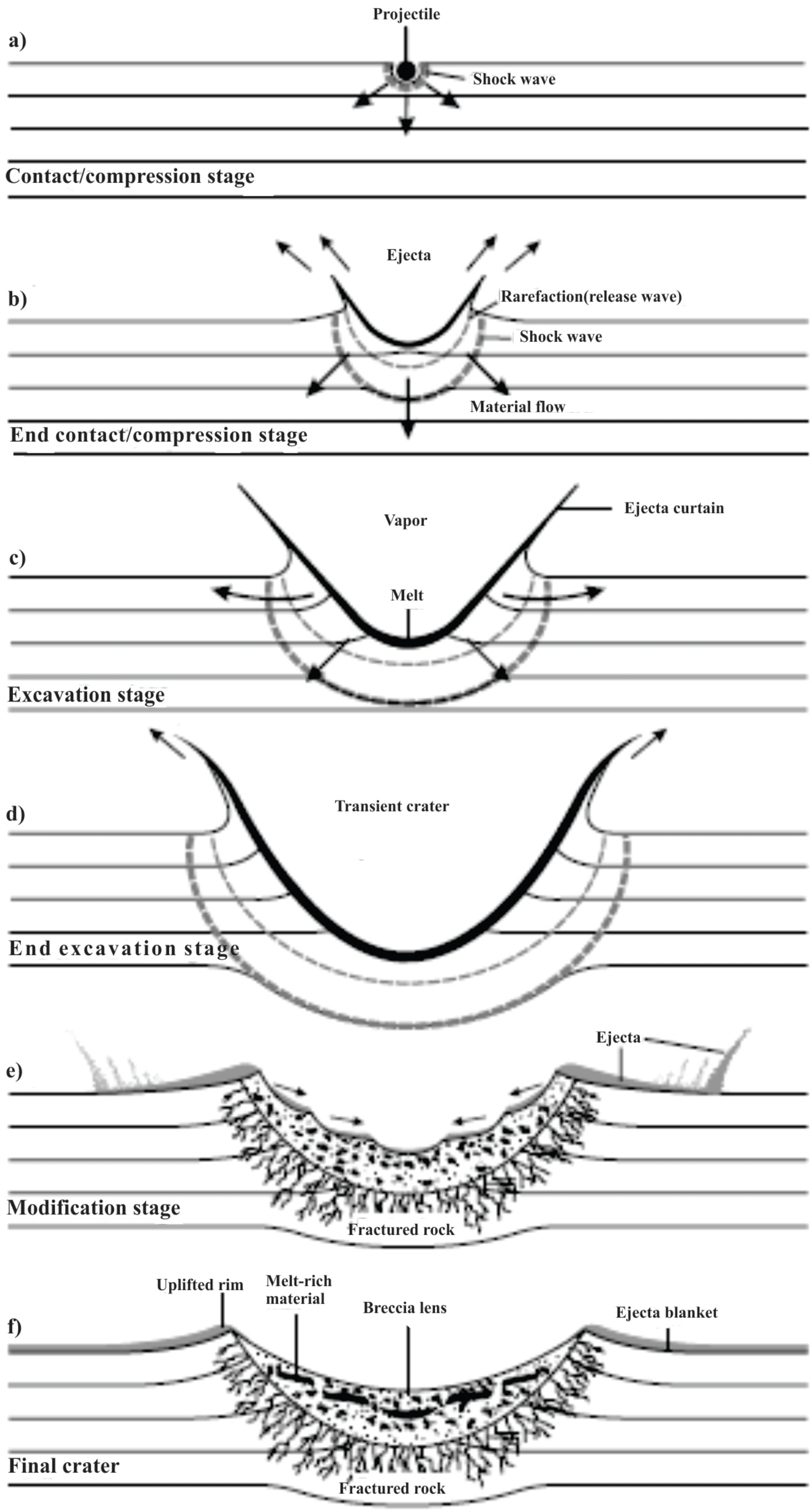

Figure 2.4 – Development of a simple impact structure (French, 1998)

2.2.2.2 Complex Craters

Complex craters are those with wall terraces, central peaks, and flat floors. The central peaks are composed of rocks that originated below the crater floor and that were uplifted a distance equal to about 8% of the crater's final diameter and the diameter of the central peak is about 22% of the crater's rim-to-rim diameter (Melosh, 1989). Structural changes occur in larger impact craters due to the complex interactions between shock-wave effects, gravity, and the strength and structure of the target rocks. These result in the formation of central peak, a generally flat floor and major peripheral collapse around the rim (Dence, 1968; Grieve et al., 1977; 1981; Grieve, 1991; Milton et al., 1972; 1996a;b; Grieve and Pilkington, 1996). Figure 2.5 shows the progressive development of a complex crater in a horizontally layered target (French, 1998).

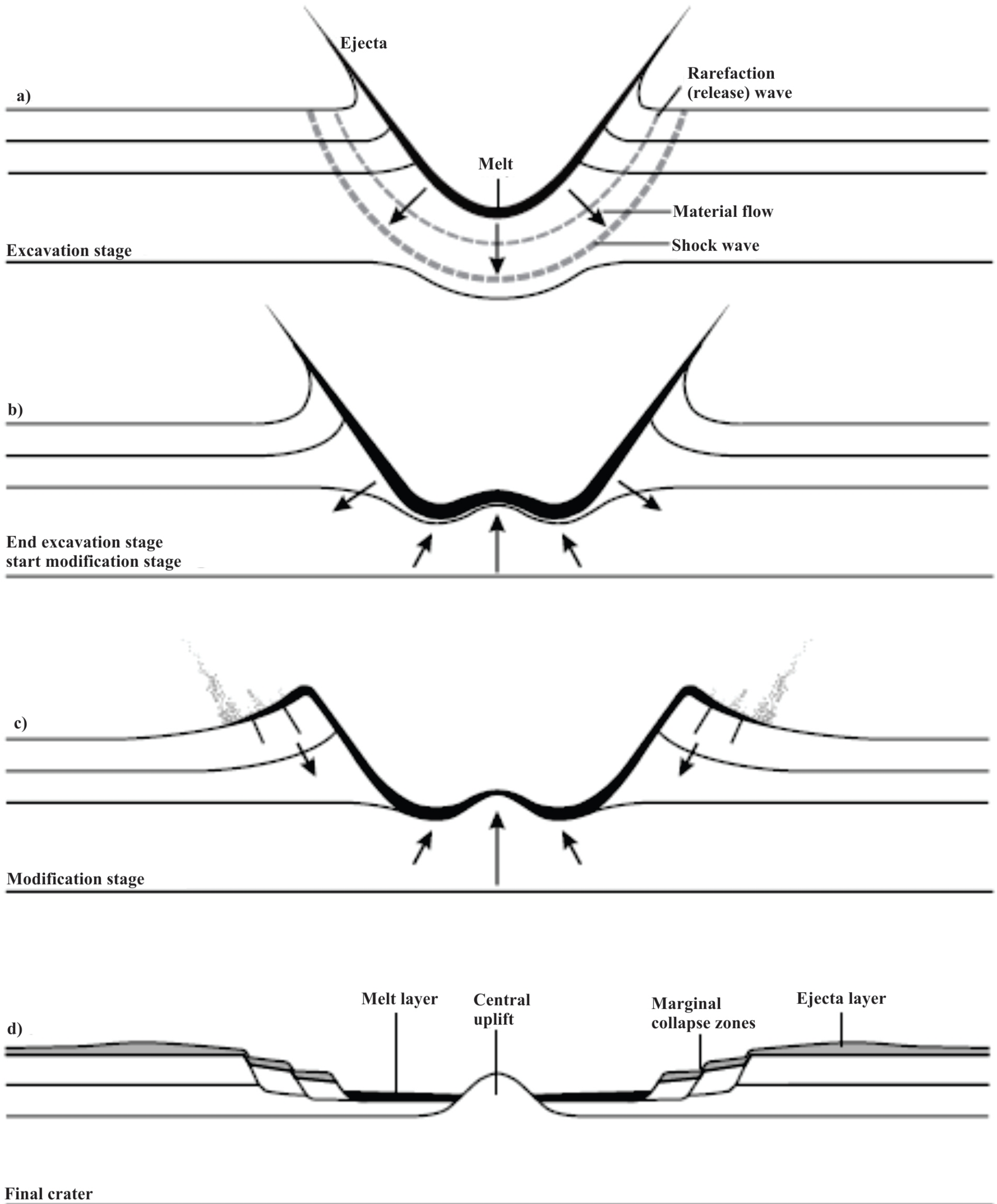

Figure 2.5 – Development of a complex impact structure (French, 1998)

The modification of complex craters are characterized by outward, inward, and upward movements of large volumes of the subcrater rocks. There is still uncertainty despite the lot of evidence that central uplifts are formed in large impact structures (Dence, 1968; Grieve et al., 1981; Melosh, 1989; Horz et al., 1991; Spudis, 1993). The surrounding annular depression is partially filled by *allochthonous* target material, either in the form of polymict breccia or impact melt rocks. According to Grieve and Pesonen (1992), complex craters are deeper in crystalline (stronger) targets than in sedimentary (weaker) targets due to the differences in the intrinsic strength of the target rock. This effect of material strength is reflected in the final morphology of complex craters. The single central peak is gradually replaced by a more complex series of concentric rings and basins as the crater size increases. Three types of complex impact structures can be indexed: central peak structures (diameter = 4 - 22 km), central-peak-basin structures (diameter = 22 - 30 km), and peak ring basin structures (diameter = 30 - 60 km) (Grieve et al., 1981; Melosh, 1989; Spudis, 1993; French, 1998).

2.2.3 Distribution of Terrestrial Impact Craters

There are 182 confirmed impact structures known on Earth presently (EarthImpactDatabase, 2012). The spatial distribution of these known craters (Figure 2.6 and Table 2.1) are not random. The known craters are concentrated in North America, Australia, Europe and Russia than in Africa and South America because there have been active programmes to search for and study impact craters in these regions and these areas also have low levels of erosion to obliterate the structures (Grieve and Pesonen, 1992; Koeberl and Anderson, 1996; Koeberl, 1994).

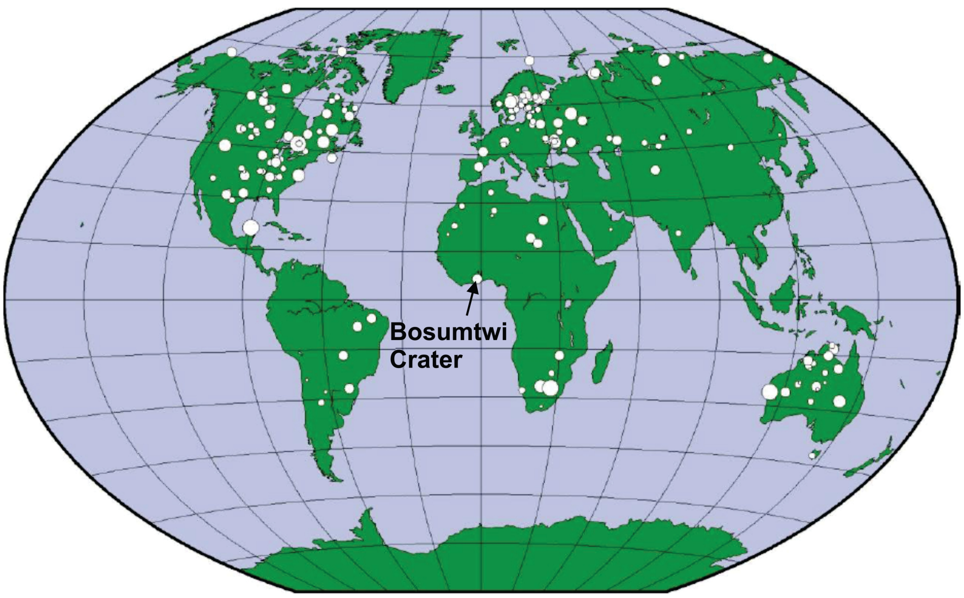

Figure 2.6 – World Distribution of Terrestrial Impact Craters identified as of 1992 ,modified from (Pohl, 2001)

Table 2.1 – Distribution of craters (EarthImpactDatabase, 2012)

Continent	Number of Impact Crater
Africa	19
Asia and Russia	30
Australia	27
Europe	38
North America	59
South America	9

CHAPTER 3

GEOLOGY AND STRUCTURE OF THE BOSUMTWI CRATER

3.1 Geology of the Crater Area

3.1.1 General

The Bosumtwi crater (Figure 3.1) was dug out in lower greenschist-facies supracrustal rocks of the 2.1 – 2.2 Gyr old Birimian Supergroup; comprising mainly metasediments and metavolcanics (Wright et al., 1985; Leube et al., 1990; Davis et al., 1994; Hirdes et al., 1996; Oberthür et al., 1998; Watkins et al., 1993; Koeberl and Reimold, 2005; Karikari et al., 2007; Coney et al., 2007a). Birimian target rocks are made up of mica schists and banded schists with both micaceous and quartz-feldspathic bands, phyllite, metagreywacke, quartzite and sandstone, shale and slate, as well as meta-tuffs. Birimian meta-volcanic rocks (altered basic intrusives intercalated with some metasediments) occur in the southeastern sector of the Bosumtwi area. Graywackes predominate the surface exposures and are the most important clast type in many suevite samples. Brecciated greywacke and phyllite dominate the geology immediately around the crater and locally intruded by small dikes and pods of granitic intrusive (Junner, 1937; Moon and Mason, 1967; Reimold et al., 1998; Koeberl and Reimold, 2005). Carbonate (calcite) which was previously unknown was identified in high abundance in the analysis of drill cores and their origin is pre–impact (Coney et al., 2007a; Deutsch et al., 2007; Ferriére et al., 2007b).

Other than the Obuom Range to the southeast of the crater, the topography of the Lake Bosumtwi drainage basin follows the Pleistocene relief produced by the impact structure. Lake morphometry is that of a simple bowl-shaped depression, which developed from the accumulation of post-impact lacustrine and alluvial sediments. The well-defined crater was initially characterized as a caldera (Smit, 1964) and has an average rim elevation of ~250 to ~300 m above the lake surface which is about 80–100 m below the terrain outside of the rim (Koeberl and Reimold, 2005). Except for the terrain of the Obuom mountain range, and locations along some stream channels in the environs of the crater, exposure is generally very poor.

Recent rock formations include the lake beds and the products of weathering (laterites, soil) which can have thicknesses up to 10 m. Although no impact melt rock has been found around the crater (Jones et al., 1981; Reimold et al., 1998), numerous breccia and suevite exposures have been mapped (Koeberl and Reimold, 2005). Recent drilling into the crater floor (Figure 3.2) revealed that shales did indeed represent a major component of the target geology.

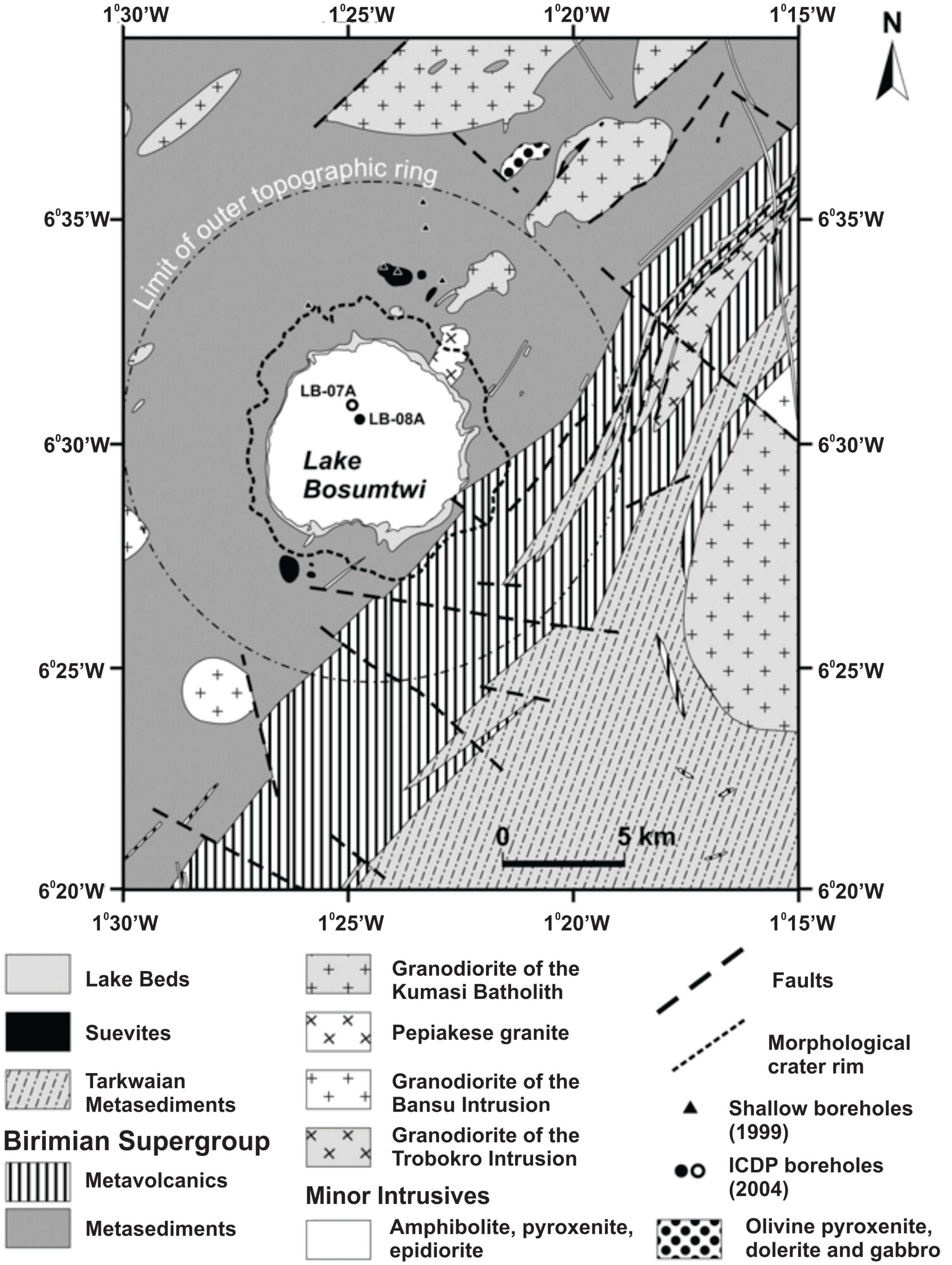

Figure 3.1 – Geological map of the Bosumtwi impact crater area (Koeberl and Reimold, 2005).

3.1.2 Intrusive Bodies

A variety of granitoid intrusions (biotite or amphibole granites) is also present in the Bosumtwi region (Junner, 1937; Woodfield, 1966; Moon and Mason, 1967; Jones, 1985a; Koeberl and Reimold, 2005). Granite intrusions, probably connected with the Kumasi batholith, outcrop around the north, northeast, east, and west sides of the lake, (e.g., the Pepiakese granite on the northeast side of the lake (Jones, 1985b; Koeberl and Reimold, 2005). Biotite and hornblende granodiorites (Bansu and Trobokro intrusions) (Koeberl and Reimold, 2005) outcrop to the south and west of the lake. Moon and Mason (1967) refer to the Bansu intrusion as a coarse, foliated biotite adamellite and finergrained, leucocratic microcline granite and the Trobokro intrusion as biotite granodiorite. Numerous narrow dikes of biotite granitoid occur at many basement exposures in the crater rim (Reimold et al., 1998). The overall granite component in the vicinity of the crater, and by implication to the target composition, was estimated at less than 2% (Reimold et al., 1998).

3.1.3 The Impact Breccia

Koeberl and Reimold (2005) grouped the breccia at Bosumtwi into three types based on their composition and texture: autochthonous (brecciated monomict), allochthonous (polymict lithic breccia) and the suevites which occur only in the north and south of the crater. Stöffler and Grieve (1994) defined suevite as polymict impact breccia including cogenetic impact melt particles which are in a glassy or crystallized state, included in a clastic matrix containing lithic and mineral clasts in various stages of shock metamorphism. Junner (1937) alluded that the Bosumtwi suevites found at the north and southwest (Figure 3.1) were volcanic tuff and agglomerates. The suevite contains target rock fragments (e.g., metagraywacke, phyllite, shale, granite) in all stages of shock metamorphism, including vitreous and devitrified impact glasses. The suevites at Bosumtwi are located in an area (about 1.5 km^2) outside the rim of the crater in the north, about 2.5 km from the lakeshore (in the area between 01° 23.5′ – 01° 24.5′ W and 06° 33.5′ – 06° 34.2′ N). They occur as large blocks up to several meters wide and as patchy massive deposits more or less and covered by thick vegetation. Shallow drill cores into suevites occurrences (Boamah and Koeberl, 2002; 2003; 2006) were obtained to the north of the crater rim.

Meta-graywacke/phyllite rocks and granite from dikes seem to be important contributors to the compositions of the suevite and the road cut samples (fragmentary matrix), with a minor contribution of Pepiakese granite. The thickness of the fallout suevites outside the northern rim of the Bosumtwi crater is 15 m, and this facies occupies an area of about 1.5 km^2 (Boamah and Koeberl, 2002; 2003). The present distribution of the suevite is likely a result of differential erosion and does not reflect the initial distribution.

Melt proportions are higher outside the crater rim, and this implies that much of the most heavily shocked material has been ejected from the crater. The relative amount of shocked and melted material in suevites from the central uplift is lower than in suevite from outside the northern crater rim (Coney et al., 2007a; Ferriére et al., 2007a). The lithostratigraphies (Figure 3.2) for the two boreholes LB – 07A and LB – 08A are substantially different, very little monomict impact breccia has been found in LB – 08A (~ 1 m) (Ferriére et al., 2007a) whereas nearly 55 m of monomict breccia have been noted in LB – 07A. The total thickness of the melt-bearing suevites of the uppermost part of LB – 08A (<10 m) is substantially different from LB – 07A (nearly 50 m). Notwithstanding these differences, similar petrographic observations have been made for both cores (Ferriére et al., 2006a;b). Most of the suevites in LB – 07A are derived from <35 GPa shock zone compared with the order of >45 GPa for LB – 08A (Coney et al., 2007a; Ferriére et al., 2007a).

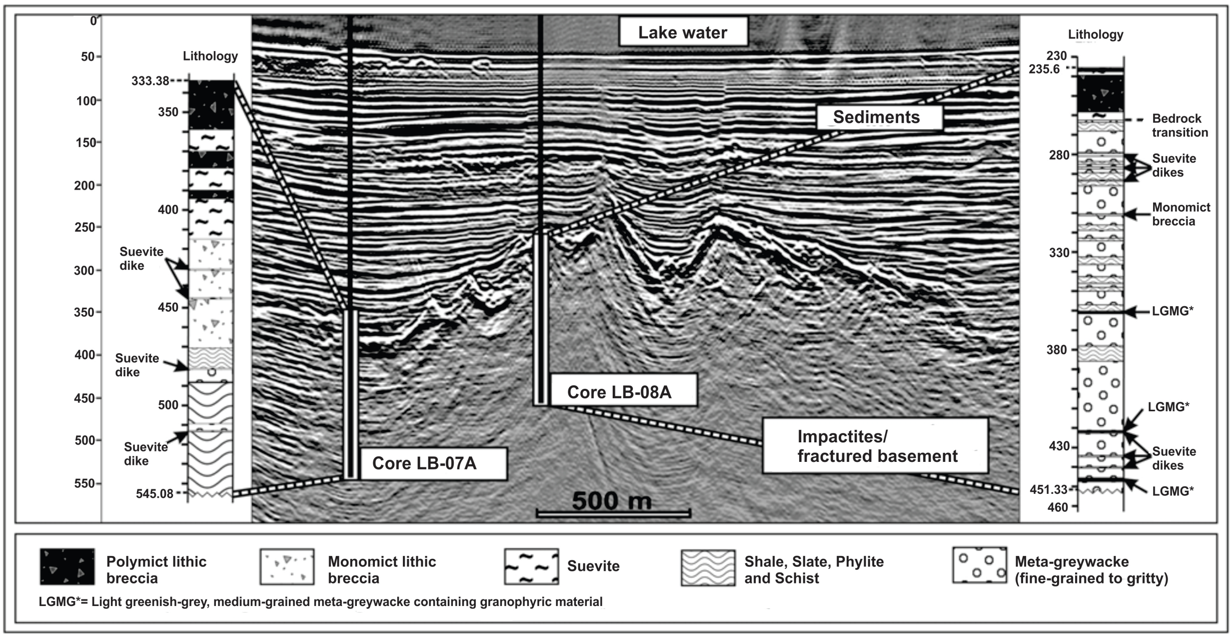

Figure 3.2 – Lithologies of the two hard-rock drill cores superimposed on the seismic profile, showing the clear connection between the two data sets and giving a summary of the lithological observations (Koeberl et al., 2007b).

3.2 Morphology and Structure of the Crater

Geophysical, drill core and remote sensing studies show that the Bosumtwi crater is a complex impact structure (Figure 3.3). The 10.5 km complex impact crater has a central uplift and is almost filled by the 8.5 km Lake Bosumtwi which has a maximum depth of 75 m (Plado et al., 2000; Karp et al., 2002; Scholz et al., 2002; Wagner et al., 2002; Pesonen et al., 2003; Koeberl et al., 2005; Milkereit et al., 2006). Lake morphometry is that of a simple bowl-shaped depression, which developed from the accumulation of post-impact lacustrine and alluvial sediments. The crater has an average rim elevation of ~250 to ~300 m above the lake surface which is about 80–100 m below the terrain outside of the rim. The crater has an apparent depth of about 550 m (Koeberl and Reimold, 2005; Karp et al., 2002; Scholz et al., 2002; 2007). Figure 3.4 shows the digital elevation data of the Bosumtwi crater and the about 18 – 20 km diameter outer ridge, which can be traced from the Obuom Range south of the lake. The outer ridge has a mean elevation of < 30 m and the elevation of the target surface is about 150 m. The thickness of the allochthonous breccia is about 600 m in the central part (Karp et al., 2002; Scholz et al., 2007).

The central uplift has a width of 1.9 km in NW – SE direction and a maximim height of 130 m above the crater moat and it sorrounded by about 300 m thick post impact lacustrine sediments. The faulted central uplift has an irregular upper surface with a small graben structure that is 15 m deep and the faults extend about 120 m into the sediments. The uplift is located away from the centre by (~1 km) to the north geometric centre of the crater (Karp et al., 2002; Scholz et al., 2007).

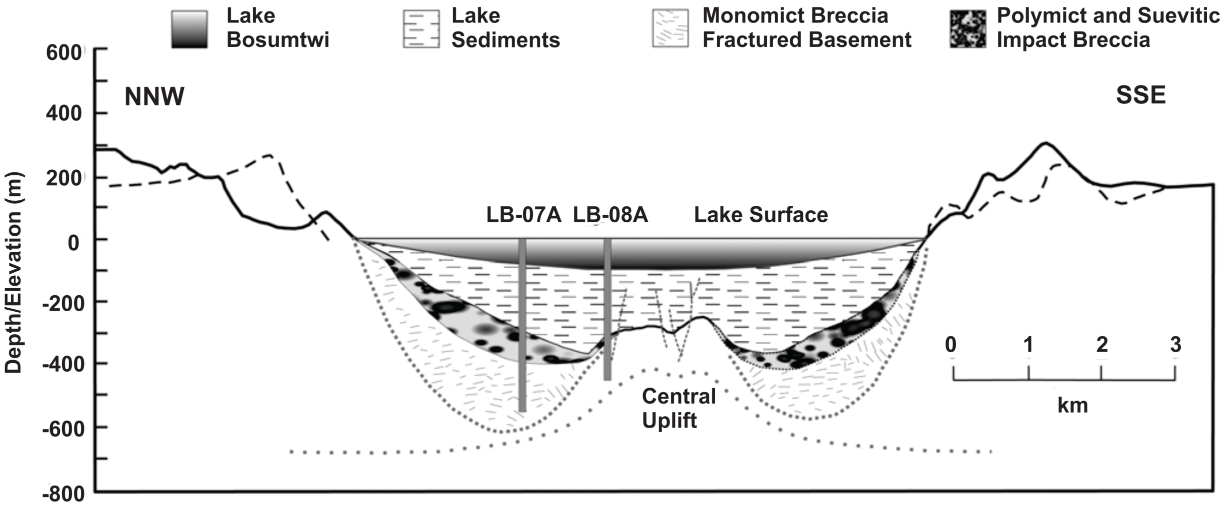

Figure 3.3 – An interpreted cross section of the Bosumtwi crater, based on the first results from the ICDP drilling project. The dashed line underneath the monomict breccia/fractured bedrock marks the zone in which a change to unfractured bedrock is expected. The dotted line indicates the approximate amount of central uplift underneath the structure (Koeberl et al., 2007b).

The Bosumtwi crater has a complex rim shape with steep inner and outer slopes (Figures 3.4 and 3.5a). The western side of the crater has steeper slopes than the other parts and there is a gentler talus slope around the lake with more talus on the western side. Reimold et al. (1998) carried out structural analysis of the rim and found that most of the clasts are strongly weathered and have variable shapes ranging from angular to well rounded (Figure 3.5). They observed that brittle deformation is widespread and quartz veins occur along many fractures and metagraywackes and metasandstones are the dominant lithologies. The faults and beds found outside the crater rim were thrusting outward and dipping inwardly at 40° – 45° and 20° respectively and 45° – 50° and 15° respectively for the faults and beds found inside the crater rim. Hunze and Wonik (2007) observed from televiewer images that that fractures dip at angles between 50° and 70° and the two main dip directions are southeast and southwest with most of the fractures open. They indicated that the main stress direction was north-south.

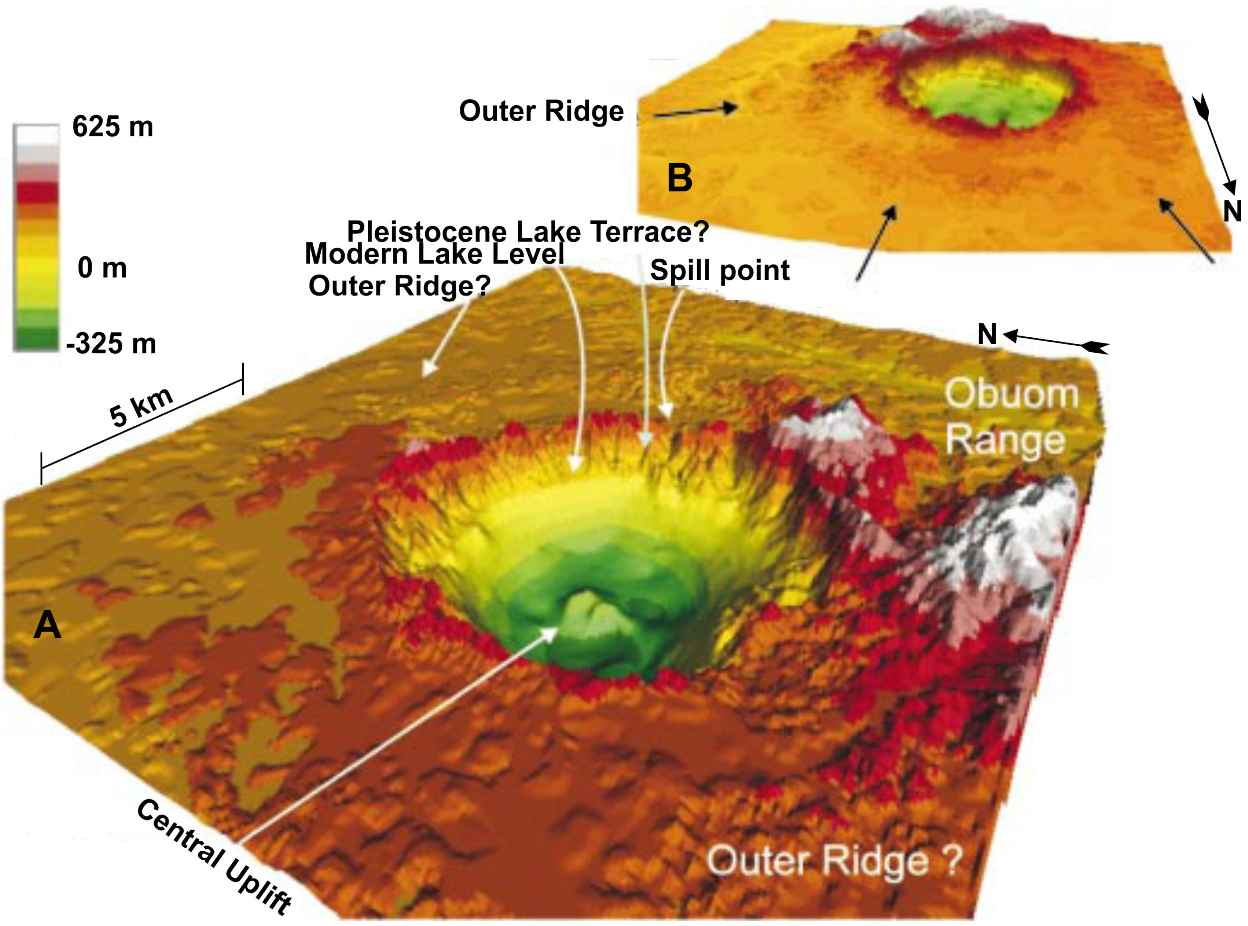

Figure 3.4 – Digital elevation model of Bosumtwi Impact Crater **(A)** at low sun angle, showing the central uplift, spill point, modern lake level and Pleistocene lake terrace and **(B)** at high illumination angle, highlighting outer ridge (Scholz et al., 2002)

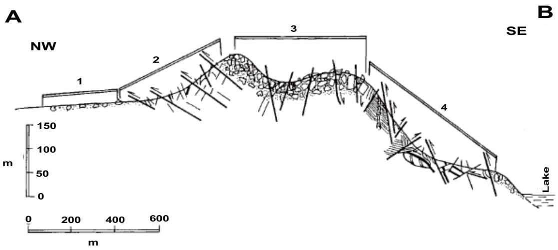

(a) Zonation of the topography of NW part towards the lake

(b) Rim section zone 2; thrust plane dipping inward (to left) and cutting Birimian metagraywacke

(c) Zone 2; isoclinal folding in stratified Birimian metasedimentary rocks

(d) Zone 3, near highest point of rim; lithic impact breccia composed of centimeter to decimeter-sized clasts

(e) Zone 3; megabreccia with meter-sized blocks of Birimian metasedimentary rocks and (lightest-colored) 2 Ga granitoids; width of field of view = 10 m

Figure 3.5 – Zonation of the topography of NW part towards the lake and the geologic features associated with each zone (Reimold et al., 1998)

CHAPTER 4

ELECTRICAL RESISTIVITY

4.1 Introduction

Electrical surveying is an area of geophysical prospecting where there are many methods. The methods may be based on naturally or artificially generated currents which is introduced into the ground. The electrical methods use either direct currents (DC) or low frequency alternating currents (AC) to investigate the subsurface electrical properties. The electrical resistivity methods include:

- Self potential (SP) method measures naturally occurring electrical potentials which are usually caused by charge separation in clay or other minerals, due to presence of semi-permeable interface impeding the diffusion of ions through the pore space of rocks, or by natural flow of a conducting fluid through the rocks,
- Induced potential (IP) method uses electrodes with time-varying currents and voltages to map the variation of electrical permittivity (dielectric constant) in the Earth at low frequencies
- In electrical resistivity surveying, electrical signal is injected into the ground and the resulting potential (how the earth responds to the signal) is measured.

The electrical resistivity method has many applications including:

- Hydrogeology and groundwater: Searching for aquifers. Mapping sea water intrusion. Acid mine investigations
- Mineral exploration: Exploring for minerals, sand and gravel
- Landslides: Mapping of potential landslides.
- Civil engineering: Geotechnical and site investigations. Mapping of faults, groundwater table, sediments/bedrock contact.
- Environmental investigations: Investigating acquifer pollution. Mapping of contamination plumes.
- Permafrost: Mapping of thickness of permafrost
- Others: Monitoring dams. Cavity detection in archaeology. Impact cratering. Stratigraphic correlation in oil fields

4.2 Resistivity of Earth Materials

The subsurface resistivity is dependent on various geological parameters such as the mineral and fluid content, porosity, permeability, temperature, particle size, tortuosity and degree of water saturation in the rock. Geological processes such as weathering, fracturing, columnar jointing, shearing, dissolution and hydrothermal alteration usually increase porosity and fluid permeability and significantly lower the resistivity. Precipitation of calcium carbonates or silica reduces porosity and hence increases resistivity.

Resistivity is one of the most variable of physical properties ranging between $1.6x10^{-8}$ Ωm for native silver to about 10^{16} Ωm for pure sulphur. Figure 4.1 shows the resistivities of some rocks, soils and minerals. The resistivity variation is not only from formation to formation but also within formations. There is no general correlation of the lithology with resistivity but some type of classification is possible between groups of rocks/material that do not overlap.

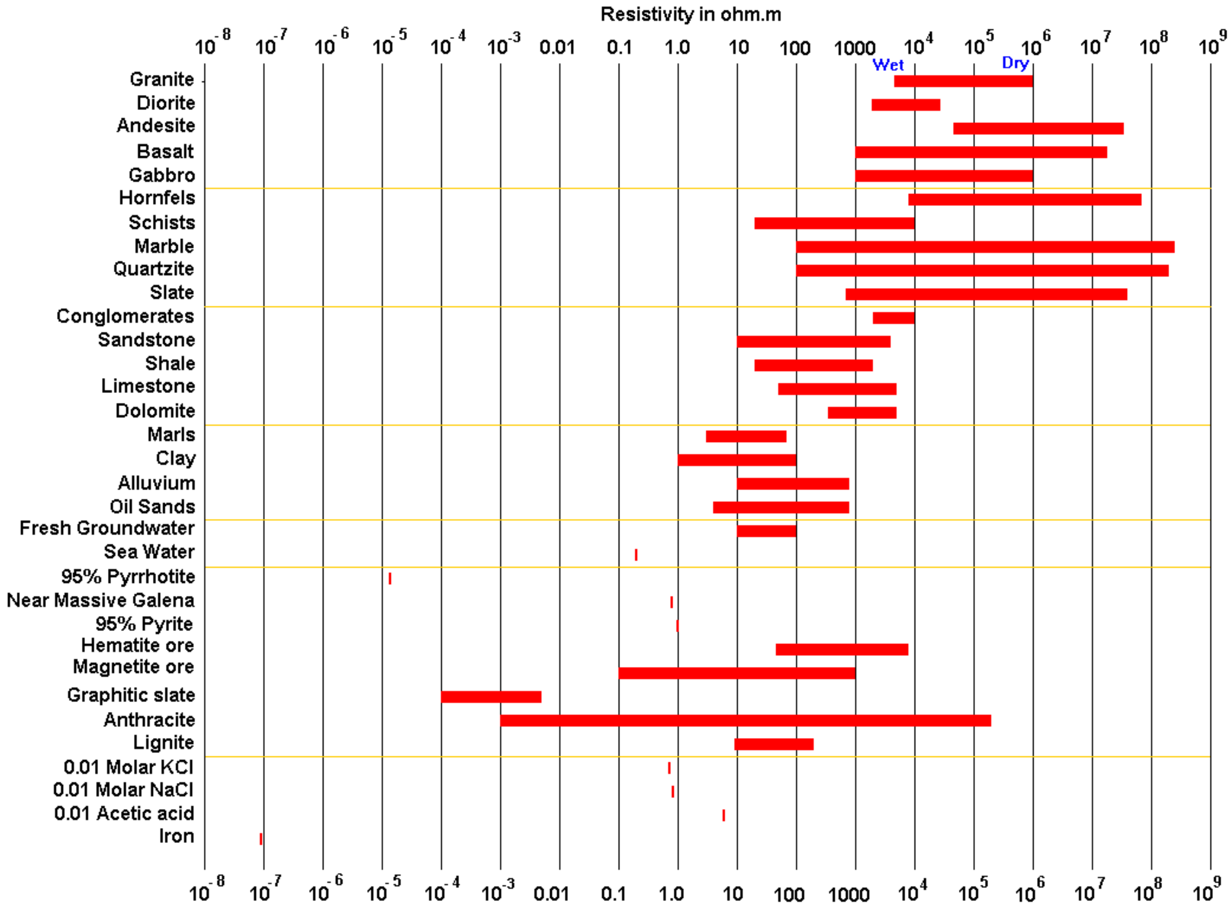

Figure 4.1 – Resistivity of rocks, soils and minerals (Loke, 2011)

Electric current flows through rocks and minerals in three ways: electronic (ohmic), electrolytic and dielectric conduction. Electronic conduction is the process by which metals, for example, allow electrons to move rapidly, so carrying the charge. Electrolytic conduction occurs by the relatively slow movement of ions within an electrolyte and depends upon the type of ion, ionic concentration and mobility, etc. Dielectric conduction takes place in poor conductors or insulators with very few free carriers. Atomic electrons will be displaced with respect to nuclei separation of positive and negative charges (Reynolds, 1997). Sedimentary rocks tend to be the most conductive of the rock types due to their high fluid content and igneous rocks have the highest resistivities and metamorphic rocks have intermediate but overlapping resistivities. The resistivity of igneous and metamorphic rocks depends on the rate of fracturing and whether these fractures are filled with electrolytes, mainly water. The resistivity of ore bodies depends on whether they are massive or disseminated. Electrical current is carried through a rock mainly by the passage of ions in pore waters that is by electrolytic rather than ohmic processes.

The resistivity of the rock according to Archie (1942) relates to the resistivity of the water filling the pores and the volume of the pores by the equation:

$$\rho = a\rho_w \phi^{-m} S^{-n} \tag{4.1}$$

where ρ and ρ_w are the effective rock resistivity and the resistivity of groundwater respectivively; ϕ is the porosity; S is the volume fraction of pores with water; a, m and n are are constants with $n \approx 2.0$, $1.3 \leq m \leq 2.5$ and $0.5 \leq a \leq 2.5$.

4.3 Basic Principles of Electrical Resistivity

Electrical resistivity surveying is fundamentally based on Ohm's law which controls the flow of current in a conducting medium. According to Ohm, the current I that flows in a conductor is proportional to the voltage U across it:

$$U = IR \tag{4.2}$$

The constant of proportionality, R, is the resistance of the conductor. For a given conductor the resistance is proportional to the length L and inversely proportional to the cross-sectional area A of the conductor (Figure 4.2).

$$R = \rho \frac{L}{A} \tag{4.3}$$

the constant of proportionality ρ is the resistivity, which is a physical property that expresses the ability of the material to oppose the flow of currents. The inverse of the resistivity is called the conductivity σ of the material.

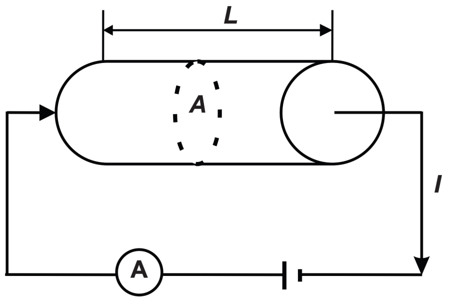

Figure 4.2 – A simple circuit diagram demonstrating Ohm's law

In the form of the current density J, the electric field intensity E and the conductivity σ, the Ohm's law can be written as:

$$J = \sigma E \tag{4.4}$$

The physical parameter that is measured on the field is the electric potential V and is related to the electric field intensity by the equation

$$E = -\nabla U \tag{4.5}$$

Putting equations (4.4) and (4.5) together we get

$$J = -\sigma \nabla U \tag{4.6}$$

The Dirac delta function for equation of continuity for a point in 3D is:

$$\nabla \cdot \vec{j}(x, y, z, t) = \frac{\partial q(x, y, z, t)}{\partial t} \delta(x)\delta(y)\delta(z) \tag{4.7}$$

where t is time and $\vec{j}$ is the current density vector. Dey and Morrison (1979a) gave the relationship between the current and the current density for the three spatial dimensions x, y, and z as:

$$J = \left(\frac{I}{\Delta V}\right) \delta(x - x_s)\delta(y - y_s)\delta(z - z_s) \tag{4.8}$$

where ΔV is the elemental volume, δ is the Dirac delta function and I is the source current located at (x_s, y_s, z_s). From equations (4.6) and (4.8) we have

$$-\nabla \bullet [\sigma(x, y, z)\nabla U(x, y, z)] = \left(\frac{I}{\Delta V}\right) \delta(x - x_s)\delta(y - y_s)\delta(z - z_s) \tag{4.9}$$

The potential U at a distance r from a single point current source I (Figure 4.3a) of a homogeneous subsurface is related to the resistivity by the equation:

$$U = \frac{\rho I}{2\pi r} \tag{4.10}$$

Practically, it is not possible to use a single electrode for resistivity measurements, at least an additional electrode is needed. For an electrode pair with current I at electrode C_1, and -I at electrode C_2 (Figure 4.3b), the potential at a point is given by the algebraic sum of the individual contributions

$$U = \frac{\rho I}{2\pi} \left[\frac{1}{r_1} - \frac{1}{r_2} \right] \tag{4.11}$$

On the field it is the potential difference between two points that is measured. Due to contact resistance, it is not advisable to use the same pair of electrodes as current and potential simultaneously. High-impedance voltmeters are used to measure the voltage across the potential pair of electrodes in order to avoid contact resistances. Figure 4.4 shows a typical practical arrangement and the potential is given as:

$$U = \frac{\rho I}{2\pi} \left[\frac{1}{r_1} - \frac{1}{r_2} - \frac{1}{r_3} + \frac{1}{r_4} \right] \tag{4.12}$$

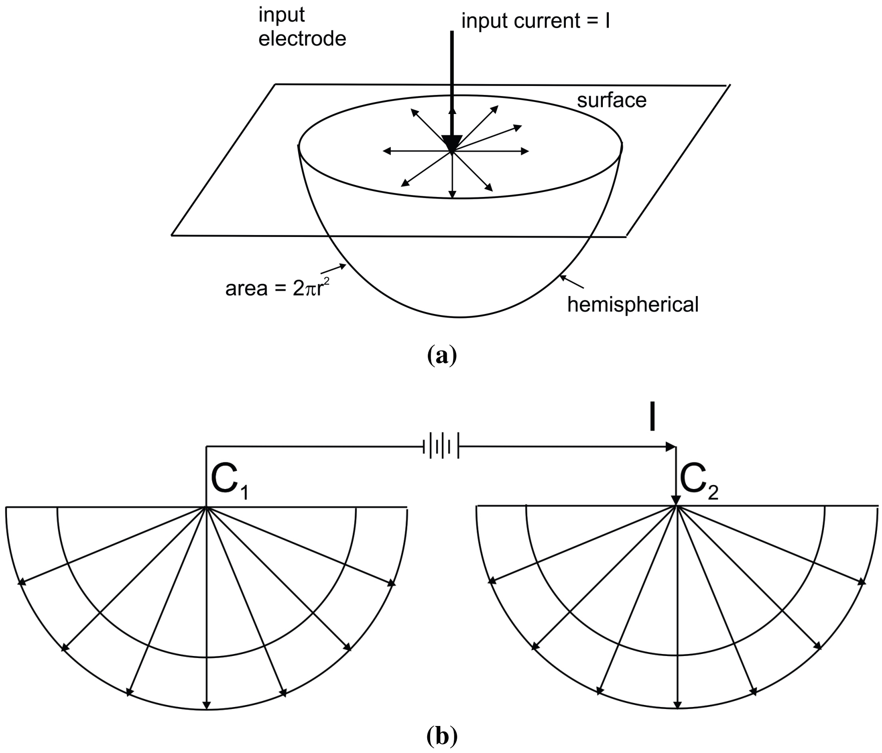

Figure 4.3 – Sketch of potential distribution caused by (a) a point current source and (b) a pair of current electrodes (Lowrie, 2007)

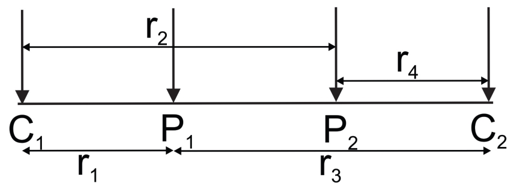

Figure 4.4 – Sketch of a typical four electrode arrangement for measurement

From equation (4.12), the apparent resistivity can be written as:

$$\rho = k\frac{\Delta U}{I} \tag{4.13}$$

and k is

$$k = \frac{2\pi}{\left(\frac{1}{r_1} - \frac{1}{r_2} - \frac{1}{r_3} + \frac{1}{r_4}\right)} \tag{4.14}$$

where k is the geometric factor and it depends on how the potential and current electrodes are arranged.

4.4 The electrode arrays

There are different arrays in electrical resistivity surveying based on the arrangements and/or separation of the current and potential electrodes. Figure 4.5 shows six of the commonly used arrays: Wenner, Schlumberger, Gradient, Dipole-dipole, Dipole-pole, Pole-pole and equations (4.15) to (4.20) give the expression for their apparent resistivities. C_1 and C_2 are current electrodes and P_1 and P_2 are potential electrodes.

For the Wenner configuration the spacings between the current and potential electrodes are the same (Figure 4.5a). The apparent resistivity for the Wenner array is:

$$\rho_a = 2\pi a \left(\frac{\Delta U}{I} \right) \tag{4.15}$$

The Wenner array is very sensitive to vertical changes in the subsurface (resolving horizontal structures) but less sensitive to horizontal changes (resolving vertical structures). The signal to noise ratio is very high for this array.

For the Schlumberger (gradient) array the potential electrodes are within the current electrodes (Figures 4.5b and 4.5c) and the apparent resistivity is:

$$\rho_a = \frac{\pi}{a} \frac{(L^2 - x^2)}{(L^2 + x^2)} \left(\frac{\Delta U}{I} \right) \tag{4.16}$$

For a symmetrically arranged Schlumberger array $x = 0$ (x is the separation between the midpoints of the current and potential electrodes), and the equation reduces to:

$$\rho_a = \frac{\pi L^2}{a} \left(\frac{\Delta U}{I} \right) \tag{4.17}$$

The Schlumberger array resolves vertical structures better than the Wenner array and penetrates deeper than the Wenner.

The gradient array Figure (4.5c) is similar to the Schlumberger array with the current electrodes at the extreme ends and the potential electrodes within them. In taking the measurements, the potential pair is moved between the current pair.

In the dipole–dipole configuration, potential pair of electrodes are placed at one side of the survey line and the current pair of electrodes are at the other side of the line (Figure 4.5d). The apparent resistivity for this array is:

$$\rho_a = \pi n(n+1)(n+2) a \left(\frac{\Delta U}{I} \right) \tag{4.18}$$

The dipole–dipole configuration is very sensitive to horizontal changes in the subsurface (resolving vertical structures) but less sensitive to vertical changes (resolving horizontal structures). The signal strength for this array is low.

The pole–dipole array (Figure 4.5e) is an asymetrical array and one of the current electrodes is placed at a great distance from the other three. The apparent resistivity for this array is:

$$\rho_a = 2\pi n(n+1) a \left(\frac{\Delta U}{I} \right) \tag{4.19}$$

This array has a signal strength higher than that of the dipole–dipole.

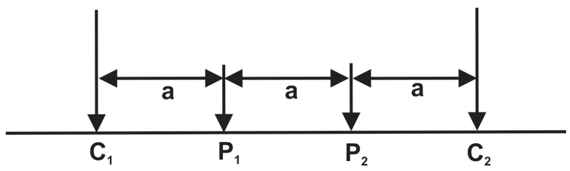

(a) Wenner array

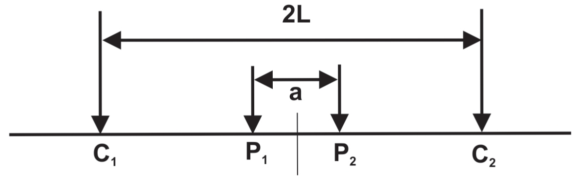

(b) Schlumberger array (symmetrical)

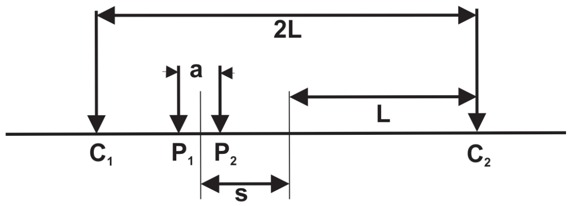

(c) Gradient array (asymmetrical Schlumberger array)

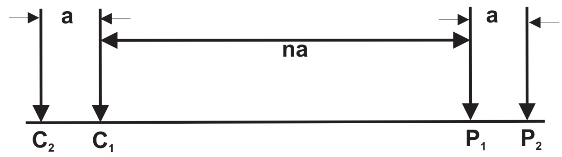

(d) Dipole–dipole array

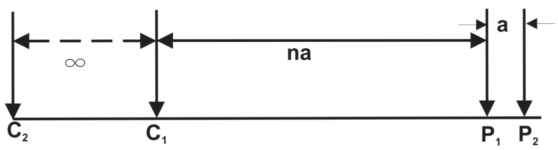

(e) Pole–dipole array

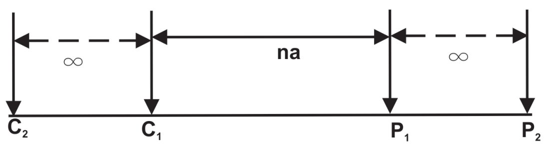

(f) Pole–pole array

Figure 4.5 – Basic electrode arrangements used in DC resistivity surveying

For the pole–pole configuration (Figure 4.5f) the second current and potential electrodes are placed at a distance not more than twenty times the separation between the first current and potential electrodes. The apparent resistivity for the pole–pole array is:

$$\rho_a = 2\pi a\left(\frac{\Delta U}{I}\right) \tag{4.20}$$

This array has the deepest depth of investigation but the resolution is very poor.

For detailed description of the resistivity methods, the reader is kindly referred to sources like (Telford et al., 1990; Reynolds, 1997; Kearey et al., 2002; Milsom, 2003; Lowrie, 2007; Sharma, 1997) for more information.

4.5 Electrical Resistivity Tomography (ERT)

4.5.1 Introduction

Traditionally, the two fundamental modes of electrical resistivity surveying are the profiling and the sounding. In the electrical resistivity profiling mode, the midpoint is varied and the electrode separations are fixed for the measurement. This technique is used for mapping lateral variations in resistivity. The data from such a survey can either be presented as a profile or as a cotour map and the depth of investigation is constant. The other mode is the vertical electrical sounding (VES), in this mode, the midpoint is the same and the electrode spacing is systematically increased. As the electrode separation is increased, the current is forced deeper into the subsurface and information on resistivities at the different depths are obtained. The actual depth of penetration depends on factors such as the type of array, the resistivity as well as how the subsurface is layered. The set up for the VES and the profiling consist of four electrodes, four reels of insulated cables, a battery and the resistance meter. The problem of the four electrode system is moving the electrodes with long spread of wire attached after each measurement. The time spent in moving the cables slows down the work and makes it expensive.

Most applications in geophysics require high resolution subsurface resistivity information in 2–D and 3–D. In the Electrical Resistivity Tomography (ERT) method, the sounding and the profiling techniques are integrated to give information on both the lateral and vertical extent of the subsurface. The ERT gives images either in 2–D or 3–D depending on how the data is acquired. Resistivity imaging is becoming increasingly popular in electrical exploration, due to its ability to produce images of the subsurface efficiently and effectively as a result of the availability of automated data-acquisition systems and efficient user friendly inversion softwares.

4.5.2 The ERT Principles and Applications

The ERT is a multi-electrode system and the spacing between the electrodes remains the same, but the separation between the potential and the current electrodes varies depending on the electrode configuration. The electrodes are arranged on a line and are connected to a multi-core cable which is connected to a selector and then to the resistivity meter or from the cable to resistivity meter directly. The resistivity meter automatically determines the separation and also which electrodes are to be used as current pair and potential pair. The meter measures the apparent resistivities by using a range of different electrode separations and midpoints, a typical example is shown in Figure 4.6a.

The apparent resistivity values are normally presented in pictorial form using pseudosections (4.6a) which give approximate pictures of the subsurface resistivity distributions. The shape of the pseudosection contours depends on the type of array used. Pseudosection is used for data analysis and quantitative data interpretation. Poor apparent resistivity measurement (noisy data) can be identified and removed with ease since they stand out. The roll-along survey technique is employed when there is a limited number of electrodes and cables to extend horizontally the area to be covered by the survey (4.6b). The roll-along is done by moving the cable past one end of the line by several units of electrode spacing after the first set of measurements. Measurements for the roll-along stations are normally faster than the first station because the number of data to be collected are less as a result of data overlap and only data which do not overlap are measured.

ERT surveys can be carried out using different electrode arrays, such as gradient, square, dipole-dipole, Wenner, Schulumberger, etc. The electrodes are placed on the surface to send the electric current into the ground and the resulting voltage signals generated as a result are measured. It has been used to investigate areas of complex geology, such as volcanic and geothermal areas, landslides, seismotectonic structures, and areas of hydrogeologic phenomena and environmental problems (Steeples, 2001; Colangelo et al., 2008; Lapenna et al., 2005; Griffiths and Barker, 1993).

The ERT method is widely applied to obtain 2–D and 3–D high-resolution resistivity images of

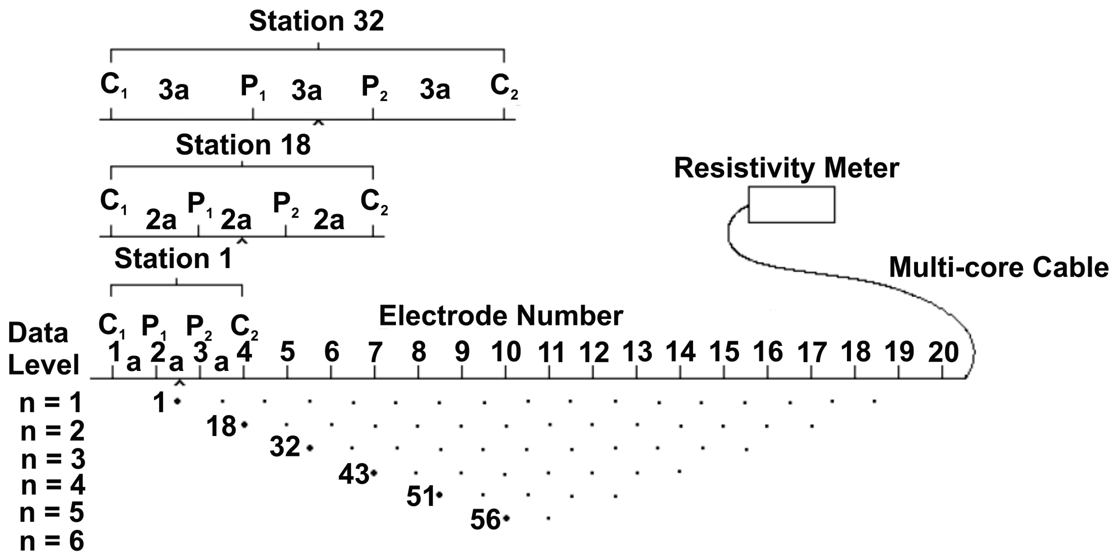

(a)

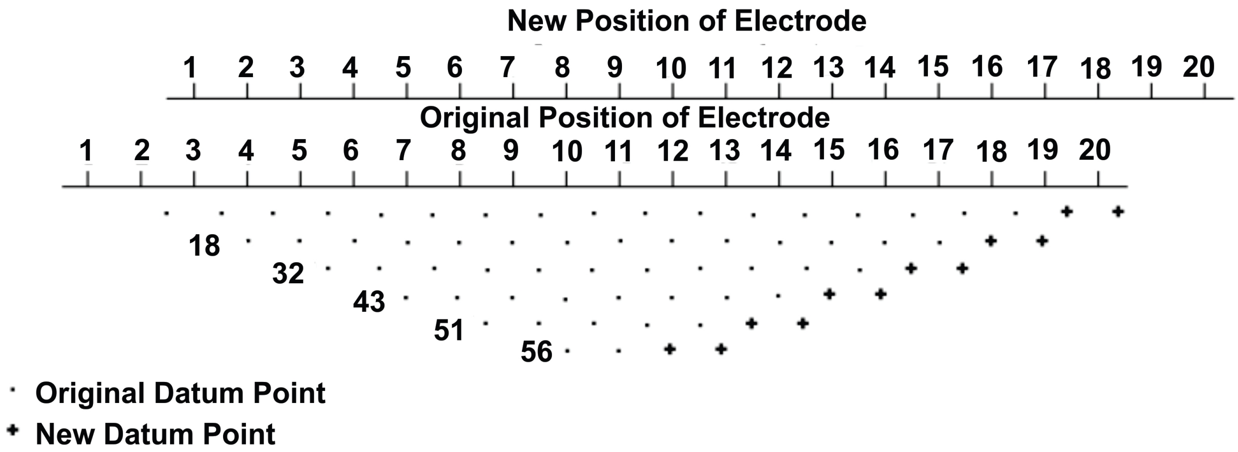

(b)

Figure 4.6 – Sketch of the (a) electrodes for the 2–D electrical survey and the sequence of measurements for building the pseudosection (b) use of the roll-along to extend the area covered by a 2–D survey (Loke, 2011)

the subsurface. The 2–D survey is the most widely used in comparison with the 3–D. The reason is that it is the economic compromise between keeping the cost down and getting accurate images (Dahlin, 1996). Figure 4.7 shows a typical high resolution 2–D resistivity image. The assumption that the subsurface is 2–D (resistivity does not change in the direction perpendicular to the survey line) when interpreting the data from a single profile is problematic. This assumption is only true if the survey is carried out across the strike of an elongated structure. There could be serious distortions in the lower sections of the model should there be significant variations in the subsurface resistivity in direction normal to the survey line (Loke, 2011).

With the development of innovative and robust inversion methods incorporating topography (Gunther et al., 2006; Loke and Barker, 1996b), accurate data interpretation for resolving complex geological problems, such as defining aspects of hidden underground structures (i.e. fractures, water accumulations, etc.) or studying the spatiotemporal evolution of groundwater flow relative to landslide phenomena has become easier. One of the major limitations of the technique today

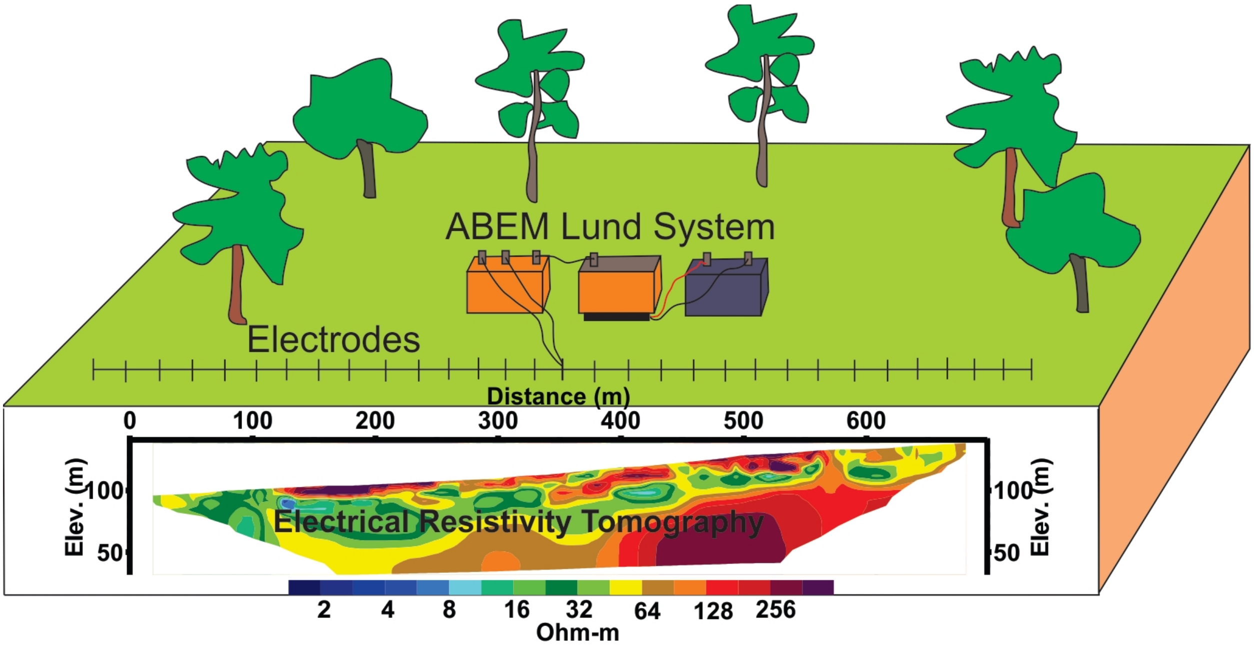

Figure 4.7 – Sketch of multi electrode array showing the set up and a possible electrical resistivity tomography obtained after inversion

is the time-consuming measurement process that tempts data-acquisition teams to reduce the data density in order to save expensive field operation time, which in turn can be devastating for the imaging quality.

4.5.3 The multi–electrode data acquisition with the gradient array

In the multi-electrode gradient surveying, a number of electrodes are arrayed in a straight line and attached to a multi-core cable (Figure 4.7). The potential electrodes are always within the current electrodes (Figure 4.8). The current is injected into the subsurface using a separation of $(s+2)a$ and all the corresponding voltages with potential electrodes spacing of a are measured simultaneously. s is an integer, and it gives the maximum number of potential readings for a current injection, and it also gives the maximum separation between the potential electrodes. The midpoint of the potential dipole m relative to the current pair electrodes is given as:

$$m = \frac{(x_M + x_N)/2 - (x_A + x_B)/2}{(x_N - x_M)} = \frac{(x_{MN} + x_{AB})}{a} \tag{4.21}$$

where x_A, x_B, x_M, x_N are the positions of the current and potential electrodes, and $x_B > x_A$, $x_N > x_M$ and x_{AB}, x_{MN} are the midpoints of the respective dipoles. m can also evaluated from the relation $m = n - (s+1)/2$, for $x_{MN} \leq x_{AB}$ $(m \leq 0)$ for and $m = n + (s+1)/2$, for $x_{MN} \geq x_{AB}$ $(m > 0)$, where n and m are negative or positive integers (Dahlin and Zhou, 2006).

Measurements using the multi-electrode system can be done either by a single – or a multi – channel. In the single–channel measurements, one potential reading is taken at a time for each current injection. In the multi – channel measurements, for example the four channel, four potential readings are taken at a time for each current injection. The multi – channel measurements are faster

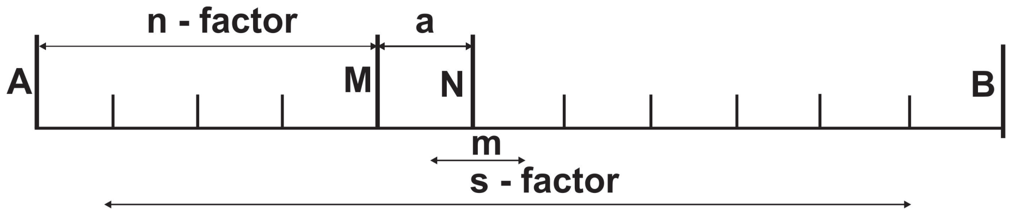

Figure 4.8 – Sketch of gradient array showing the position of the electrodes for a measurement with a current-electrode separation of $(s + 2)a$, where separation factor $s = 9$, the $n = 4$, n is the smallest relative spacing between a current electrode and a potential electrode and the midpoint factor $m = -1$

and as a result cost effective and this makes the gradient array a better option to the Wenner array which can only use one–channel. The density of data is higher in the multi – channel than the single – channel. Dahlin and Zhou (2004) concluded that the resolution of the multi–electrode gradient array is as good as the best of the convectionally used arrays and two years later Dahlin and Zhou (2006) reported again that the gradient array's resolution is better than or as good as that of the Wenner array. Stummer et al. (2004) reported that if the array gives a greater data density than the Wenner array, then it is good for the resolution. The quality of the inverted models can be compromised if the data density is less and there are loss of data due to may be skipped electrodes and if there are also large number of noisy data points. The gradient array would be a better option for the multi – channel measurement as compared to the dipole-dipole because the latter suffer from higher noise levels for longer electrode separations. (Dahlin and Zhou, 2006).

4.5.4 ERT in the study of Impact Craters

Although ERT is becoming increasingly popular in electrical exploration, as a result of its ability to produce high resolution images of the subsurface, it is hardly being used in impact cratering science. The only availabile data is the work by ***The Geological Society of America*** and the findings were published by Tong et al. (2010; 2012). They used ERT to study the deposition and flow of impact melt and breccias over the central uplift of the Araguainha impact structure in Brazil. They used the dipole-dipole array with eight electrodes (six current and two potential) and the electrode separation was 50 m.

From their results, they delineated the granite (150 Ωm $< \rho <$ 250 Ωm) and sedimentary ($\rho >$ 250 Ωm) boundary (solid white lines in Figure 4.9a) and also mapped the fracture (zone with the dotted white line (Figure 4.9a)). They reported that the fracture is possibly filled with lithologic materials. They were also able to demarcate the boundary between the granite and the impact breccias and characterize three distinct resistivity anomalies within the impact breccias (Figure 4.9b). They interpreted the low resistivity zones (LRZ) to represent the matrix of the polymict breccia, the high resistivity blocks (HRB) as impact melt and the anomalously high resistivity regions (XHR) as the target sedimentary rocks because of their resistivity and dimensions.

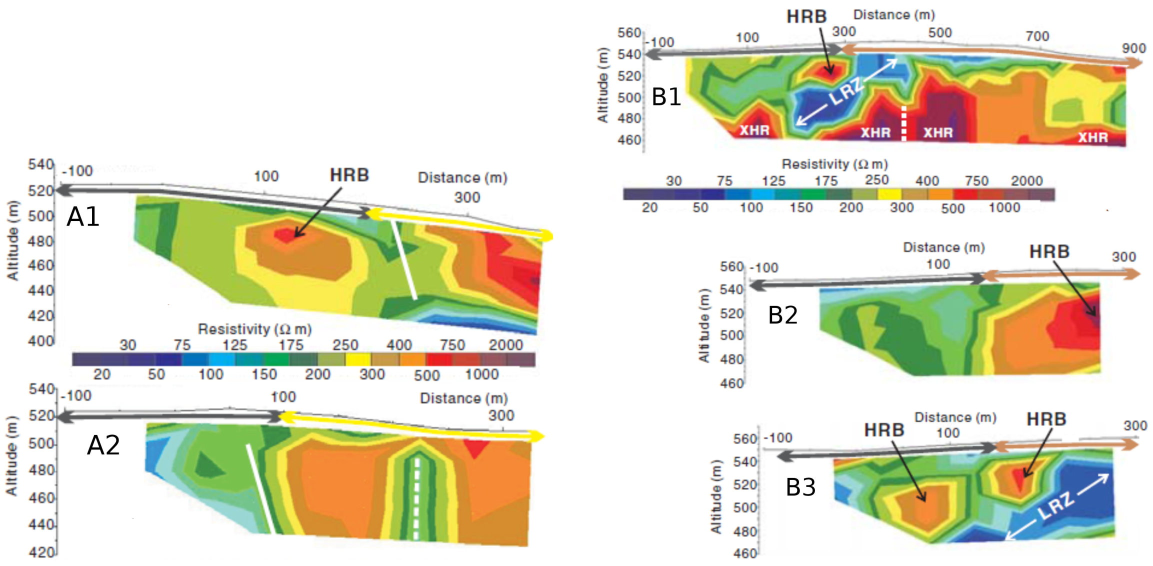

(a) Electrical images at the granite-sediment boundary

(b) Electrical images at the granite-polymict breccia boundary

Figure 4.9 – Profiles of electrical resistivity tomography of the Araguainha impact structure, Brazil. The arrow lines at the top of the images indicate the extent of the regions: granite (black), sediments (yellow) and polymict breccia (brown), (Tong et al., 2010)

.

4.6 The forward modelling and inversion

In the electrical resistivity inverse problem, the attempt is made to determine an appropriate distribution of subsurface resistivity that could have given rise to the resistivity survey data. Finding a solution to the inverse problem is the principal difficulty because of its inherent non-uniqueness and the number of models that can adequately reproduce the field data. The inversion method basically tries to fit the observed survey data to within a degree justified by their estimated uncertainties. The model is the mathematical relationship between the data and model parameters: resistivity and depth (the physical quantities that one is attempting to estimate). Iterative optimization is to find model adjustments that will minimize the difference between the measured and predicted data.

The analytical, boundary element and finite-difference (FD) and finite-element (FE) methods are the three main methods used to calculate the apparent resistivity values for a particular model. The (FD) and (FE) methods are commonly used because the analytical method works well with only simple geometries and the boundary element methods does not work well when there are higher numbers of regions with different resistivity values. The reader is referred to Dey and Morrison (1979a;b) and Silvester and Ferrari (1990) for the mathematical details of the equations for the FD and the FE methods used in evaluating the 2–D and 3–D resistivity models.

Application of the FE method to EM and resistivity has been given by Pridmore et al. (1981) and Sasaki (1994) has developed an algorithm to inverse data using the FE approach for the forward problem. Lesur et al. (1999a) have used the boundary element method which is a simplified form of the FE technique for crosshole tomography. Lowry et al. (1989) and Zhao and Yedlin

(1996) have provided a more efficient alternative solution to the FD method proposed by Dey and Morrison (1979a) and Spitzer (1995) which had a singularity problem. Menke (1984) minimized the least-squares equation so that the difference between the observed and the predicted data is reduced. This form of inversion is called the Gauss-Newton method:

$$J^T J \Delta q_i = J^T g \tag{4.22}$$

The problem with this inversion method is that if the inversion starts with a poor initial model, the values calculated can be unrealistic. The introduction of the parameter, λ, called Marquardt or damping factor into the Gauss-Newton equation (4.22) constrained the values of the parameter change vector (Marquardt, 1963; Levenberg, 1994; Lines and Treitel, 1984).

$$(J^T J + \lambda I)\Delta q_k = J^T g \tag{4.23}$$

This method is called the Marquardt-Levenburg or ridge-regression method (Inman, 1975). In 2–D and 3–D inversions where the model parameters are large and have many small cells, the model produced by this equation can be misleading. To stabilize the inversion, the Occam's inversion (Constable et al., 1987) is used where the model parameters change in a gradual manner. The Res2DInv uses the L_2– *norm* (smoothness-constrained least-squares method) (Ellis and Oldenburg, 1994) inversion routine to estimate the true resistivity of the subsurface structure. The inversion routine is implemented by the equation:

$$(J^T J + \lambda F)\Delta q_k = J^T g - \lambda F q_k \tag{4.24}$$

where $F = \alpha_x C_x^T C_x + \alpha_z C_z^T C_z$, C_x and C_z are the horizontal and vertical roughness filter respectivively, J is the Jacobian matrix of partial derivatives, J^T is the transpose of J, λ is the damping factor, q is the model change vector and g is the data misfit vector. The L_2– *norm* works very well where the resistivity contrast is gradual. A modified form of equation (4.24) called the L_1– *norm* (blocky or robust inversion method) based on equation (4.25) is used when the subsurface is known to have highly contrasting resistivities.

$$(J^T J + \lambda F_R)\Delta q_k = J^T R_d g - \lambda F_R q_k \tag{4.25}$$

$F_R = \alpha_x C_x^T R_m C_x + \alpha_z C_z^T R_m C_z$, R_d is the data misfit weighting matrix, and R_m is the model roughness weighting matrix.

The equations for the L_1– and L_2–*norms* have gone through several applications and modification from the Gauss-Newton equation (4.22) in order to improve upon it. These include: the perturbing effects due to a vertical dike using different arrays (Dey et al., 1975), classification of the array and the depth of investigation (Apparao et al., 1992), the resolutions of the arrays for 2D inversions (Beard and Tripp, 1995), the influence of data density on the results (Dahlin and Loke, 1998), first-order roughness filter (deGroot-Hedlin deGroot-Hedlin deGroot Hedlin and Constable, 1990) and the depth below which surface data are insensitive to physical property variations which is commonly called *depth of investigation index (DOI)* (Oldenburg and Li, 1999). These researchers have also worked on other aspects of the inversion: Claerbout and Muir (1973) altered (4.24) to minimise the absolute changes in the model resistivity for regions that are homogeneous internally but have sharp boundaries with other regions, Maurer et al. (1998) added stochastic constraints to the least-squares solution. For more information on the 2–D inversion, the reader is kindly referred to Wolke and Schwetlick (1988), Sasaki (1992), Olayinka and Yaramanci (2000), Smith et al. (1999) and Auken and Christiansen (2004), Møller et al. (2001), Mufti (1976), Lesur et al. (1999a), Lesur et al. (1999b), Lehmann (1995), LaBrecque et al. (1996), Tarantola (1987), Park and Van (1991), Li and Oldenburg (1994), Loke and Barker (1996a).

CHAPTER 5

METHODOLOGY

5.1 Design and Modification of the ABEM Cable and Fabrication of a Roller

The ABEM LUND Resistivity Imaging System was the equipment that was to be used for this research. The electrode cable system available was four 21 take-out cables spaced every 2 m (Figure 5.1a). When all the four cables were connected, the total length was 160 m and this could only probe to a depth of about 30 m. It was necessary to find a way to increase the length of these cables since it was practically difficult to acquire new extended set. The challenge was how to modify this 2 m take-out ABEM electrode cable in order to probe to a greater depth. A design (Figure 5.1b) was created and wires were made. In the fabrication, about 3.3 km of wire were cut into different lengths. These wires were joined to the take-outs of the original ABEM electrode cables to get electrode separation of 5 m and a total length of 400 m in order to probe to a depth of about 75 m.

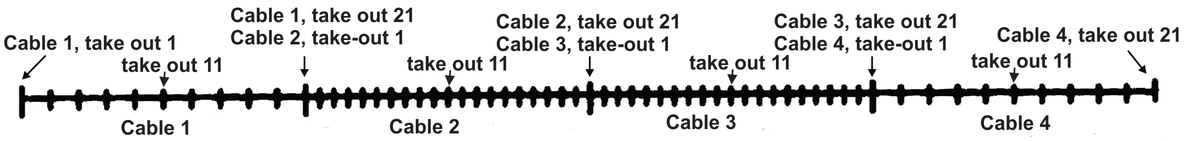

(a)

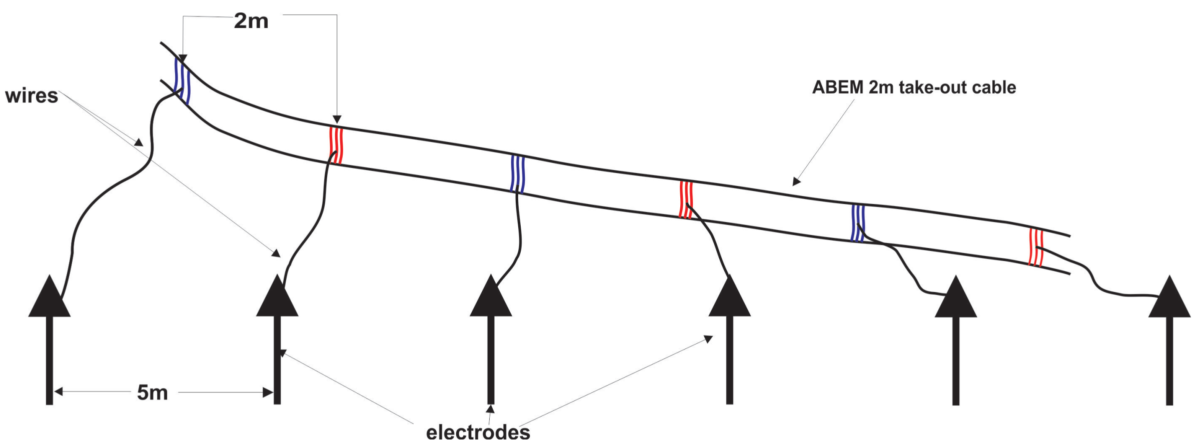

(b)

Figure 5.1 – Sketch of the (a) layout of the four cables (b) modified 2 m takeout ABEM cable and its connection

Wires were not cut for take-out *twenty one* of cable 1 and take-out *one* of cable 2 because that was the measurement station and they were to be connected to the station electrode. The lengths of wires cut were a meter longer than the actual separation between the cable take-out and the electrode, this was to compensate for the varied topography. As an example (Figure 5.2a), take-outs *eleven* of the inner cables (2 and 3) would be 20 m away from the station but their corresponding electrodes would be 50 m away. Wires of length 31 m were cut to make up the difference in separation of 30 m. The lengths of wires for the take-outs *twenty one* of cable 1 and *one* of cable 2 and take-outs *twenty one* of cable 3 and *one* of cable 4 were the same (61 m) because they were to be connected to the electrodes 11 and 31 which are equally spaced from the center (Figures 5.2a and 5.2b).

The lengths of the wires that were added to the four cable take-outs are as shown in Tables 5.1 and 5.2 and they were based on the selected protocols. The multi-electrode gradient array was used for acquiring the data and the GRAD4LX8 and GRAD4S8 protocols were selected. For the GRAD4LX8 protocol (long layout), all the four cables would be used and only the odd-numbered take-outs would be connected for the measurements (Figures 5.2b and 5.3). The take-out separation for the odd-numbered take-outs of the 2 m take-out ABEM cables are 4 m but the electrodes were to be 10 m apart so there was the need to add wires to make up for the differences. For the GRAD4S8 protocol (short layout), only the inner cables were to be employed for the measurements and all the take-outs were to be used (Figures 5.2a and 5.3). The cable take-out separation is 2 m and the electrode spacing for this arrangement was to be 5 m. Two each of the same length of wire were cut for each of the protocols GRAD4LX8 and GRAD4S8, one for cables on the left side of the station of measurements and the other for those on the right side.

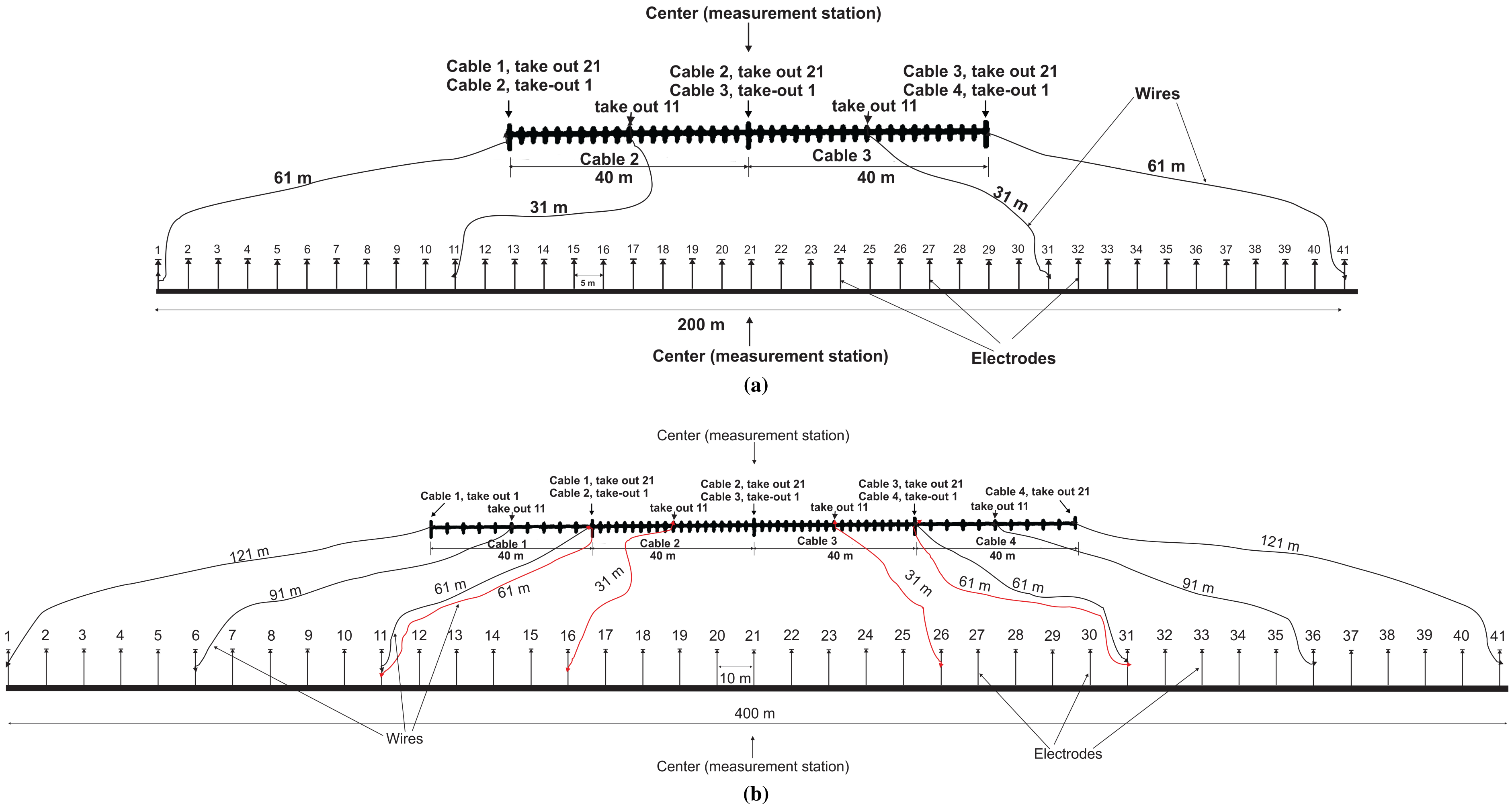

Figure 5.2 – Sketch of the connection for (a) short layout (GRAD4S8) and (b) long layout (GRAD4LX8). The red wires are used for both the long and short layout measurements

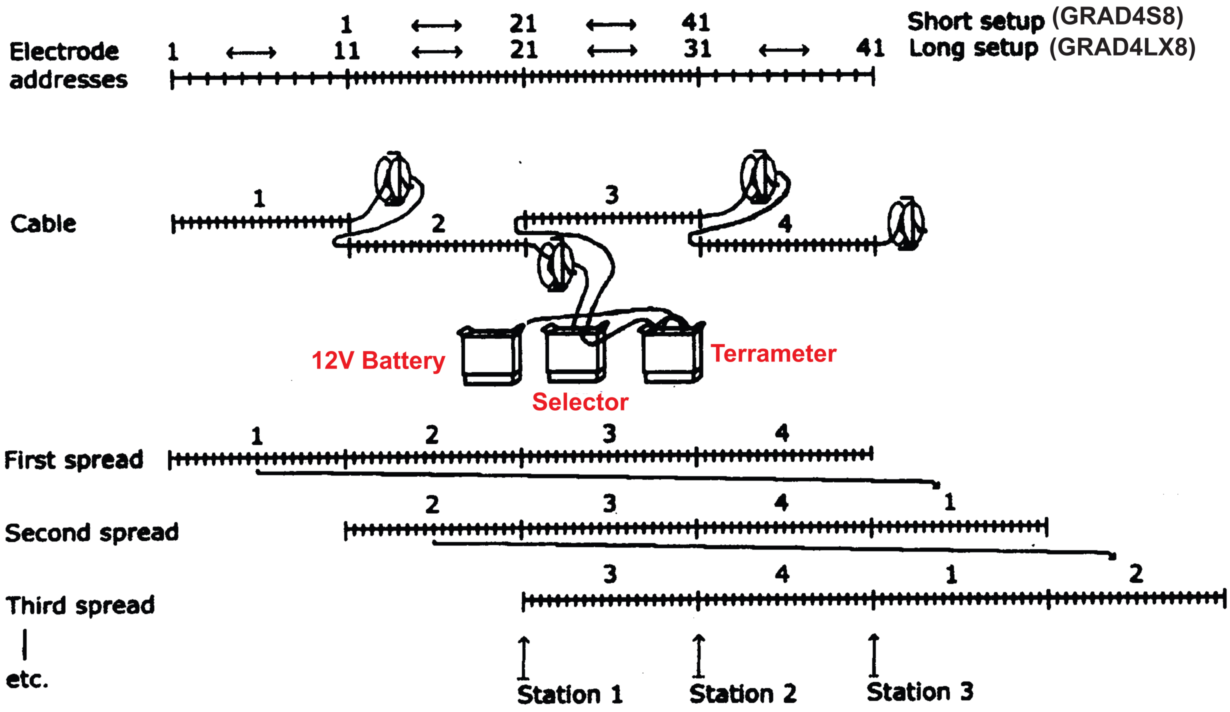

Figure 5.3 – Roll-along technique using four electrode cables. Modified from (ABEM, 2008)

The design and fabrication of the wires was successful because I had earlier on used the *SYSCAL-R1 PLUS* for the fieldwork at the maar of Beaunit at "Chaîne des Puys", France. This equipment uses a bunch of 16 wires and all the wires are connected to a ***multinode*** (Figure 5.4) at one end and the ***multinode*** is connected to a remote control multiplexer and then to the *SYSCAL-R1 PLUS*. At the other end of the bunch, the wires take out at 5 m interval. Unlike the *SYSCAL-R1 PLUS* where all the 16 wires take-out at the same point at one end where they are connected to the multinode and at different intervals at the other end, the take-outs for this one are different for both ends. For the long layout, the take-outs are at 4 m (to be connected to the odd-numbered takeout) and 10 m (to be connected to the electrodes) intervals towards and away from the station respectively. And, for the short layout, it is 2 m (to be connected to the even-numbered takeout) and 5 m (to be connected to the electrodes) intervals towards and away from the station respectively.

The Laboratoire Interactions et Dynamique des Environnements de Surface (IDES) de Universitè Paris Sud, Orsay, France has a roller that was used in the field to roll and unroll this long bunch of wires. The designed and fabricated roller shown in Figure 5.5 follow the model of the one at IDES.

Table 5.1 – Length of the wires for the 2 inner cables

Cable 3 take-out	Cable 2 take-out	Take-out separation (m)	Electrode position (m)	Difference in Length (m)	Actual Length of wire (m)
1	21	0	0	0	0
2	20	2	5	3	4
3	19	4	10	6	7
4	18	6	15	9	10
5	17	8	20	12	13
6	16	10	25	15	16
7	15	12	30	18	19
8	14	14	35	21	22
9	13	16	40	24	25
10	12	18	45	27	28
11	11	20	50	30	31
12	10	22	55	33	34
13	9	24	60	36	37
14	8	26	65	39	40
15	7	28	70	42	43
16	6	30	75	45	46
17	5	32	80	48	49
18	4	34	85	51	52
19	3	36	90	54	55
20	2	38	95	57	58
21	1	40	100	60	61

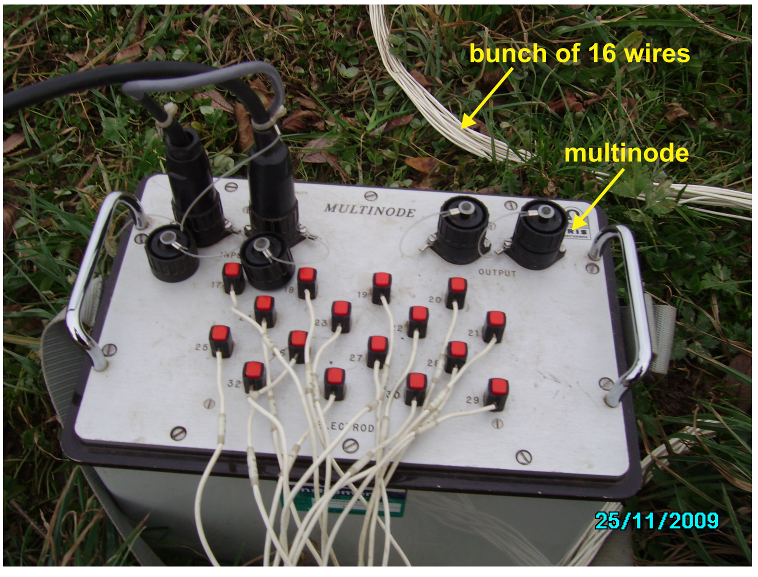

Figure 5.4 – SYSCAL-R1 PLUS multinode

Table 5.2 – Length of the wires for the 2 outer cables

Cable 4 take-out	Cable 1 take-out	Take-out separation (m)	Electrode position (m)	Difference in Length (m)	Actual Length of wire (m)
1	21	40	100	60	61
3	19	44	110	66	67
5	17	48	120	72	73
7	15	52	130	78	79
9	13	56	140	84	85
11	11	60	150	90	91
13	9	64	160	96	97
15	7	68	170	102	103
17	5	72	180	108	109
19	3	76	190	114	115
21	1	80	200	120	121

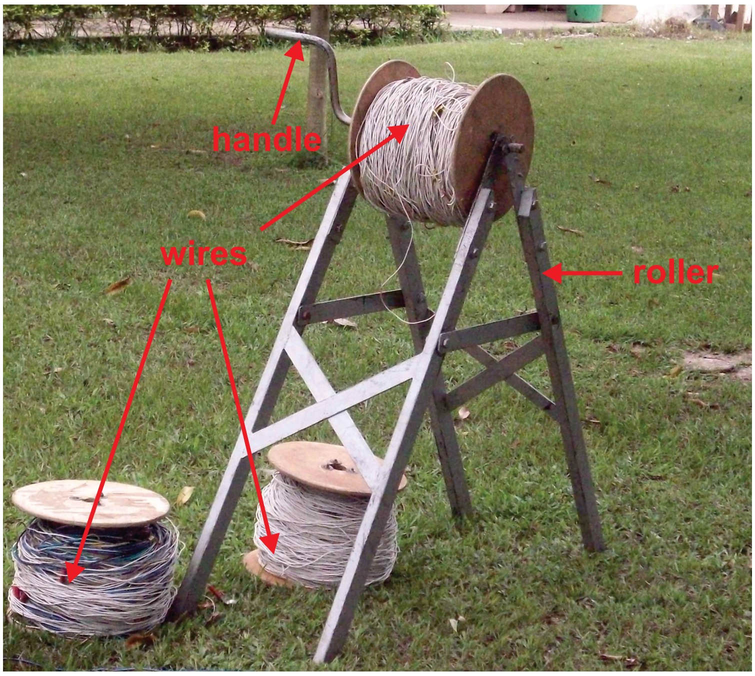

Figure 5.5 – Diagram of the roller

5.2 Data Acquisition

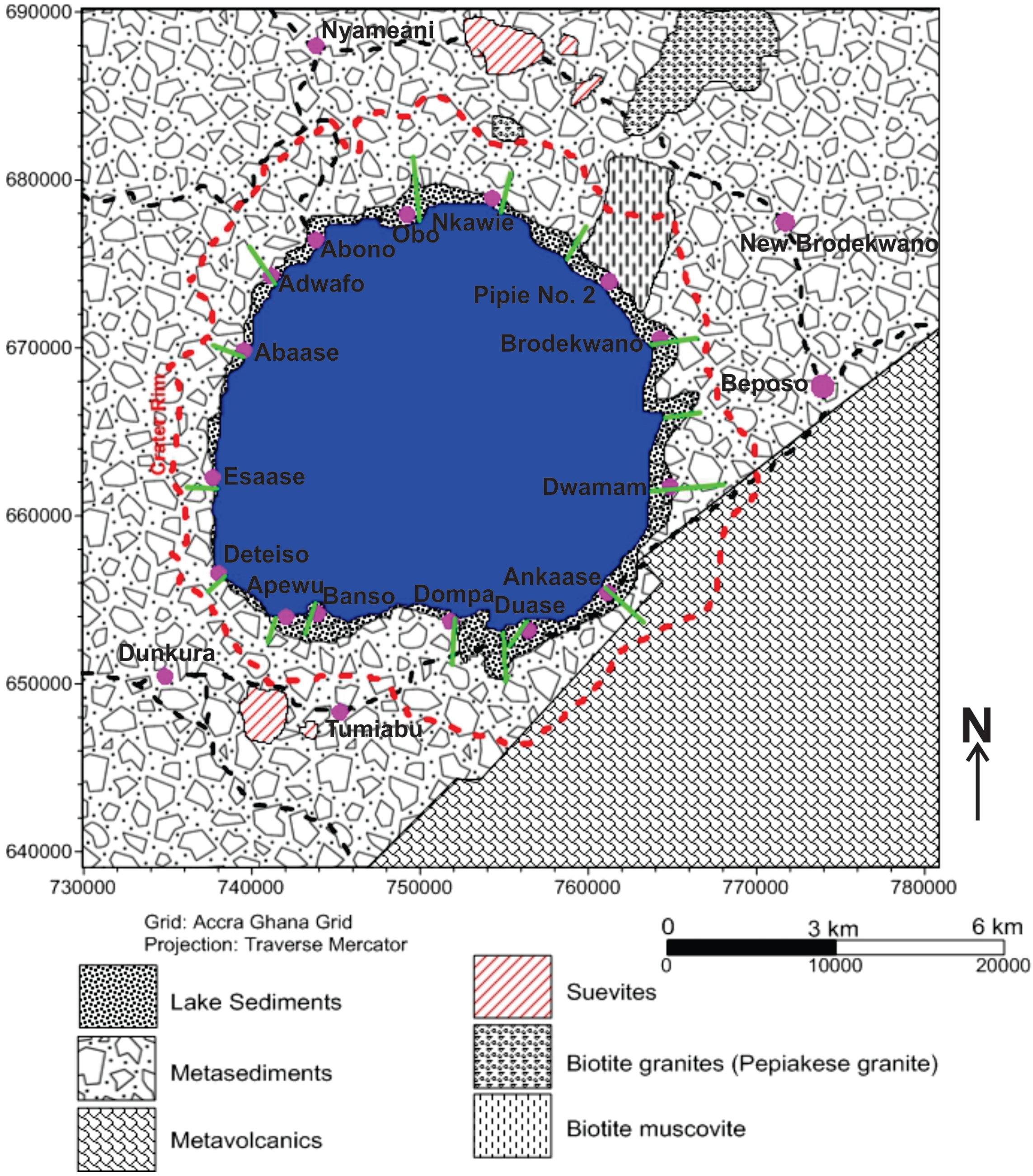

Figure 5.6 – Geological map of Bosumtwi showing the profile lines in green. Modified from (Koeberl and Reimold, 2005)

Sixteen electrical resistivity tomograms data sets were acquired radially around the lake (Figure 5.6) starting from the shore uphill towards the rim (Figure 5.7) of the crater at this topographically varied environment. The modified ABEM LUND Resistivity Imaging equipment was used to acquire the data. It consisted of the Terrameter SAS4000, the electrode selector ES 10-64C, 12V car battery four cables, four bundles of wires, eighty four stainless steel electrodes, seventy five electrode jumpers and about a hundred clips. Walkie-talkie and GPS were for communication and location of the profiles. As previously mentioned, each cable has twenty one electrode take-outs giving a total of eighty four electrode take-outs for the four cables, but the last and the first electrode take-outs overlap at the cable ends. The minimum profile length was 400 m and the maximum was

1,200 m (using the roll along technique).

(a) (b) (c)

Figure 5.7 – The modified ABEM LUND resistivity imaging set up (a) wires at the coast stretching to the lake, (b) measurement station near the rim of the crater and (c) bunch of wires at a considerable height from the electrode

The GRAD4LX8 and GRAD4S8 gradient array protocols were used for this four channel measurements in that order (Table B.2). The GRAD4LX8 was for the long layout (Figures 5.3 and 5.2b) and all the four electrode cables were connected. The GRAD4LX8 was chosen because apart from the fact that it gives a dense near-surface cover and a slightly sparser measurement pattern at long electrode spacings, this protocol also takes Wenner-Schlumberger measurements data for the longest electrode separations in order to improve the resolution for the largest investigation depths which is necessary for this work. The GRAD4S8 is for the short lay out (cables 2 and 3) (Figures 5.3 and 5.2a) and is designed to supplement GRAD4LX8 data to enhance near surface resolution. All the electrode take-outs were connected in the GRAD4S8 protocol. The resistivity meter automatically switches the electrodes to serve as current or potential pairs. The selection of the protocols and the other inputs were done prior to going to the field.

The protocol file with *ORG* filename (Table 5.3) was used for the first set of measurements on every profile and the file with *UP* filename was used for the roll-along towards the rim (Table B.2). The data for the *UP* files was lower because of data overlap with the previous measurements (using the ORG file) and as a result measuring was much faster for consecutive stations at a roll-along than for the first one (ABEM, 2008).

Table 5.3 – Number of data points for 4 cable layout (ABEM, 2008)

Array type	Protocol name	Address file	No of data ORG	No of data UP	Total data for one layout
Gradient	GRAD4LX8	LONG	608	340	1080
	GRAD4S8	SHORT	248	160	

The stainless steel electrodes were driven into the ground with a small hammer at 5 m and 10 m spacings for the inner (2 and 3) and outer (1 and 4) (Figures 5.3, 5.2a and 5.2b) cables respectively. The separation was done using a measuring tape. The cables were laid and the end of the fabricated bunch of wires with take-outs separation of 4 m were connected to their respective cable take-outs. The other end of the wires with take-outs separation of 10 m were also connected to the corresponding electrodes. The ends of the wires that are to be connected to the cables were painted red to distinguished them from the ends to be connected to the electrodes. The paintings also speed up the work because the wires were rolled in the desired directions. In all thirty one electrodes were connected to the odd-numbered take-outs at electrode separation of 10 m making a total length of 300 m for the first set of measurements using the GRAD4LX8 (Figure 5.8). Cables 3 and 4 were connected using a cable joint with the grove facing the equipment. Cable 1 was not connected during the first set of measurements. The terrameter, the electrode selector ES 10-64C and the 12 V car battery were then connected between cables 2 and 3 to the set-up. Figure 5.9 shows the set up and connections for the measurements. The electrode resistance test was run first before the measurements to ensure that all the 31 electrodes were connected. In some cases the electrode test failed and water had to be poured under those electrodes and they were also hammered deeper to ensure they pass the electrode test. The GRAD4S8 measurements was carried out after the GRAD4LX8 one. Electrode test was also carried out for this short layout of forty one electrodes spaced 5 m apart (total length 200 m) before the measurements.

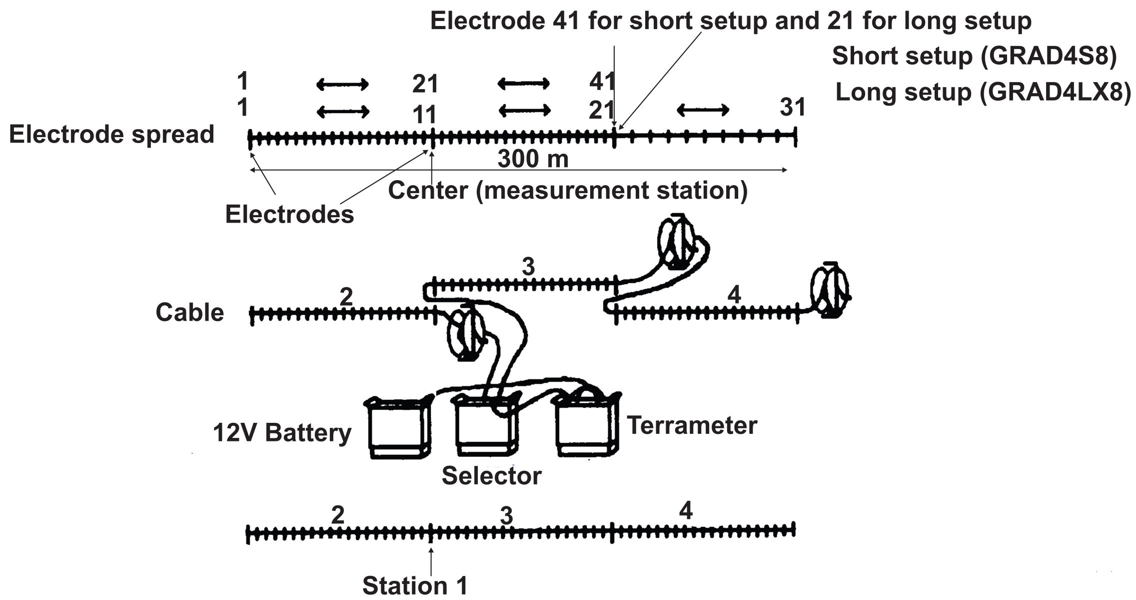

Figure 5.8 – Set up for first station measurements. Modified from (ABEM, 2008)

The roll-along technique (Figure 5.3) was employed on all the profiles in order to extend horizontally the area to be covered by the profile. Whilst the measurements were going on for the long lay out, twenty electrodes were fixed, ten of them midway between the electrodes in cable 4 and the rest at 10 m interval beyond the 4. It was not possible to just move one cable past the end of the cable towards the crater rim after the first set of measurements, because of the modification of the cable. The inner cables have 20 short extended wires (length between 4 and 61 m) (Table 5.1) whereas the outer cables have 11 long extended wires (length between 61 and 121 m) (Table 5.2). The whole set up has to be dismantled and moved 100 m towards the crater rim to be reconnected.

At the second, third and all the subsequent measurement stations so long as the profile was being extended, all the four cables were used for the GRAD4LX8 (Figures 5.10a and 5.10b) giving a total length of 400 m. Cable joints were used to connect first and second cables and the third and fourth cables and the groove on the cable joint used to connect them were facing the station. The terrameter, the electrode selector ES 10-64C and the 12 V car battery were connected between the second and third cables. The procedure described for the first set of measurements were repeated

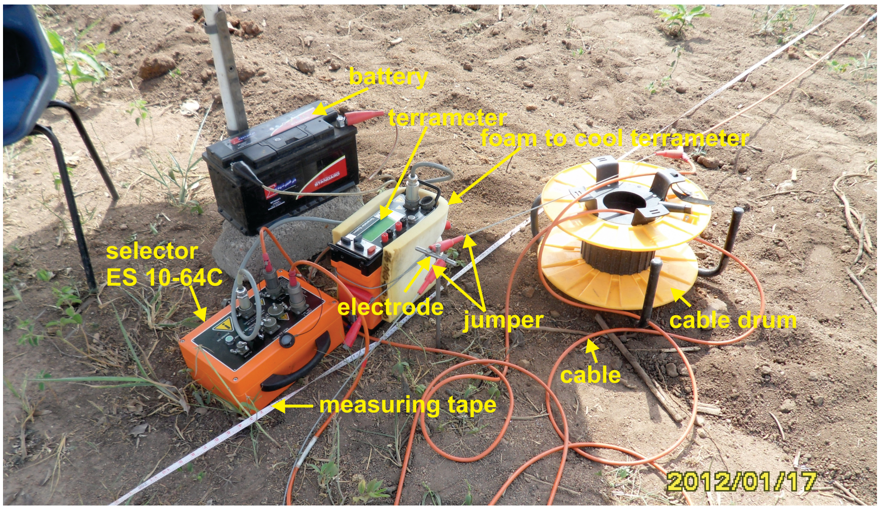

(a)

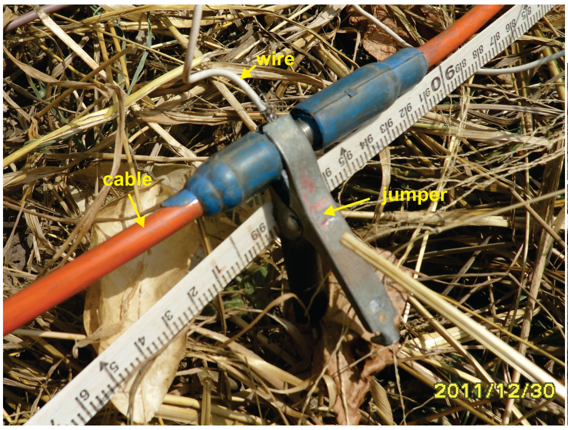

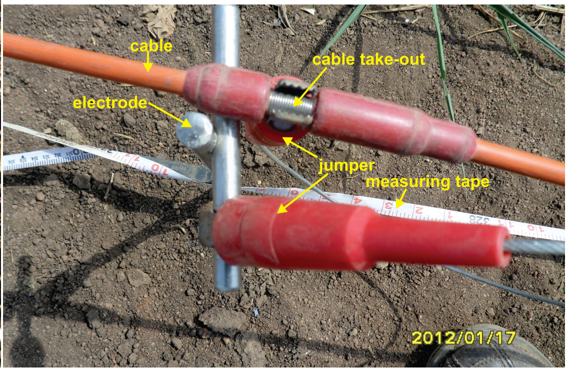

(b) (c)

Figure 5.9 – (a) The set up of the modified ABEM LUND resistivity imaging, (b) a jumper connecting a wire and the ABEM cable and (c) a jumper connecting a cable and a take-out

to acquire the data. The wires and in some cases the cables were tied to trees (mainly cocoa) with ropes so that they do not drift down the steep slope especially near the rim of the crater. At some some points jumpers were joined so that wires could be connected to the electrode (Figure 5.7c). GPS readings were taken at 10 m intervals.

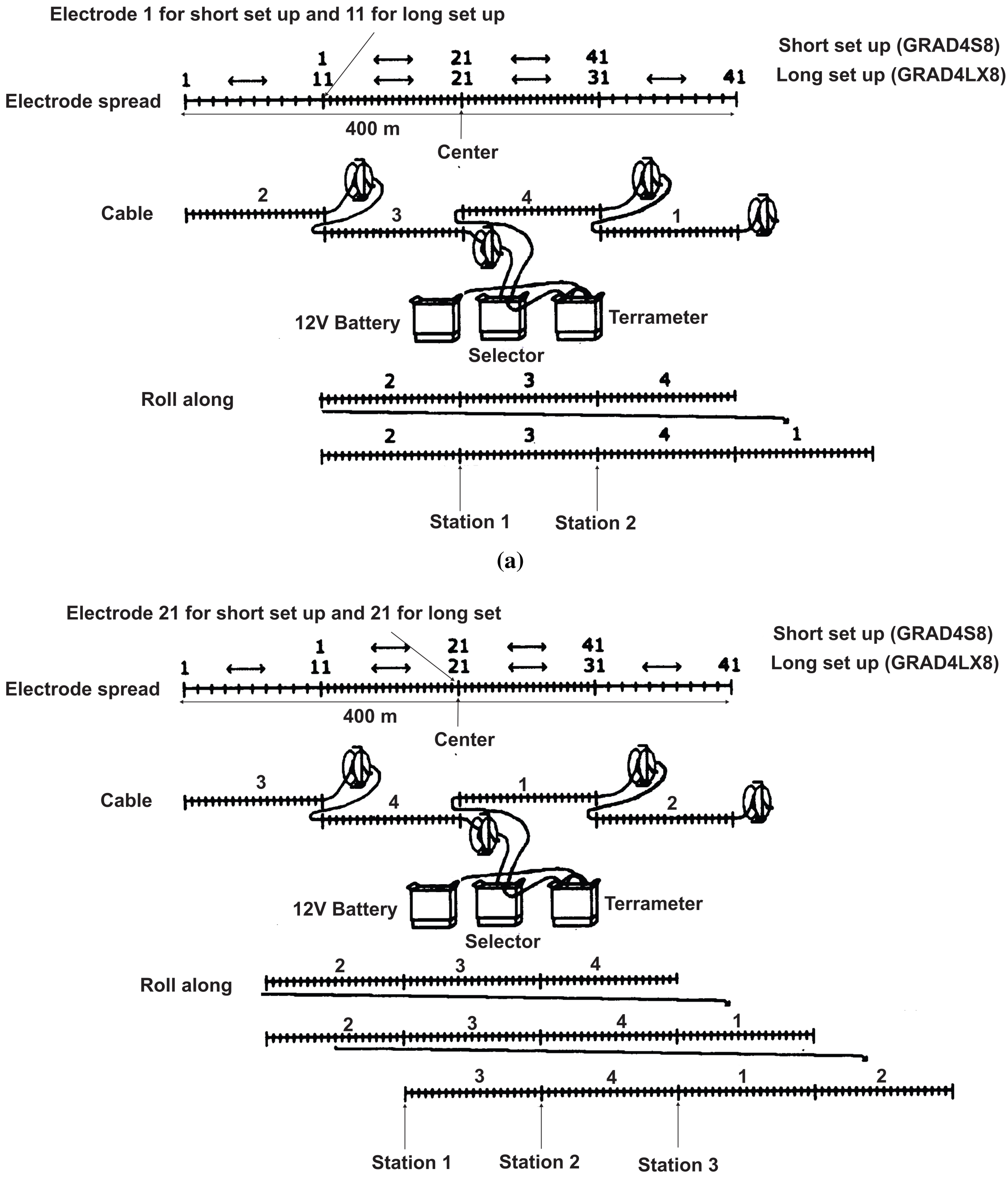

Figure 5.10 – Sketch of the connection for the (a) second and (b) third measurements stations. Modified from (ABEM, 2008)

Table 5.4 – Profile and profile length

Profile Name	Location	Length (m)
Obo	North	700
Nkawie	North-East	700
Mmem	North-East	700
Pipie	North-East	700
Brodekwano	East	600
Konkoma	East	500
Dwamam	East	1300
Ankaase	South-East	800
Duase 1	South-East	1200
Duase 2	South-East	400
Dompa	South	650
Banso	South-West	400
Apewu	South-West	400
Deteiso	South-West	500
Esaase	West	500
Abaase	West	500
Adwafo	North-West	700
Total		**11250**

Table 5.4 shows the profiles, their locations and lengths.

5.3 Data Analysis

The SAS4000/SAS1000 utility software, the RES2DINV, the Golden software SURFER 10 GRAPHICS and GRAPHER 8, Adobe photoshop CS5 and Corel draw GRAPHIC SUITE X5 were used in the analysis of the data. The sequence and the details of the analysis are given in this section.

5.3.1 The SAS4000/SAS1000 Utility Software and RES2DINV Data Analysis

The Terrameter SAS4000/SAS1000 utility software was used to retrieve the data from the terrameter and also to convert the data to RES2DINV format (.DAT file) for processing (Table B.3) and ABEM multi-purpose format (.AMP file) for documentation (Table B.1). The negative resistivity readings were rejected before the data were converted. Topographic data were added to the converted data (Table B.3).

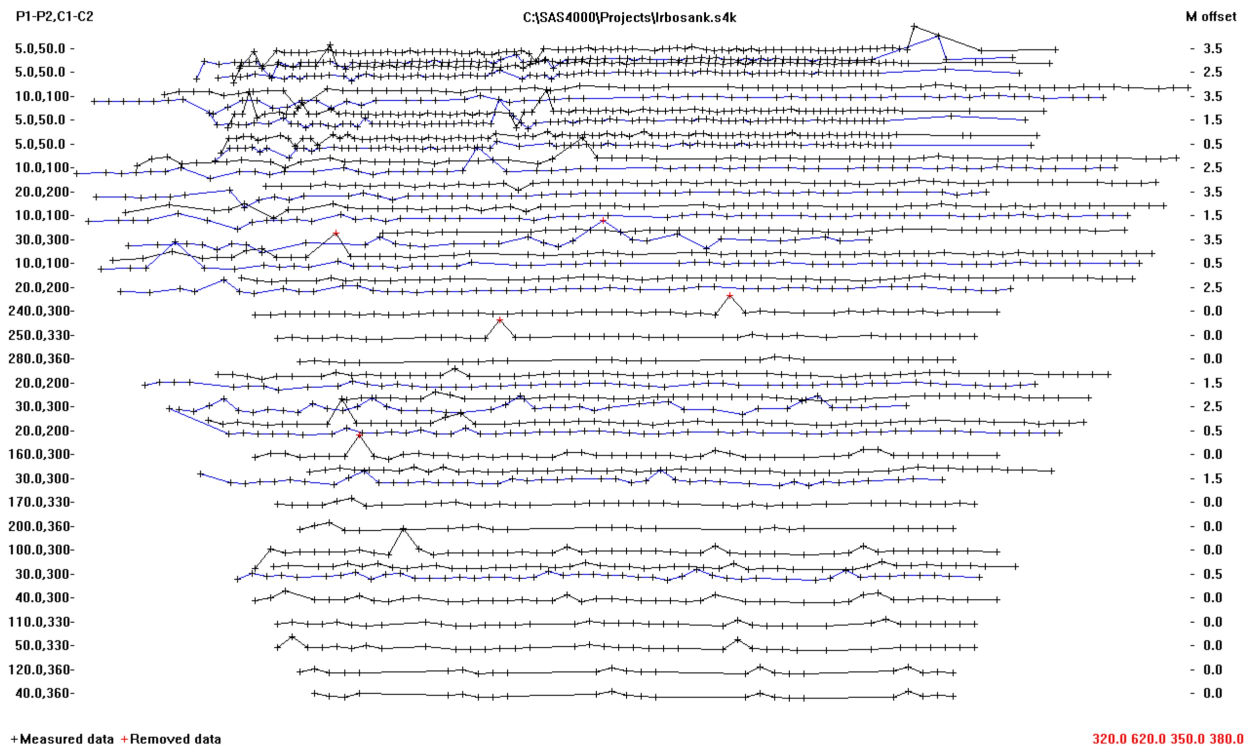

Figure 5.11 – Example of Multiple gradient array data with some bad data points

All the field data were inverted using the Res2DInv (version 3.59.106). The extremely low and high resistivity values were removed using the *Exterminate bad datum points* feature in Res2DInv for removing noisy data points. Bad data points were easily viewed as they appeared as stand out points (Figure 5.11) because the values were displayed in the form of profiles for each data level. These bad data points could be due to the failure of the relays at one of the electrodes, poor electrode ground contact due to dry, sandy or stony ground, attaching electrodes to wrong connectors, or shorting across the cables due to very wet ground conditions especially close to the lake shore. In some cases also preliminary inversion using the *robust inversion method* was employed followed by the *Display/Edit data/Estimate errors* to deal with the data quality.

Change settings/Use finite element method was used to calculate the apparent resistivities because all the data contained topography. The main objective of this research was to map the sediment/bedrock contact, so there was the need to sharply delineate this boundary as a result the L_1 *norm* (robust inversion) was employed. The L_1 *norm* also gives a more stable results (Zhou and Dahlin, 2003; Dahlin and Zhou, 2004). The *Gauss-Newton method* was used in calculating the sensitivity matrix for all the iterations. Talus are common around Lake Bosumtwi when you

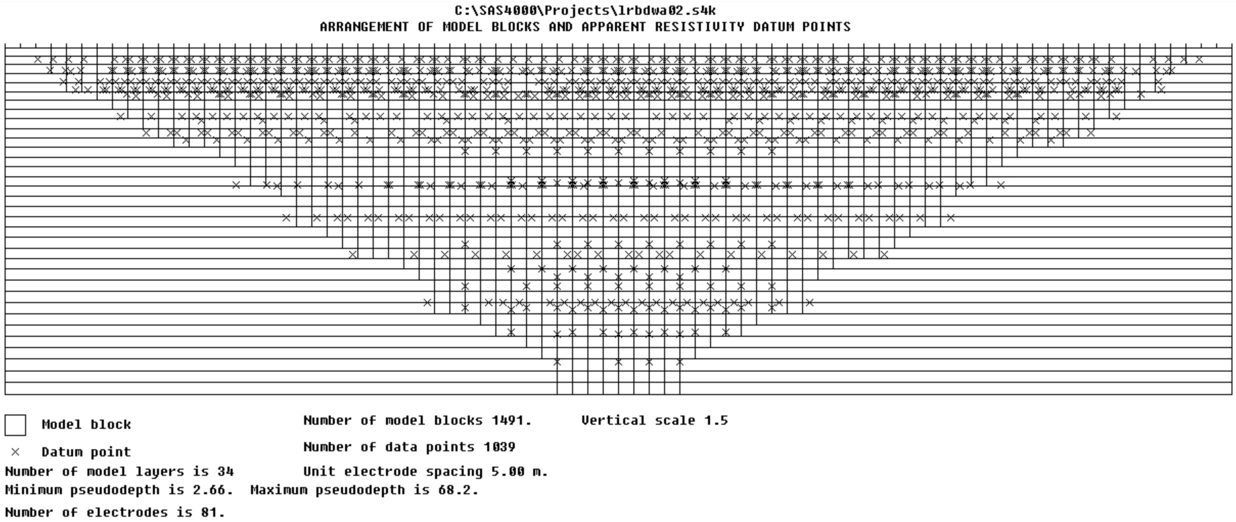

(a)

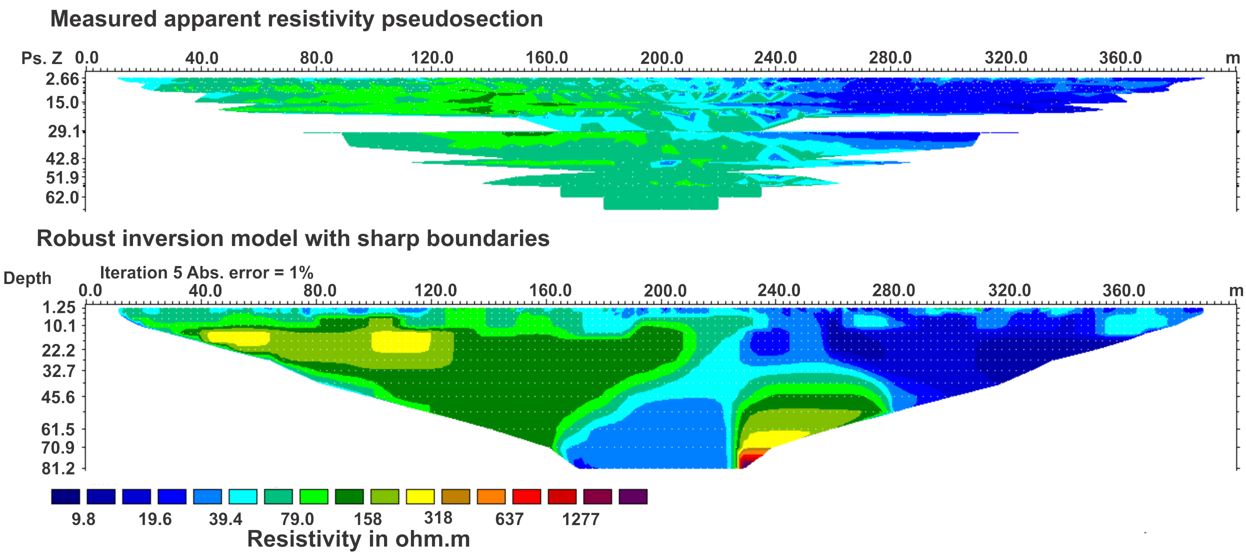

(b)

Figure 5.12 – Example of (a) arrangement of model block and and datum points in the pseudosection (b) measured apparent resistivity pseudosection and robust inversion model from one of the Bosumtwi survey lines

move closer to the shore of the lake especially at the western part and this gave large variations of resistivity near the ground surface. To get optimum results, the *Inversion/Model refinement* was used which allows the user to choose models with widths of half electrode spacing. This was necessary because failure to resolve the near surface variations could lead to distortions in the lower portion of the model as the program attempts to reduce the misfit. The downside of this *Inversion/Model refinement* is the increase in the inversion time. When the root mean square (RMS) error between the present and the previous iterations is $< 0.1\%$ the inversion stops. Figure 5.12 shows an example of a multi-electrode gradient data with the model blocks and the measured apparent resistivity pseudosection and the inverted model. This data was acquired using the GRAD4LX8 and GRAD4S8 protocols.

The *Display section/Model section with topography/User defined logarithmic resistivity interval* was selected in order to have a common contour interval. This was necessary because it gave the same colour code for a particular contour interval for all the profiles. The apparent resistivity pseudosections and model sections were saved in the *SURFER GRAPHICS* 2–D plotting program format. These were done after displaying the model with topography.

5.3.2 Analysis of the data using the Golden Software SURFER 10 GRAPHICS, GRAPHER 8, and Corel Draw GRAPHIC SUITE X5

Golden software SURFER 10 was used to redraw the model sections to enhance the font, labels and titles. The data with file names ***topreslog.dat*** were *grided* using the *Kriging method*. The number of lines in the x – and y – direction were multiplied by five. This was done to reduce the griding space and improve the smoothness of the contours as surfer uses these lines to generate the grid. The *contour map* was then generated from the the gridded data and the fill colour option was selected and the file ***topreslog.lvl*** was loaded to set the colour of the contour. The lines and labels in the contour were removed at this stage. Next the contour map was selected and a *base map* was added using the file ***topreslog.bln***. The base map was then selected and in the properties window, the line and fill colours were changed from the default black to white so that the overlay lines would not be shown. *Post map* was added afterwards with the file ***topreslog_post.dat***. The scales for the three maps were adjusted at this point in order to fit together. The labels, fonts, tick marks, tick labels, axis widths etc. were adjusted. The ERT models were then exported to *Corel Draw GRAPHIC SUITE X5* to further enhance the appearance.

The inferred fault lines and the sediment/bedrock contact on the various profiles were digitized using *Map/Digitized* option in the Surfer graphics and the data were saved with *bln* extension. The values were plotted as *Line/Scatter plots* using Golden Software *GRAPHER 8* 2–D plotting program. Regressional procedure was used to obtain the best fit.

5.3.3 Analysis of the Direction of the Inferred Fault Lines

Directional data is one of the most important geological information. This information was needed in order to characterize faults, joints and bedding planes. To describe these geologic features at the Bosumtwi crater area, it was necessary to compute the individual directional measurements and calculate the mean direction. Statistical methods are required for the determination of the mean direction and the test for significance. To calculate the mean directions with confidence limits, ***von Mises distribution*** and ***Fisher statistics*** were used because they are applicable to directional data that are dispersed symmetrically about the true direction. The statistical treatment by Fisher allows calculation of confidence intervals, comparison of mean directions and comparison of variance (Davis, 2002; Butler, 1992).

A simple mathematical background for calculating the parameters involved is given below. For a given angle θ, the x– and y– coordinates of the unit vector are given as:

$$\boxed{\begin{aligned} X_i &= cos\theta_i \\ Y_i &= sin\theta_i \end{aligned}} \tag{5.1}$$

The resultant R (Figure 5.13b) is calculated from the sum of cosines and sines of the individual vectors(Figure 5.13a):

$$\boxed{\begin{aligned} X_r &= \sum_{i=1}^{n} cos\theta_i \\ Y_r &= \sum_{i=1}^{n} sin\theta_i \end{aligned}} \tag{5.2}$$

The mean direction $\bar{\theta}$ which is the angular average of all the vectors is:

$$\bar{\theta} = tan^{-1}\left(\frac{Y_r}{X_r}\right) = tan^{-1}\left(\frac{\sum_{i=1}^{n} sin\theta_i}{\sum_{i=1}^{n} cos\theta_i}\right) \tag{5.3}$$

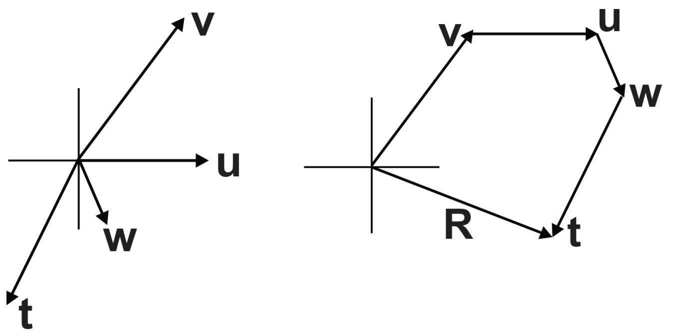

(a) (b)

Figure 5.13 – Sketch of (a) four vectors having different directions (b) the resultant R of the the four vectors

The next objective after the calculation of the mean direction was to determine the concentration parameter κ which is the statistic that can provide a measure of the dispersion of the population of directions from which the sample data set was drawn. To estimate the concentration parameter, it was necessary to calculate the mean resultant from the standardized coordinates of the resultant. The coordinates of the resultant R are divided by the number of observation n to standardize the resultant for comparison with samples of different sizes (Davis, 2002).

$$\boxed{\begin{aligned} \bar{C} &= \frac{X_r}{n} = \frac{1}{n}\sum_{i=1}^{n} cos\theta_i \\ \bar{S} &= \frac{X_r}{n} = \frac{1}{n}\sum_{i=1}^{n} sin\theta_i \end{aligned}} \tag{5.4}$$

The length of the resultant is given by the Pythagoras theorem:

$$R = \sqrt{X_r^2 + Y_r^2} = \sqrt{\left(\sum_{i=1}^{n} cos\theta_i\right)^2 + \left(\sum_{i=1}^{n} cos\theta_i\right)^2} \tag{5.5}$$

The resultant gives information about both the spread and the average direction of the vectors. The standardized resultant (mean resultant length) is:

$$\bar{R} = \frac{R}{n} = \sqrt{\bar{C}^2 + \bar{S}^2} \tag{5.6}$$

and it ranges from *zero* to *one*. If the values of $\bar{R}$ (Figure 5.14) are close to *one*, it means the observations are tightly grouped and values nearer to *zero* indicate random dispersion. The circular variance which measures the degree of dispersion can be calculated from the relation (Davis, 2002):

$$s_o^2 = 1 - \bar{R} = \frac{(n - R)}{n} \tag{5.7}$$

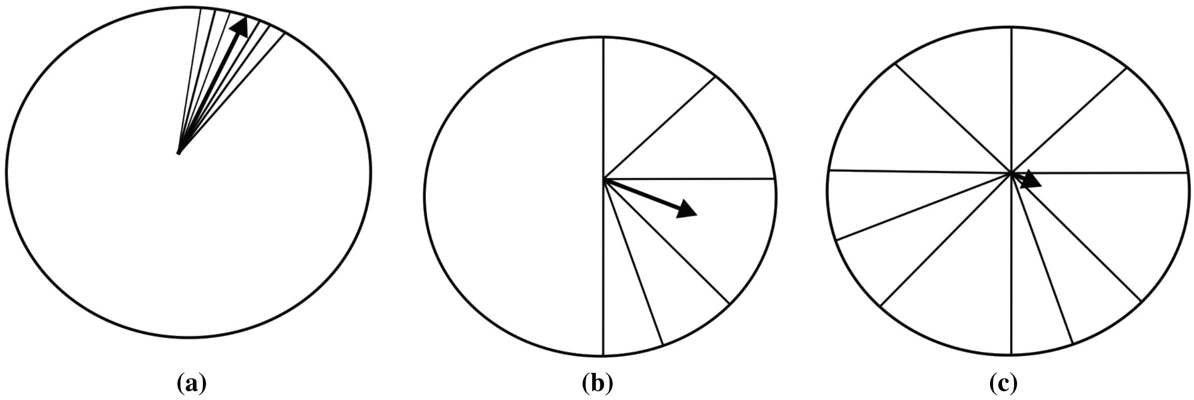

Figure 5.14 – Sketch of unit vectors indicating the value of $\bar{R}$ from different dispersions of vectors (a) $\bar{R} \approx 1$ (b) $\bar{R} \approx 0.5$ and (c) $\bar{R} \approx 0$

The ***von Mises distribution*** which is the circular equivalent of the normal distribution was also adopted to test how the inferred directions are circularly distributed.

$$\boxed{\begin{array}{l} H_0 : \kappa = 0 \\ H_1 : \kappa > 0 \end{array}} \tag{5.8}$$

This distribution has only two parameters, a mean direction $\bar{\theta}$, and a concentration parameter κ. A circular uniform distribution is realised if $\kappa = 0$. Statistical table for von Mises distribution was used to estimate the value of the concentration parameter from calculated values of $\bar{R}$. The null hypothesis H_0 and its alternative H_1 were used to test for the circularity or otherwise of the vectors. For the presence of a preferred direction, the Rayleigh's test for the critical values of $\bar{R}$ at 5% level of significance were estimated using statistical tables. Where the critical value is larger than the computed value, the hypothesis is that the geologic feature was uniformly circularly distributed and the null hypothesis could not be rejected. But, when the critical value was smaller, the null hypothesis was rejected and the conclusion was that the features were having a preferred direction.

The confidence limit for the calculated mean direction is analogous to the estimated standard error s_e of the mean. The standard error was calculated from the relation:

$$s_e = \frac{1}{\sqrt{n\bar{R}\kappa}} \tag{5.9}$$

and the interval of the error was:

$$\bar{\theta} \pm z_\alpha s_e \tag{5.10}$$

Confidence limit of α_{95} was used for the analysis and this means that one is 95% certain that the unknown true mean direction lies within α_{95} of the calculated mean. The probability that this statement is wrong is 5%.

The fault lines were grouped and a comparisons was made of their directions using the *F–distribution* at 2 and $2(N-2)$ degrees of freedom. The equality of their mean directions was tested by comparing the vector resultants of the two groups to vector resultant produced when the two sets of measurements are combined. For example, if n_1, and R_1 are the number of observations and the resultant vector for set 1 respectively, and n_2, and R_2 are the number of observations and the resultant vector for set 2 respectively. Then the statistic

$$F_{1,n-2} = \frac{(n-2)(R_1 + R_2 - R_p)}{(n - R_1 - R_2)} \tag{5.11}$$

where $n = n_1 + n_2$ is the total number of observation and R_p is the resultant when all the individual observations are combined. Equation (5.11) is applicable when κ has a large value (greater than 10), and if it is smaller than 10 but greater than 2 equation (5.12) was applied (Davis, 2002; Butler, 1992).

$$F_{1,n-2} = \left(1 + \frac{3}{8\kappa}\right)\left(\frac{(n-2)(R_1 + R_2 - R_p)}{(n - R_1 - R_2)}\right) \tag{5.12}$$

If the mean directions of the two groups are significantly different, then R_p will be shorter than $R_1 + R_2$. But when the resultant of the combined samples is approximately equal to the sum of their two resultants, then the two samples were from the same population.

Rose diagrams and polar plots were generated using Golden Software *GRAPHER 8* 2–D plotting program from the ***F-statistics*** calculations for the inferred fault lines around the crater. The rose plots were grouped to fault lines in the east and west. The azimuth, β, was calculated from Equations (5.13) and (5.14) (Poelchau and Kenkmann, 2008).

$$x = tan^{-1}\left(\frac{lat_c - lat_d}{(long_c - long_d)(coslat_c)}\right) \tag{5.13}$$

$$\beta = \begin{cases} x + 90, & lat_c - lat_d < 0; x < 0. \\ x + 270, & lat_c - lat_d < 0; x > 0. \\ x + 270, & lat_c - lat_d > 0; x < 0. \\ x + 90, & lat_c - lat_d > 0; x > 0. \end{cases} \tag{5.14}$$

Where lat_c and $long_c$ are coordinates of the centre of the lake which was taken as (06° 30′ 15.04″ N, 01° 25′ 36.17″ W) and lat_d and $long_d$ are latitude and logitude of the data points. The north and south were assigned values of 0° and 180° respectively moving in the clockwise direction.

CHAPTER 6

RESULTS AND INTERPRETATION

6.1 Introduction

On electrical resistivity tomographies, fault zones can be easily delineated because they have lower resistivities than their surroundings as a result of their high permeability and high density of discontinuities. Faults are sometimes characterized by their sharp resistivities contrast with their hosts. When the faults are filled with calcite or quartz they can have higher resistivity than their sorroundings. Generally, faults occuring in crystalline environment are less resistive than the sorrounding rock (Giocoli et al., 2008; Colella et al., 2004; Diaferia et al., 2006; Scheibz et al., 2009; Suzuki et al., 2000; Barsukov, 1970). The analysis of the resistivity images is based on the knowledge of geology of the crater area and the topography on the profile. There are a lot of thrust faults of multiple orientations at the Bosumtwi impact crater site (Reimold et al., 1998). The main lithological units of the crater area are the target rocks (graywackes and phyllites/slates), the sediments and the impact breccias (allochthonous, dikes and parautochthonous) (Deutsch et al., 2007). Figure 6.1 shows the resistivity of meta greywackes, slate/phyllites and breccias; the breccias have the lowest resistivity and the meta greywackes the highest and the phyllites/slates have intermediate values. Open and close fractures have been detected at the area with most of the fractures occuring in the meta graywackes and due to the high degree of fracturing some of the rocks disintegrates when cutting (Deutsch et al., 2007; Hunze and Wonik, 2007).

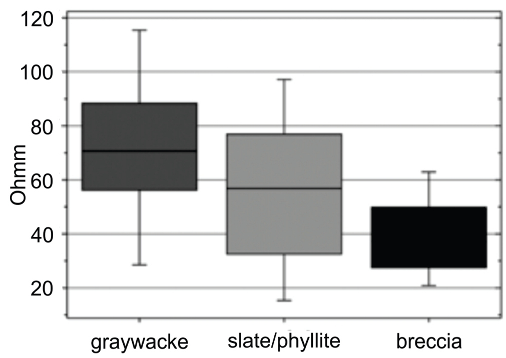

Figure 6.1 – Whisker diagram of the resistivities of three types of rocks at Bosumtwi crater site (Hunze and Wonik, 2007)

The resistivity profile lines (Figure 5.6) have been named after the communities where they were acquired with the exception of Mmem and Konkoma which were named after the traditional owners of the land. These two transects were not in a community. The Mmem profile is on the north eastern section of the lake and is about midway between Nkowie and Pipie No. 2 and Konkoma is on the eastern side and is also about midway between Brodekwano and Dwamam. Detailed topography was done using Garmin GPSMAP 62s Handheld GPS on all the profiles. All the imaging surveys have been topographically corrected. For uniformity in the interpretation of the different true resistivity sections along various profiles, a common colour code was adopted for presentation of the results.

The tomographies generally show a low surface resistivity towards the lake as expected, moderately high resistivity as you move uphill towards the crater rim and high resistivity at the base towards the end of the profile. The very low resistivity (< 64 Ω.m) from the shore uphill towards the rim of the crater represents the post-impact lake sediments. The solid white lines are the inffered fault lines and the dotted white ones are the sediments and bedrock boundary. The blocks marked **P** and **A** are the interpreted parautochthonous and allochthonous breccias respectively and the low resistivity zones labelled **F** are fractures.

6.2 Analysis of the Profiles

6.2.1 Brodekwano Profile

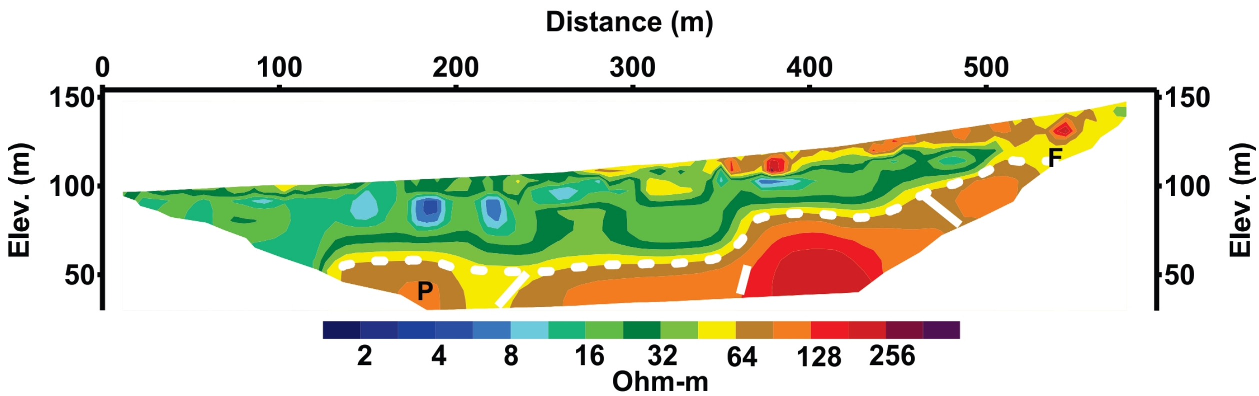

Figure 6.2 – 2D resistivity imaging traverse conducted at Brodekwano located on the east end of the lake

The sediments stretch from the shore to the end of the profile. The moderately high resistivity region (> 90 Ω.m) at the base of Figure 6.2 and the zone marked **P** are likely to represent parautochthonous breccia (brecciated monomict) because of their geometry. It is likely they were part of the target surface marked with the dotted white line and faulted at 200 m and 350 m. The portion labelled **F** is probably an open fracture filled with clasts. The faults identified at 200 m and 450 m have different dip orientations.

6.2.2 Nkawie Profile

The sediment on this profile extend to just about 150 m (Figure 6.3) and this is a direct correspondence with the geology. The lack of sediments on this line explains why this is the only profile with no farming activity beyond 200 m from the shore. When the local people were asked why there is no farming activity on the part of the area they said nothing can be grown there apparently referring to the fact that neither cocoa nor food crops grow well there. The low resistivity block labelled **F** at 300 m mark could be an open fracture probably filled by matrix of polymict breccia and the one at 600 m filled with clasts. The other fault lines are marked with solid white lines. The regions marked **P** were interpreted as parautochthonous: they appear to be part of

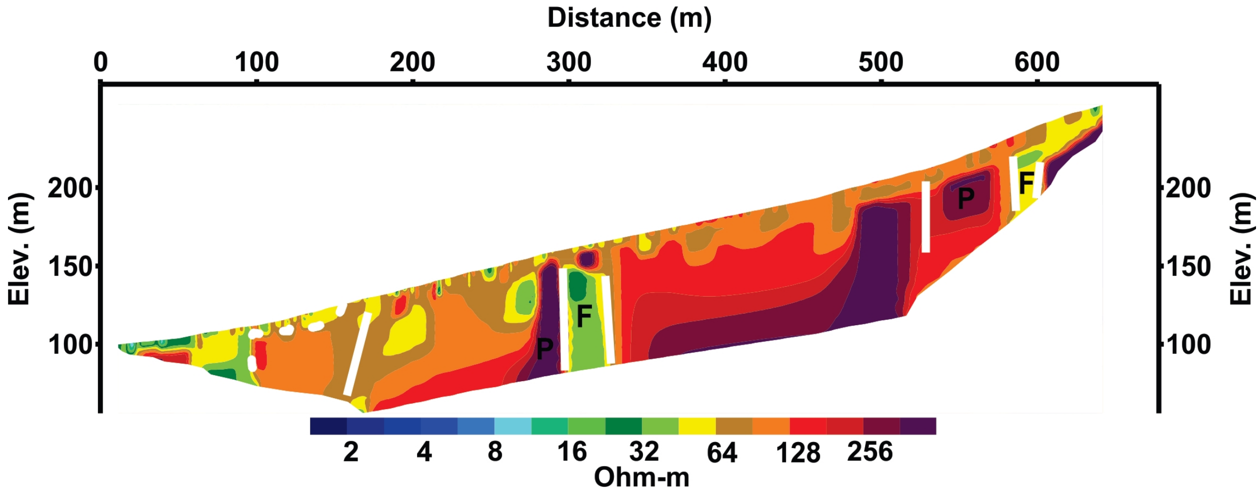

Figure 6.3 – 2D resistivity imaging traverse conducted at Nkawie on the north east

the high resistivity block that spans from about 150 m to the end of the line but fractured at 300 m and 600 m. It seems that the fracture at 600 m extends to the base of the parautochthonous breccia at 550 m.

6.2.3 Konkoma Profile

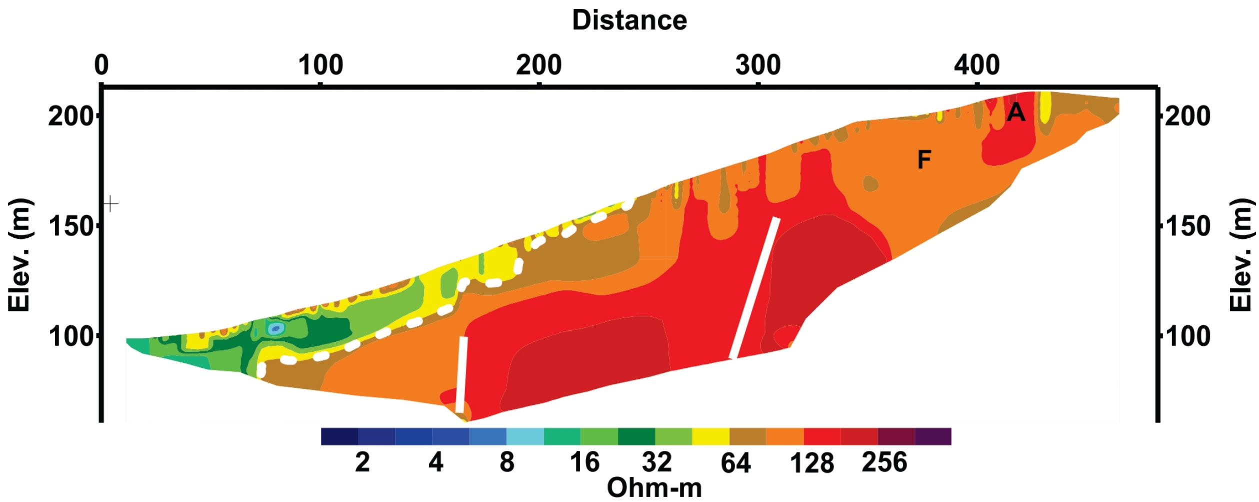

Figure 6.4 – 2D resistivity imaging traverse conducted at Konkoma about mid–way between Brodekwano and Dwamam on the eastern side of the lake

The sediments thin out sharply after about 180 m (Figure 6.4). The area tagged **A** is reasonably an allochthonous breccia because of its smaller extent and it does not seem to have a root. The high resistivity region (> 128 Ω.m) at the base is interpreted as brecciated monomict and is faulted around 300 m.

6.2.4 Mmem Profile

The region of the lake sediments extend from the shore to 680 m towards the rim (Figure 6.5). The segments designated as **P** are likely to be parautochthonous because of their geometry and dimensions (the first block spanning about 250 m). These blocks are possibly part of the target surface that has been brecciated and faulted at around 500 m.

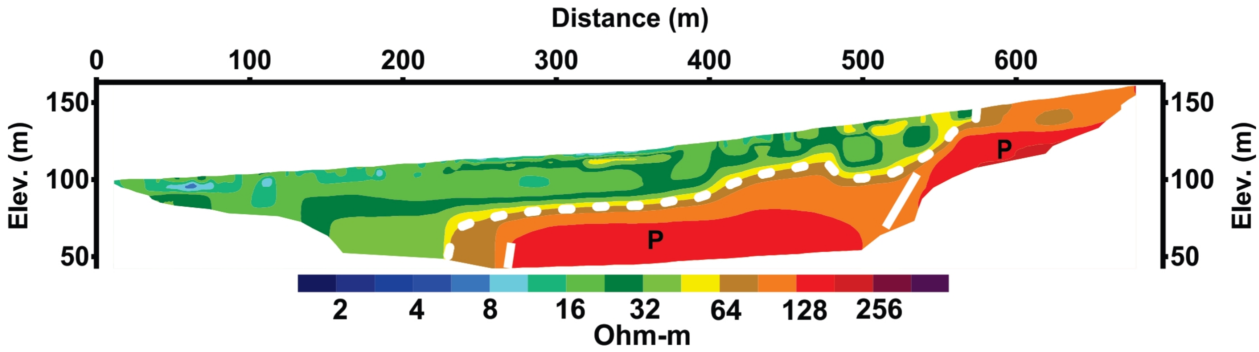

Figure 6.5 – 2D resistivity imaging traverse conducted at Mmem about mid–way between Nkawie and Pipie on the north east

6.2.5 Dwamam Profile

The Dwamam profile (Figure 6.6) exhibits peculiar characteristics; the topography rises sharply from the shore of the lake to about 180 m and descends to about 20 m and then it almost flattens. From the field observation there were no lake sediments from 5 m mark to about 200 m from the shore. The ERT very clearly shows the location of the lake sediments from 200 m to about 500 m mark being in very good agreement with the field observations. This region between 200 - 500 m (black rectangle) which lies between two moderately high resistivity regions (> 64 - 200 Ω.m) could represent a downthrown region which was later filled by sediments. The zones dubbed **P** at the shore were interpreted as in-situ blocks (parautochthonous) that have been faulted and those at 600 m and 900 m as brecciated monomict because of their geometry. The open fractures **F** are possibly filled with clasts.

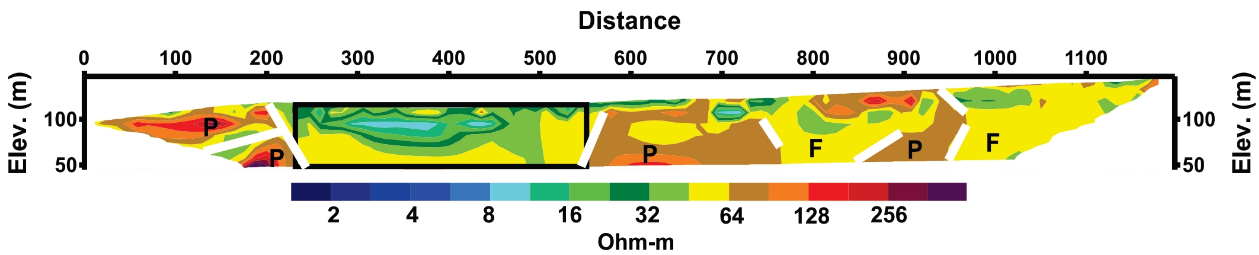

Figure 6.6 – 2D resistivity imaging traverse conducted at Dwamam situated on the eastern side of the lake

6.2.6 Ankaase Profile

This 800 m long profile (Figure 6.7) has sediments covering up to 350 m. The subsurface is highly fractured. The open fractures **F** on this profile are possibly filled with polymict matrix of heterogeneous nature due to their very low resistivities. All the high resistive zones were interpreted as parautochthonous because they appear to be part of the fractured target surface. The sediment and bedrock boundary at 250 m was interpreted as a fault line as it is too deep to correspond to the erosional surface.

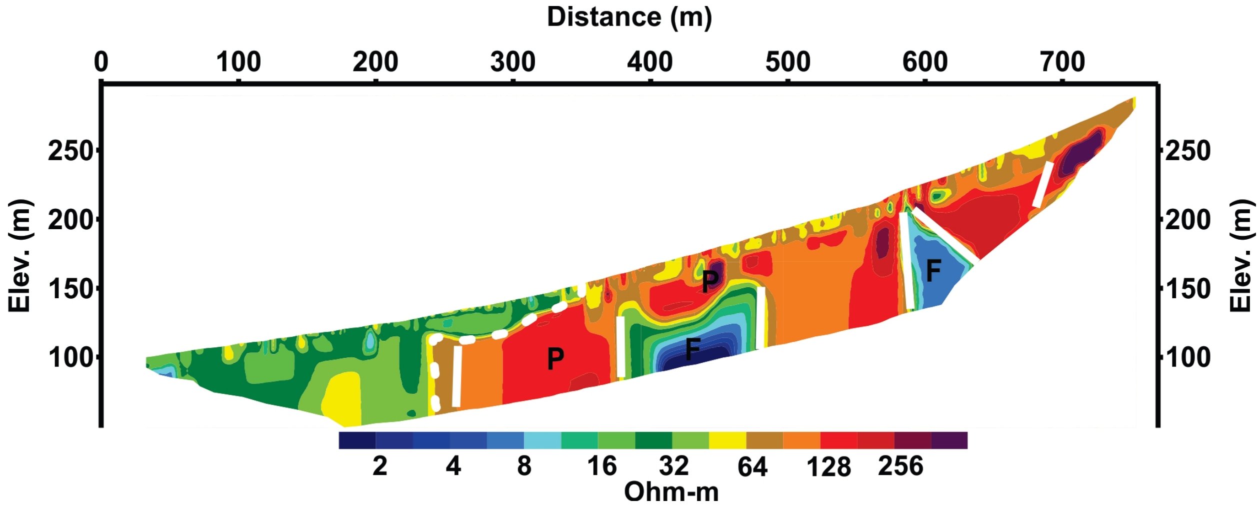

Figure 6.7 – 2D resistivity imaging traverse conducted at Ankaase located on the south eastern portion of the lake

6.2.7 Duase Profiles

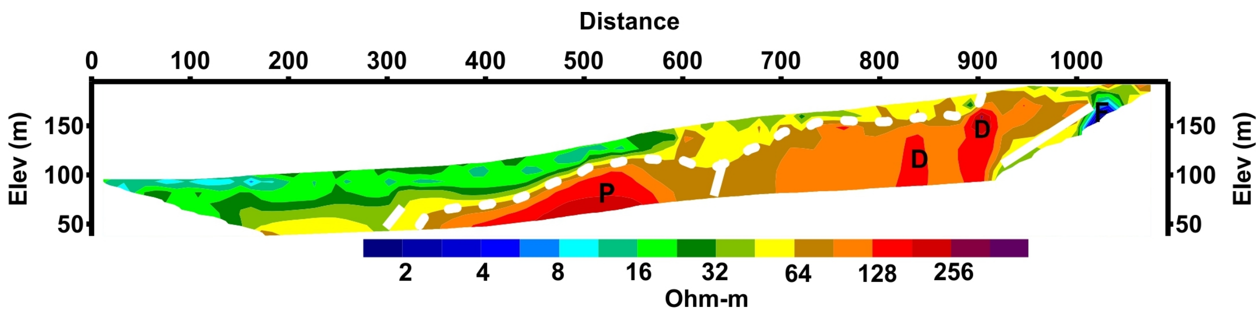

Figure 6.8 – 2D resistivity imaging traverse conducted at Duase profile 1 located on the southern part of the lake

Two ERTs were carried out in this community which is situated at the southern section of the lake (Figures 6.9 and 6.8). The moderately high resistivity regions marked **D** could be dikes due to their structure and their resistivity. They could also have resulted from an insitu fractured megablock and as such a parautochthonous breccia. If they are dikes, then they contravene the findings of Hunze and Wonik (2007) that dike breccias have dimensions between one decimeter

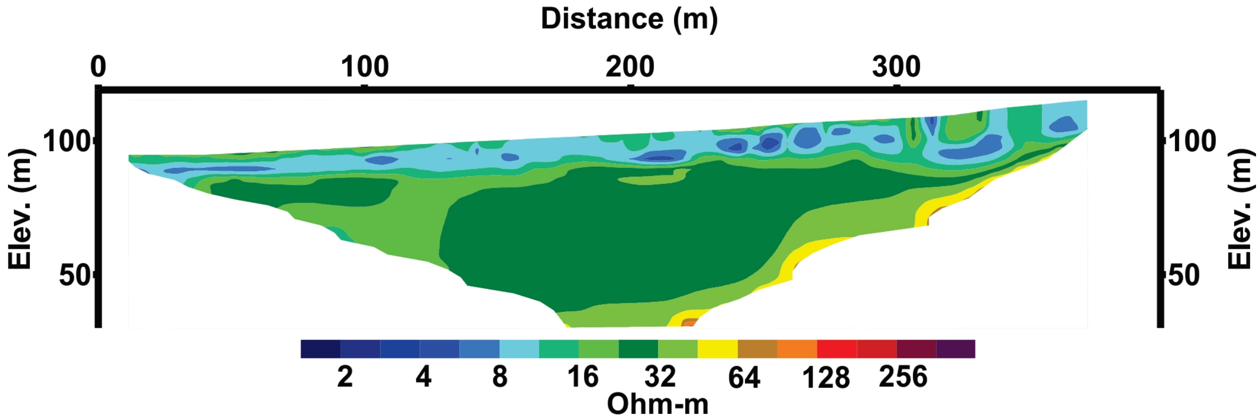

Figure 6.9 – 2D resistivity imaging traverse conducted at Duase profile 2 located on the southern part of the lake

and one meter. The fractured zone **F** is probably filled with heterogeneous polymict matrix and **A** is a brecciated monomict considering its geometry and dimension. The sediments stretch about 900 m on this profile. The second profile at Duase (Figure 6.9) exhibits only the lake sediments.

6.2.8 Dompa Profile

Figure 6.10 shows the Dompa traverse which has almost 400 m of post impact sediments. The blocks designated as **P** were analysed as in-situ brecciated monomict by virtue of their geometry especially for the ones at 300 and 400 m and for the one between 500 and 600 m because of its size. The fracture **F** at 350 m is likely saturated with polymict matrix. The fault line at 420 m dips away from the centre of the crater.

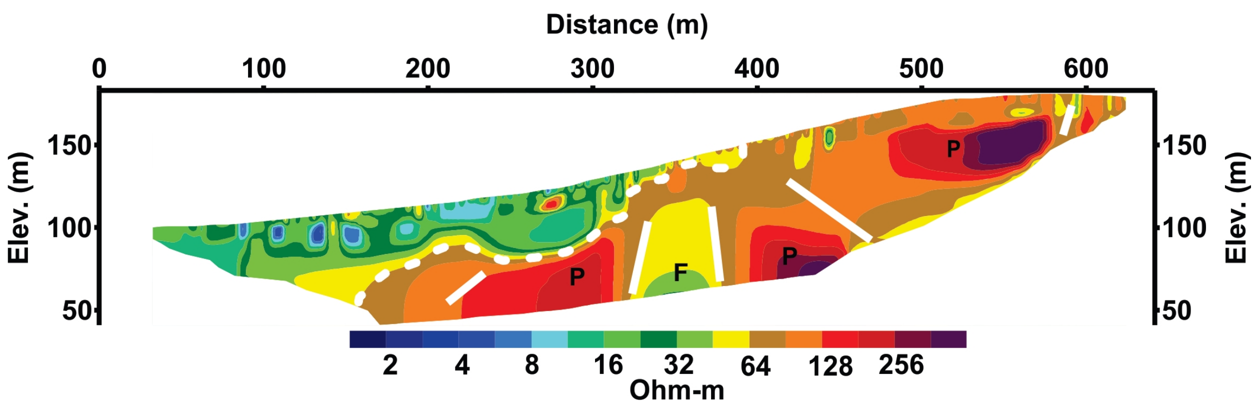

Figure 6.10 – 2D resistivity imaging traverse conducted at Dompa found on the southern section of the lake

6.2.9 Banso Profile

The very low resistivity region (black rectangle) (Figure 6.11) from the 210 to 380 m point was water logged and basically the whole profile was within the lake sediment. The high resisitivities observed on the surface could be as a result of talus. This profile is short because of the uncooperative attitude of the people in the community.

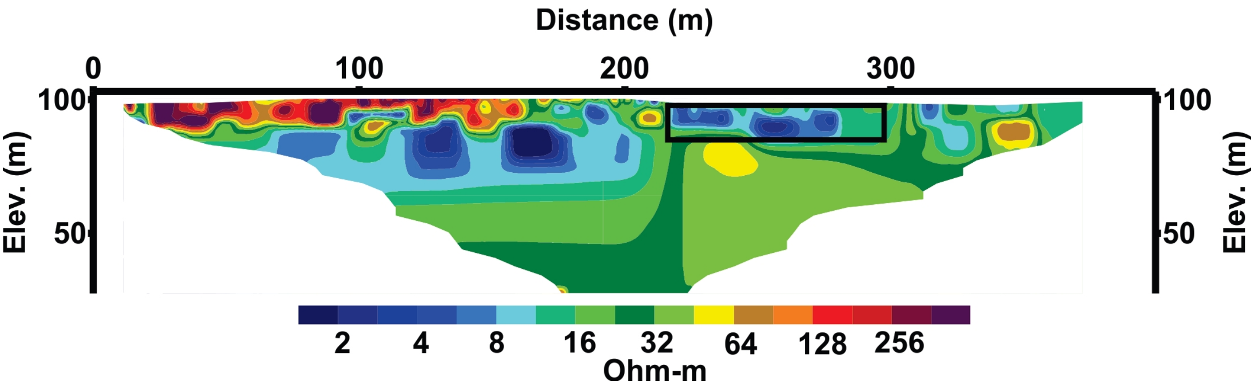

Figure 6.11 – 2D resistivity imaging traverse conducted at Banso found on the southern section of the lake

6.2.10 Apewu Profile

There is about 250 m of sediments on this traverse (Figure 6.12). The zone tagged **A** is unlikely to be parautochthonous breccia due to its rootless nature and dimension and is interpreted as brecciated polymict. The fractures **F** are probably saturated with heterogeneous polymict matrix. The sediment and bedrock interface is interpreted as a fault line due to its steepness nature and a moderately high resistivity poping out nearby. The patches of high resistivities on the surface from the shore to about 200 m could come from talus. There was also a problem of cooperation from this community, so we could not do much work there.

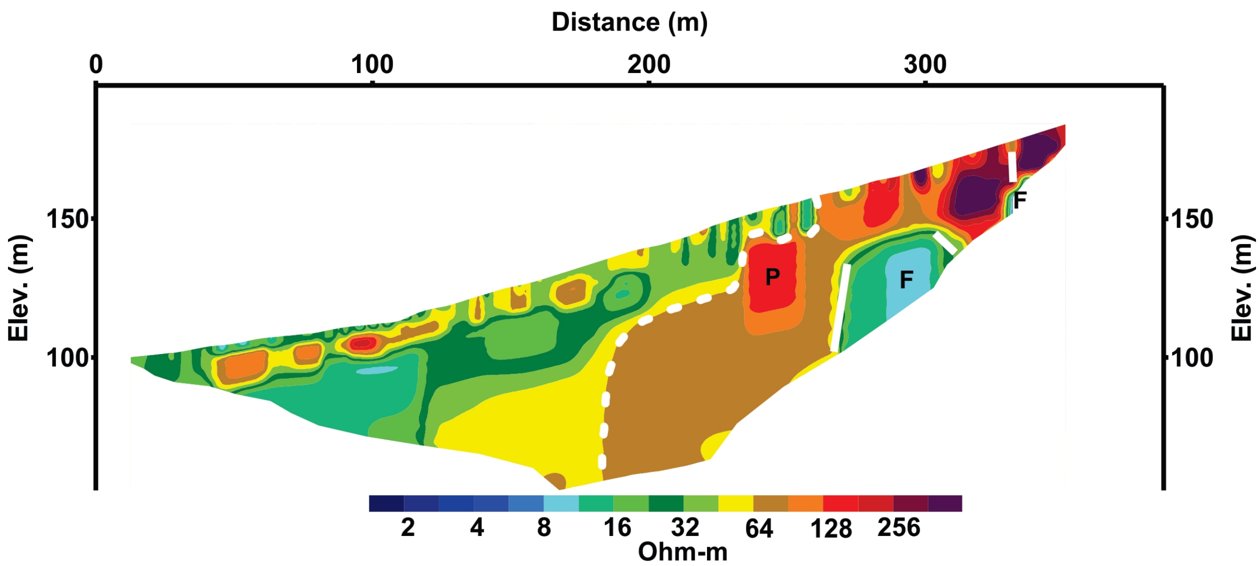

Figure 6.12 – 2D resistivity imaging traverse conducted at Apewu found on the southern section of the lake

6.2.11 Detieso Profile

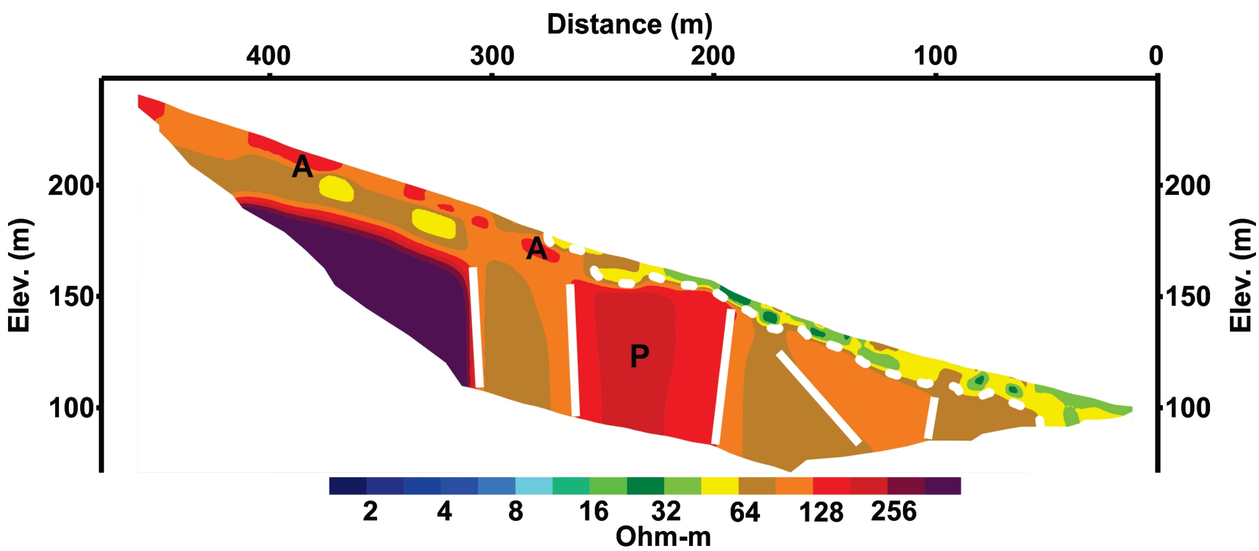

Figure 6.13 – 2D resistivity imaging traverse conducted at Deteiso located on the south western side of the lake

The Deteiso traverse (Figure 6.13) is the steepest of all the profiles.The sediments stretch over 300 m. The zone labelled **A** is explained as allochthonous considering its dimensions and is unlikely to be part of the metasedimentary target surface directly below because there is no slightest of root connecting them. The block tagged **P** between 200 and 300 m was interpreted as parautochthonous due to its dimensions and geometry. The dip of the inferred fault lines here are very steep.

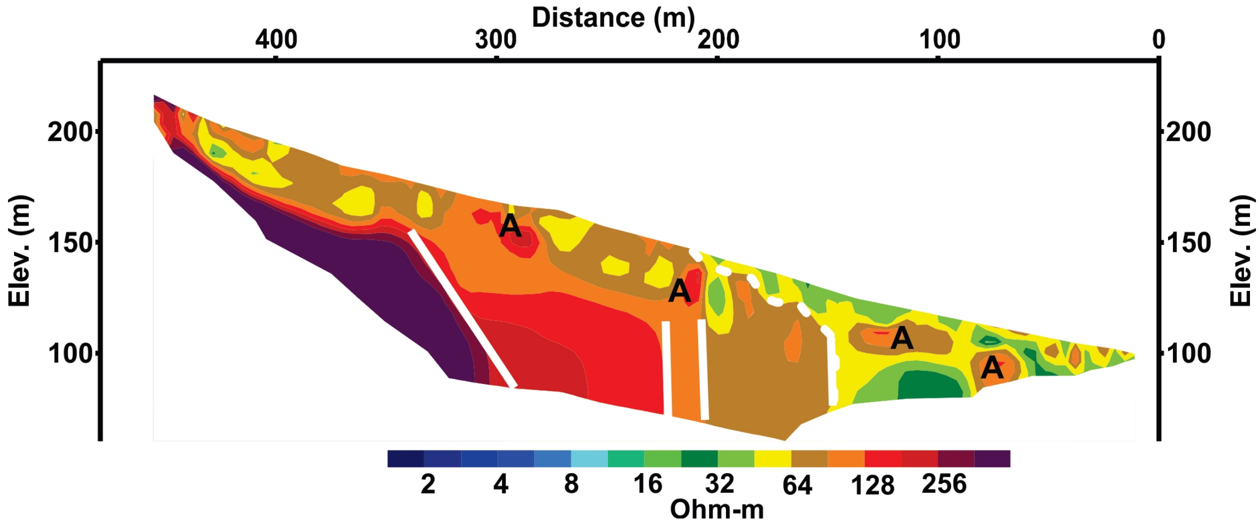

Figure 6.14 – 2D resistivity imaging traverse conducted at Esaase located on the western side of the lake

6.2.12 Esaase Profile

The moderately low resistivity region 64 - 100 Ω.m observed on the surface of the profile (Figure 6.14) could come from the considerable amount of talus found in the area. The zones marked **A** could be interpreted as allochthonous brecia or talus eroded from upper crater walls and brought there by mass wasting. The feature at the base of the profile with resistivity > 128 Ω.m is likely to represent the metasedimentary target rock, because of its lateral extent (hundreds of metres), high resistivity and geometry. The faults on this traverse dips very sharply. The extent of the sediments is about 200 m.

6.2.13 Abaase Profile

There are more talus in Abaase than any other area around the lake and that is what is reflecting as high resistivity on the surface (Figure 6.15). This combination of talus and sediments extends to about 300 m. The area marked **A** are possibly allochthonous breccia due to its size. The high resistivity zone (> 128 Ω.m) at the base of the profile could be the metasedimentary target surface in view of the resistivity, geometry and dimensions.

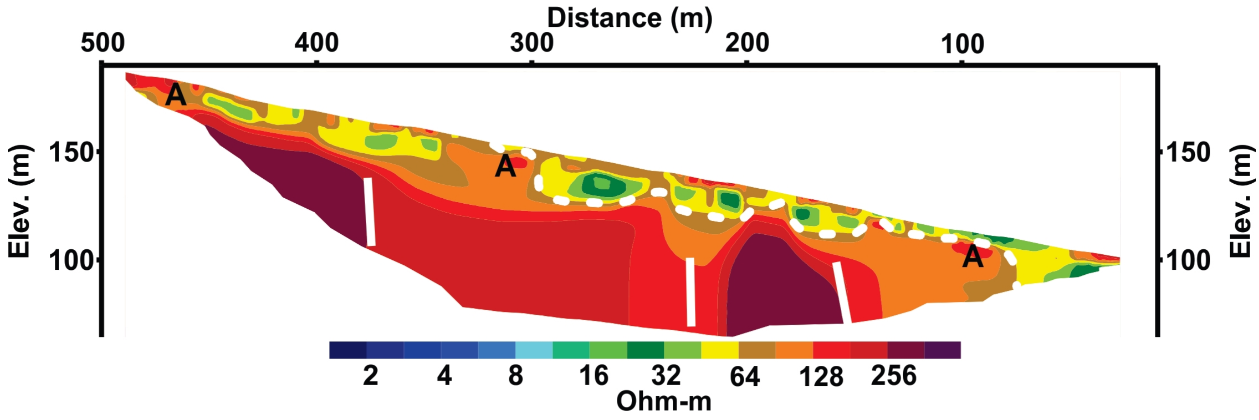

Figure 6.15 – 2D resistivity imaging traverse conducted at Abaase located on the western side of the lake

6.2.14 Obo Profile

The high resistivity region (> 128 Ω.m) at the base of the tomograph (Figure 6.16) is likely to represent the metasedimentary target rock, because of its geometry and lateral extent (hundreds of metres) and high resistivity. The zone marked **P** is likely to represent a brecciated monomict. This profile shows high resistivities on the surface which could be talus eroded from upper crater walls and brought there by mass wasting.

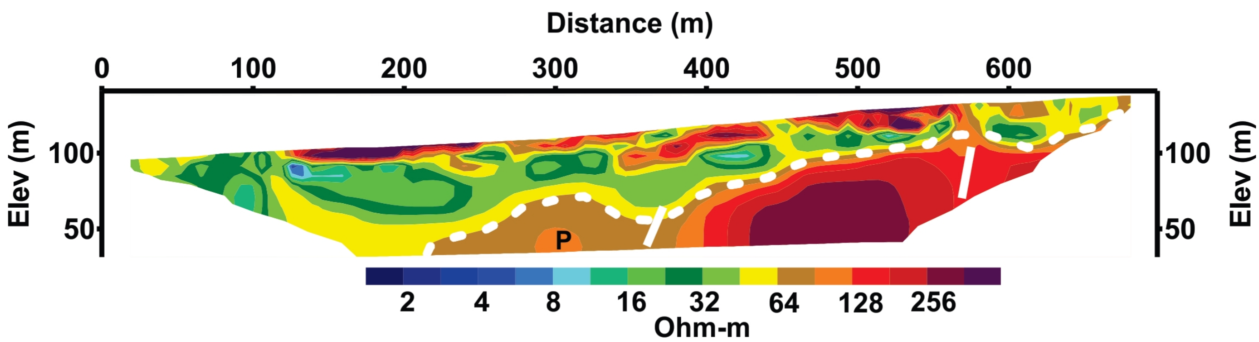

Figure 6.16 – 2D resistivity imaging traverse conducted at Obo situated on northern section of the crater

6.2.15 Adwafo Profile

The moderately low resistivity region 64 - 100 Ω.m observed on the surface of the profile (Figure 6.17) could come from the considerable amount of talus found in the area. The region **P** is possibly a brecciated monomict and part of the target rock. The high resistivity region (> 128 Ω.m) observed at the base from 380 to 620 m is likely to represent the metasedimentary target rock, because of its high resistivity and geometry, and it is possible that this target rock has been faulted at point 500 m resulting in a downthrow. The patches of high resistivity regions near the surface indicated as **A**

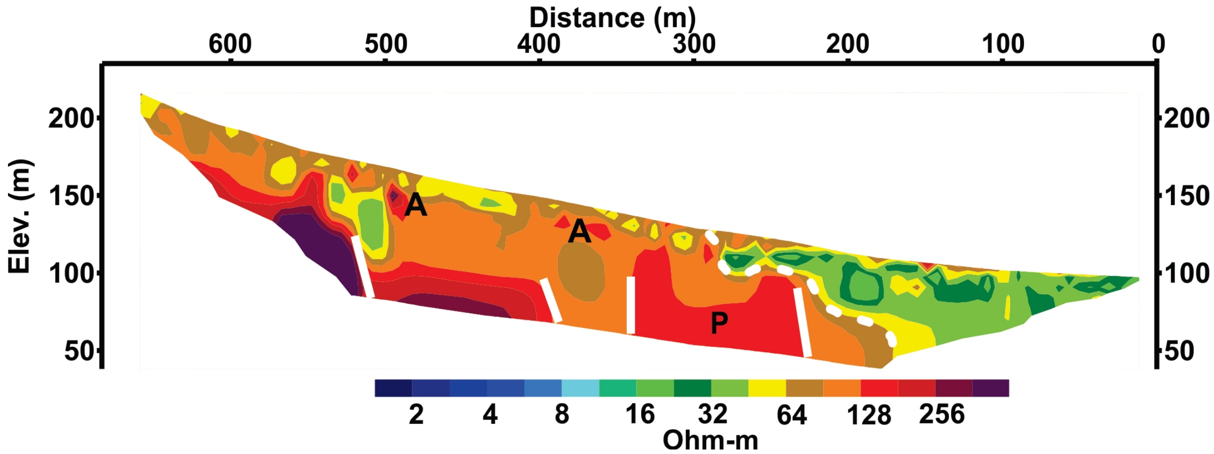

Figure 6.17 – 2D resistivity imaging traverse conducted at Adwafo situated on the north western portion of the lake

could either be talus eroded from upper crater walls and brought there by mass wasting as a result of the steepness of the slope or allochthonous breccia.

CHAPTER 7

DISCUSSIONS

7.1 Interpretation of Discontinuous Features

Using the ERT it has been possible to clearly map the extent of the post impact lake sediments and the crater wall on each profile and delineate the other discontinuities; the dikes, allochthonous and parautochthonous breccias, the fractures and the faults as shown in Figure 7.1. This section looks at how these discontinuities are related by juxtapositioning them as they appear within the crater.

7.1.1 The Post-Impact Lake Sediments and the Talus

For all the lines the results show a low resistivity (< 64 Ω.m) from the shore of the lake towards the rim. These well defined zones were interpreted as the lake sediments. These zones thin out when you move uphill. The extent of the sediments around the lake is assymetrical (Figure 7.1) with the eastern and southern portions of the lake having the largest and deepest extent and the western the shortest and thinnest. Figure 7.2a shows the dips and expanse of the sediments. To have a better view of the limit of the sediments around the lake, the X–Y plot was converted to a polar plot using Equations (5.13) and (5.14). This angular plot displays the juxtaposition of the profiles and also as they appear from azimuthal view (Figure 7.2b). The 8.5 km lake is assumed to be a point located at the centre of the polar plot, so the stretch is from the limit of the water uphill. The interior slope is steepest near the rim and decreases smoothly towards the lake in the eastern and some portions of the southern sections but sharply in the western part. The sediments/bedrock surface dips between the lowest of 16^{o} in the NE to the highest 36^{o} in the SW as shown in Table 7.1.

Considerable amount of talus was observed around the lake. The amount increases as you move downhill towards the lake and it is abundant on the western portion of the crater with Abaase having the highest quantity of talus material. Even though a small quantity of talus was observed in the Obo area, the profile there shows very high near surface resistivities.

Table 7.1 – The slope of the sediments and bedrock boundary around the crater

Section of crater	Angle of dip of sediments and bedrock contact (^{o})
Northeast	16
East	17
Southeast	20
South	25
Southwest	36
West	27
Northwest	19
North	19

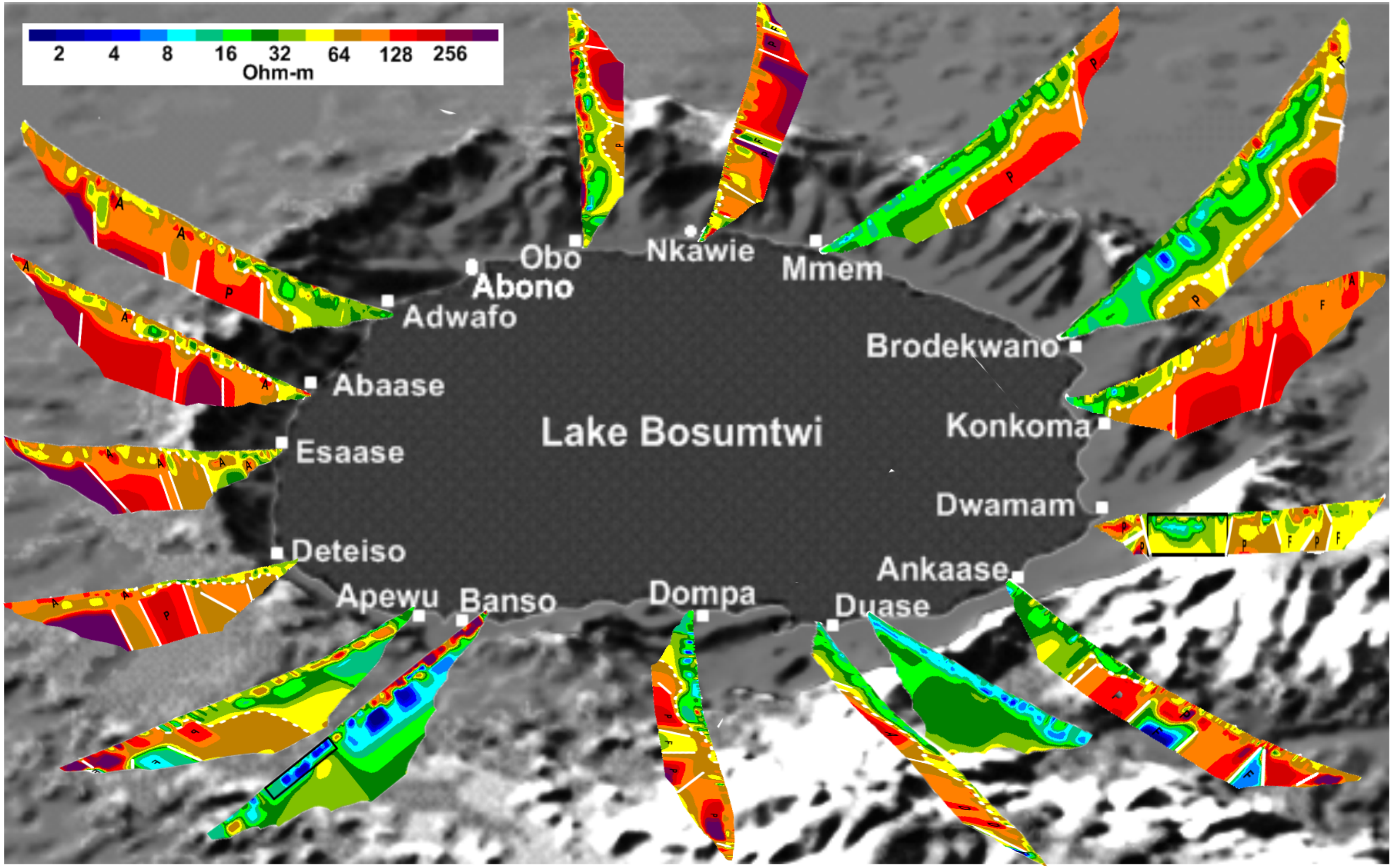

Figure 7.1 – Bosumtwi impact crater with the 2D resistivity images

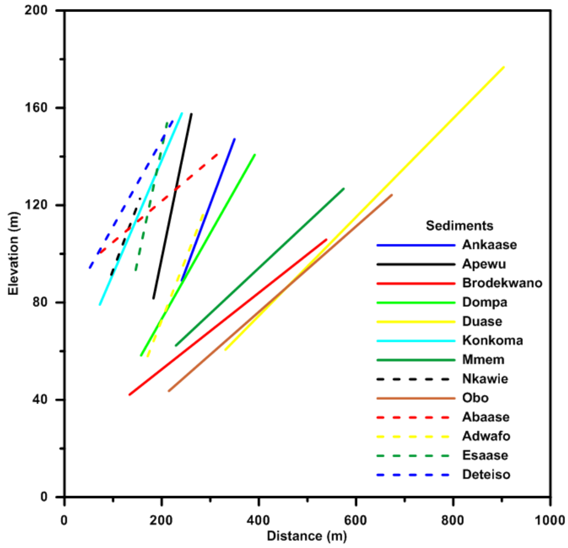

(a)

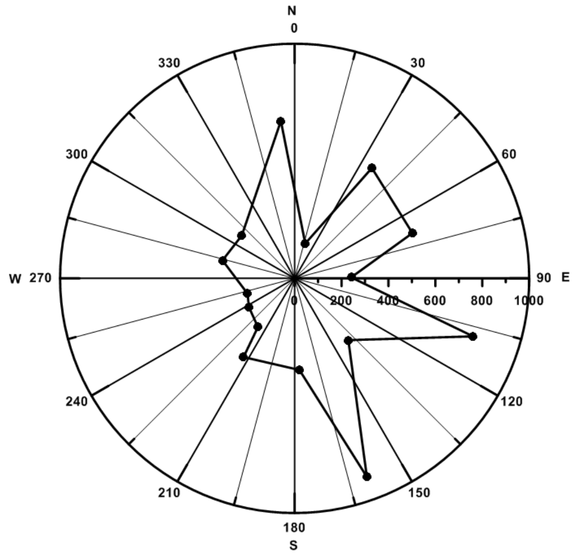

(b)

Figure 7.2 – The extent of sediments from the lake located at 0 m; (a) The dipping of the sediments towards the lake and (b) Radial plot of azimuth (location within the crater) relative to the centre of the lake

7.1.2 The Bedrock

The areas with resistivity > 64 Ω.m were labelled as the bedrock which consists of metagraywackes, phyllites and slates. With the exception of Dwamam, Banso and Duase 2 profiles, all the others evidently shows the sediments and target surface boundary, and the dipping of the bedrock is the same as that of the sediments (Table 7.1, Figures 7.1, 7.2a and 7.2b). The target appears to have been severely faulted and downthrown between 200 and 500 m on the Dwamam resistivity image. The Banso and Duase 2 tomograms are within the post impact sediments. The target ground has been brecciated and faulted all around the crater, but the degree of fracturing is less on the western part of the crater.

The unbrecciated part of the subsurface (> 256 Ω.m) were noticeably marked on the western section of the crater. This could mean the bolide that impacted obliquely (Artemieva et al., 2004) came from the northeast or east and that the shockwave front is below the depth of resolution of the 2D resistivity images which is about 75 m. This very high resistivity feature is obvious from the north to the southwest. The Nkawie, Obo, Adwafo and Abaase profiles have peculiar appearance: at around 300 m from the shore, there is a high resistivity feature, but on Abaase it is at 200 m. There is also a high resistivity zone between 400 and 500 m at Nkawie, Obo and Adwafo, but it is below 100 m on the Adwafo and Obo profiles, and did not appear at all on the Abaase image. Could it be that that portion is faulted and downthrown as in the case of Adwafo and as such below the resolution of the resistivity equipment? Furthermore, another high resistivity belt is evident on the images getting to the end of the profile and this is probably the same very high resistivity region beyond the 300 m on the Esaase and Deteiso traverses. This is not so clear on the Obo traverse but could be seen to be poping up below the 600 m.

Bilateral symmetry discovery is very essential in restricting the direction of an oblique impact.

The gradient of the bedrock surface shows a bilaterally symmetric pattern with the symmetry axis running NE–SW as shown in Table 7.1. The north which is symmetrical to the east has comparable dip values 19^{o} and 17^{o} respectively, the NW and the SE have 19^{o} and 20^{o} and finally the west and south have 27^{o} and 25^{o} respectively. This is in agreement with Artemieva et al. (2004) who proposed an impactor coming from the N–NE.

7.1.3 The Dikes, Allochthonous and Parautochthonous Impact Breccias

All but the Banso tomogram show relatively high resistivity values which were described as either allochthonous or parautochthonous impact breccias (Figure 7.1) depending on their geometry and/or lateral extent. The possible dikes were identified purely by their geometry on the Duase profile 1.

7.1.4 The Faults and Fractures

With the exception of the Banso and Duase 2 traverses which were within the sediments, faults were identified on all the profiles (Figure 7.1). Generally, the faults on the western side of the crater dip steeply (nearly vertical) than those on the east (Figures 7.3a and 7.3b). In order to relate the profiles very well in a juxtaposition manner, the data is also displayed in the X–Y plot with X–axis being the azimuth and the Y–axis being the radial distance from the shore of the lake. Reverse faults (faults dipping away from the centre of the crater) were mapped in the northeast, southeast and southwest. Reflecting the results displayed in Figures 7.3a and 7.4, there is a fault line at around 240 m on the Adwafo, Abaase and Esaase profiles. This could be the same fault line forming a ‘concentric‘ fault on the west and northwest part of the crater. There are other similarities as well: 200 and 300 m on Esaase and Deteiso and 270 m on Deteiso and Apewu traverses. These faults could all be related. There is no noticeable link between the faults on the eastern section of the crater.

Fracture zones (areas with resistivities $< 64\ \Omega.m$ far from the shore and not on the surface of the tomograms) were mapped on all the traverses on the southeastern portion of the crater (Figure 7.1). They were interpreted as open fractures filled with polymict breccias in a heterogenous matrix. The dips of the faults and/or fractures average about 51^{o} and 80^{o} for the east and west sections of the crater respectively and this is consistent with the findings of Reimold et al. (1998) and Hunze and Wonik (2007). Hunze and Wonik (2007) on their analysis of the televiewer images from the central uplift borehole LB–08A, found that most of the fractures were towards the SE. Could this have a relation with the numerous fractures found on the SW profiles (especially Dwamam and Ankaase)? Or are the fractures due to the intruding metavolcanics? The topography outside the Bosumtwi crater rim is nearly horizontal (Koeberl and Reimold, 2005), so the increase in dip angles towards the southwest part is as a result of it being in the downrange direction of the oblique impactor.

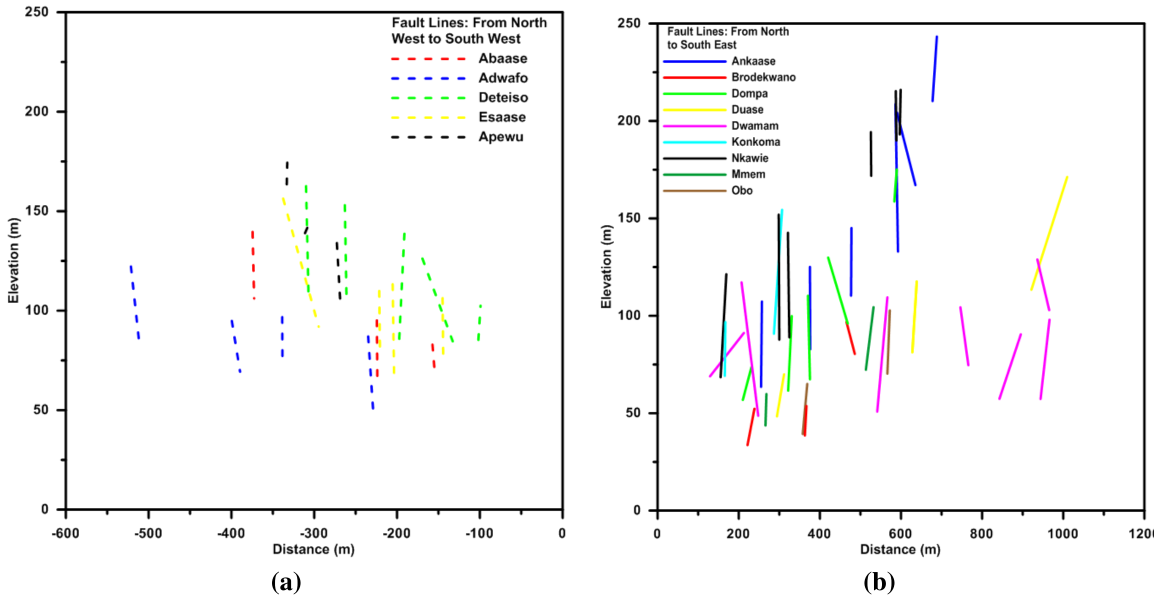

Figure 7.3 – Dips of the inferred faults around the lake: (a) Western section and (b) Eastern section

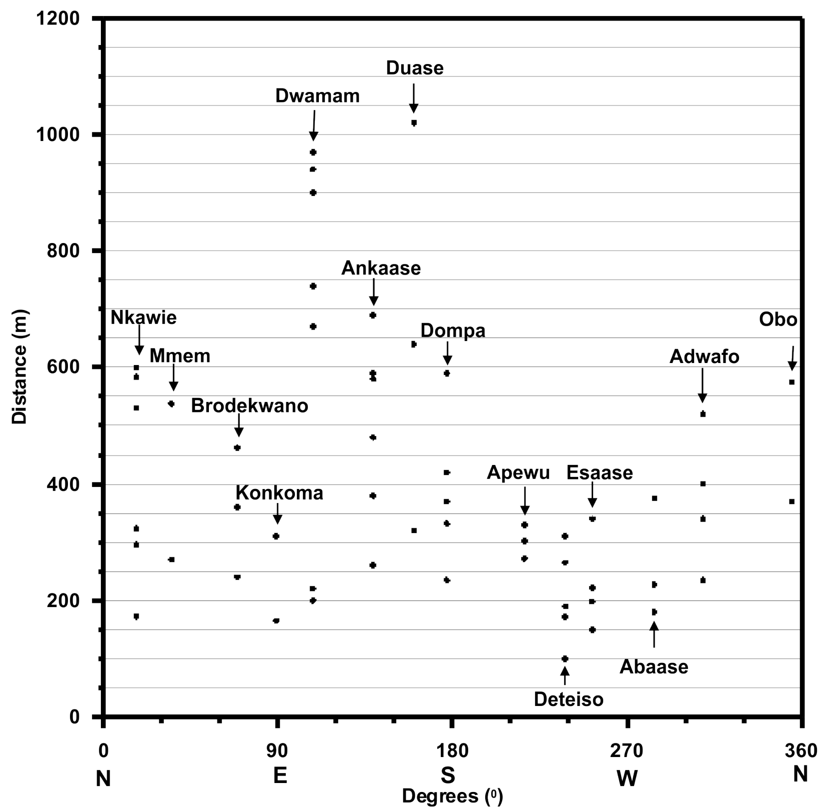

Figure 7.4 – Inferred fault lines around the lake

7.2 Statistical Analysis of the faults

The von Mises distribution and Fisher statistics were used to characterize the dip of the faults identified on the eastern and western parts of the crater (Figure 7.5 and Table 7.2). The resultant length, R, the mean resultant length, $\bar{R}$, the mean direction, $\bar{\theta}$ and the standard error, s_e were calculated using Equations (5.5), (5.6), (5.3) and (5.9) respectively. The values of the concentration parameter, κ were estimated using Table C.2 from the calculated values of $\bar{R}$. The measures of dispersion (test for randomness) values $\bar{R}$ and κ exhibits high values in the west and this indicates that the directional measurements in this section are very close to the mean direction (Figure 7.5, Table 7.2).

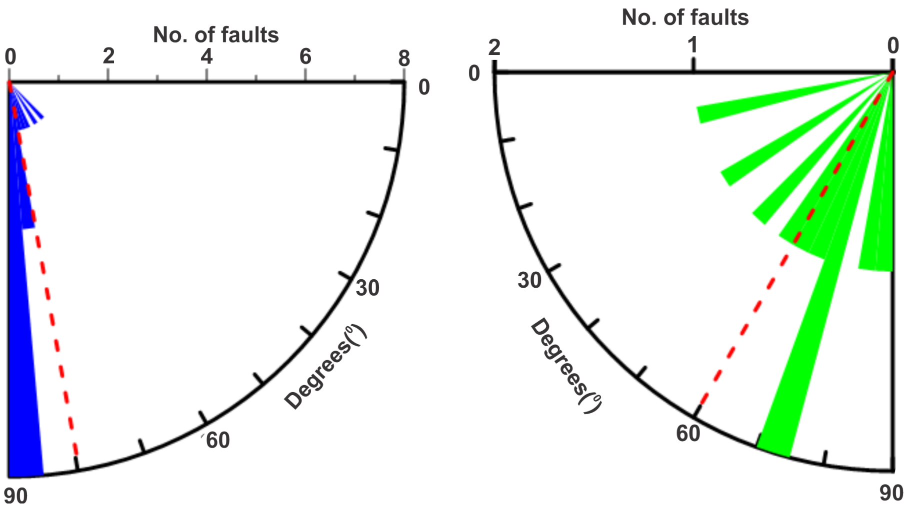

(a) West **(b)** East

Figure 7.5 – Rose plots of the inferred faults on the east and west sections of the lake indicating the angles of dip. The dotted red line is the mean dip of the fault lines

The Rayleigh's test for critical values of $\bar{R}_c$ at 5% level of significance was also estimated (Table 7.2) using Table C.3 from the number of samples n. The critical values were smaller than the computed values and the hypothesis is that, the geologic feature (faults) was not uniformly circularly distributed and the null hypothesis could not be accepted and the faults have a preffered direction.

The rose diagrams (Figure 7.5) show how the faults have been bunched together and it demonstrates that they have preferred direction and are not randomly distributed. And the faults dip steeply towards the lake centre. The s_e indicates the limits of the precision of $\bar{\theta}$.

Table 7.2 – Mean directions and standard errors of the fault lines

Section of crater	n	$\bar{\theta}$	R	$\bar{R}$	$\bar{R}_c$	κ	s_e
East	10	60.33	9.32	0.93	0.54	7.43	6.85
West	16	79.62	15.67	0.98	0.43	25.25	2.88

The Fisher statistics was used for the comparison of the two mean directions (East and West). The test values, F_T were calculated using Equation (5.12). The resultant length R_p and the standardized resultant $\bar{R}_p$ of the pooled vectors were also calculated from Equations (5.5) and (5.6) respectively. The critical values F_c at 5% were estimated from Table C.1 with two degrees of freedom, 1 and 24. From Table 7.3, the observed statistics F_T value exceeds the tabulated F_c value at the 5% level of significance indicate that the two mean directions are different.

Table 7.3 – Resultants of the sampled and pooled fault lines

Section of crater	N	R_T	R_p	$\bar{R}_p$	κ	F_T	F_c
East–West	26	24.98	24.64	0.95	10.27	7.78	4.26

7.3 Direction of the Meteorite

Numerical modelling by Artemieva et al. (2004) suggested that the crater was produced by a 0.75–1 km bolide with a velocity of 15 kms^{-1} and impacted between 30° – 45° and in the N–NE to S–SW. The interpretation of the fault lines in the crater indicates that the impactor came from the NE as greater proportion of the energy (momentum) was in the downrange (SW) direction and this portion of the crater experienced a greater degree of faulting. This preferential direction of faulting shows the transport direction of the material and indicates the impact vector. The analysis of the slopes of the bedrock also supports a NE impactor.

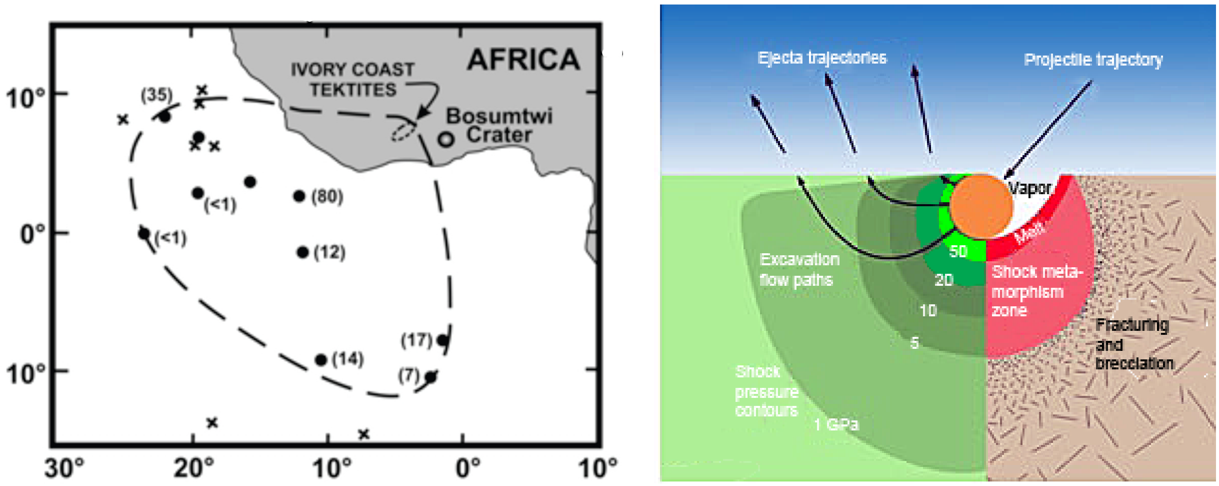

(a) (b)

Figure 7.6 – (a) Location of the Bosumtwi impact crater in relation to the Ivory Coast tektites strewnfield and the deep-sea microtektites (Glass et al., 1991) (b) Initial shock wave pressures and excavation flow lines around an oblique impact point modified from (Kring, 2006)

The directions of oblique impact ejecta (Figure 7.6b) and the distribution of the tektites in Ivory Coast and the deep-sea microtektites off the coast of West Africa (Figure 7.6a) also supports an impactor coming from the NE because the tektites strewnfield lies in the SW quadrant of the crater (Artemieva et al., 2004). The distribution of distal ejecta (tektites) is a strong indicator of the impact trajectory. For the suevites distribution, those in the N-NE was ejected in the uprange direction whereas that in the SW was in the downrange direction of the impactor.

CHAPTER 8

CONCLUSIONS AND OUTLOOK

Electrical resistivity tomography (ERT) has been used successfully at the Bosumtwi impact crater to map the inner wall of the crater, delineate the sediment and bedrock contact, and other impact related structures (dike breccias, autochthonous breccias, allochthonous breccias, faults and fractures) of this topographically varied environment. This is the first surface electrical resistivity measurements to be carried out in the Lake Bosumtwi impact crater. In all sixteen 2D resistivity images were acquired radially around the lake from the shore uphill towards the rim.

The area extending from the lake shore towards the crater rim contains essentially three different formations. First, the low resistivity regions (< 64 Ω.m) extending from the lake shore towards the rim represent the post impact lake sediments. Second, the moderately high resistivity regions with values between 128 and 200 Ω.m were interpreted as impact related breccias (dike, autochthonous and allochthonous) based on their resistivity and geometry. Third, the high resistivity regions (> 128 Ω.m) as representing the metasedimentary target rocks consisting of metagreywackes and phyllite to slate because of their resistivity, geometry and lateral extent.

The ERTs also highlighted areas characterised by faults and fractures. The fractures were interpreted to be filled with either clasts or polymict breccia matrix. Most of the fractures were observed on the tomograms in the southeastern portion of the crater. A direct correspondence between the lithology were identified on the surface and the subsurface resistivity were observed at Dwamam and Nkawie.

The sediment/bedrock contact dips between the lowest of 16° in the NE to the highest of 36° in the SW. The sediment/bedrock surface is symmetrical in the NE–SW direction. The dips of the faults and/or fractures average about 60° and 80° in the east and west parts of the crater respectively. What appear to be concentric faults were mapped on the western profiles: first on the Adwafo, Abaase and Esaase profiles and again on the Esaase and Deteiso traverses and lastly on the Deteiso and Apewu tomograms.

Statistical analysis of the faults revealed that the mean directions of the faults in the east and the west are different and that they are not randomly distributed but have a preferred direction. The individual directional measurements of the faults in the west are closer to their mean direction than those in the east.

The data from the sediment/bedrock boundary and the inferred faults and the locations of the Ivory Coast tektites and deep–sea microtektites indicates that the impactor most probably came from the NE.

The geo–electrical data has added value to the knowledge of one of the well preserved impact craters on earth. The findings have revealed the crater geometry and this will contribute to future numerical modelling of the crater and the use of ERT in impact cratering studies.

Bibliography

ABEM, A. I. (2008). *Instruction manual, Terrameter SAS4000/SAS1000*.

Ahrens, T. J. and O'Keefe, J. D. (1977). *Equations of State and impact-induced shock-wave attenuation on the Moon, In: Impact and Explosion Cratering: Planetary and Terrestrial Impact Implications*. Pergamon, New York.

Alvarez, L. W. (1997). T. Rex and the Crater of Doom. *Princeton Univ.,Princeton*, page 185 pp.

Alvarez, L. W., Alvarez, W., Asaro, F., and Michel, H. V. (1980). Extraterrestrial cause for the Cretaceous-Tertiary extinction. *Science*, 208:1095–1108.

Apparao, A., Rao, T. G., Sastry, R. S., and Sarma, V. S. (1992). Depth of detection of buried conductive targets with different electrode arrays in resistivity prospecting. *Geophysical Prospecting*, 40:749–760.

Archie, G. E. (1942). The electrical resistivity log as an aid in determining some reservoir characteristics. *Transactions of the American Institute of Mining, Metallurgical and Petroleum Engineering*, (146):54–62.

Artemieva, N. (2007). Possible reasons of shock melt deficiency in the Bosumtwi drill cores. *Meteoritics and Planetary Science*, 42(4/5):883–894.

Artemieva, N., Karp, T., and Milkereit, B. (2004). Investigating the Lake Bosumtwi impact structure: Insight from numerical modeling. *Geochemistry, Geophysics and Geosystems: An Electronic Journal of the Earth Sciences*, 5(11).

Aubert, M., Camus, G., and Fournier, W. (1984). Resistivity and magnetic surveys in groundwater prospecting in volcanic areas – Case history Maar of Beaunit, Puy de Dome, France. *Geophysical Prospecting*, 32:554–563.

Auken, E. and Christiansen, A. V. (2004). Layered and laterally constrained 2D inversion of resistivity data. *Geophysics*, 69:752–761.

Bampo, S. O. (1963). Kumasi conference on the Lake Bosumtwi Crater. *Nature*, 198:1150–1151.

Barsukov, O. M. (1970). Relationship between the electrical resistivity of rocks and tectonic processes,izv. *Acad. Sci., USSR Phys. Solid Earth, Engl. Transl.*, (1):55–59.

Beard, L. P. and Tripp, A. C. (1995). Investigating the resolution of IP arrays using inverse theory. *Geophysics*, 60(5):1326–1341.

Boamah, D. (2001). *Bosumtwi Impact Structure, Ghana: petrography and geochemistry of target rocks and impactites, with emphasis on shallow drilling project around the crater*. PhD thesis, University of Vienna, Austria.

Boamah, D. and Koeberl, C. (2002). Geochemistry of soils from the Bosumtwi Impact Structure, Ghana, and relationship to radiometric airborne geophysical data. – in: J. Plado & L. Pesonen (eds.): Meteorite Impacts in Precambrian Shields. *Heidelberg – Berlin (Springer)*, Impact Studies vol. 2:211–255.

Boamah, D. and Koeberl, C. (2003). Geology and geochemistry of shallow drill cores from the Bosumtwi Impact Structure, Ghana. *Meteoritics and Planetary Science*, 38:1137–1159.

Boamah, D. and Koeberl, C. (2006). Petrographic studies of fallout suevite from outside the Bosumtwi Impact Crater, Ghana. *Meteoritics and Planetary Science*, 41:1761–1774.

Butler, R. F. (1992). *Paleomagnetism: Magnetic Domains to Geologic Terranes*. Blackwell Science Publications.

Camus, G. (1975). *La Chaîne des Puys (Massif Central Français). Etude structurale et volcanologique*. PhD thesis, Univ. de Clermont-Ferrand.

Channell, J., Mazaud, A., Sullivan, P., Turner, S., and Raymo, M. (2002). Geomagnetic excursions and paleointensities in the 0.9–2.15 Ma interval of the Matuyama Chron at ODP Site 983 and 984 (Iceland basin). *Journal of Geophysical Research*, 107/6:1–14, doi: 10.1029/2001JB000491.

Claerbout, J. F. and Muir, F. (1973). Robust modeling with erratic data. *Geophysics*, 38:826–844.

Colangelo, G., Lapenna, V., Loperte, A., Perrone, A., and Telesca, L. (2008). 2D electrical resistivity tomographies for investigating recent activation landslides in Basilicata Region (Southern Italy). *Annals of Geophysics*, 51(1):275–285.

Colella, A., Lapenna, V., and Rizzo, E. (2004). High-resolution imaging of the high Agri valley basin (Southern Italy) with the electrical resistivity tomography. *Tectonophysics*, 386(1-2):29–40.

Coney, L., Gibson, R. L., Reimold, W. U., and Koeberl, C. (2007a). Lithostratigraphic and petrographic analysis of ICDP drill core LB-07A, Bosumtwi Impact Structure, Ghana. *Meteoritic and Planetary Science*, 42(4/5):569–589.

Coney, L., Reimold, W. U., Gibson, R. L., and Koeberl, C. (2007b). Geochemistry of impactites and basement lithologies from ICDP borehole LB-07A, Bosumtwi Impact Structure, Ghana. *Meteoritics and Planetary Science*, 42(4/5):667–688.

Constable, S. C., Parker, R. L., and Constable, C. G. (1987). Occam's inversion : A practical algorithm for generating smooth models from electromagnetic sounding data. *Geophysics*, 52(3):289–300.

Dahlin, T. (1996). 2D resistivity surveying for environmental and engineering applications. *First Break*, 14:275–284.

Dahlin, T. and Loke, M. H. (1998). Resolution of 2D wenner resistivity imaging as assessed by numerical modelling. *Journal of Applied Geophysics*, 38:237–249.

Dahlin, T. and Zhou, B. (2004). A numerical comparison of 2D resistivity imaging with ten electrode arrays. *Geophysical Prospecting*, 52:379–398.

Dahlin, T. and Zhou, B. (2006). Multiple-gradient array measurements for multichannel 2D resistivity imaging. *Near Surface Geophysics*, pages 113–123.

Dai, X., Boamah, D., Koeberl, C., Reimold, W. U., Irvine, G., and McDonald, I. (2005). Bosumtwi Impact Structure, Ghana: Geochemistry of impactites and target rocks, and search for meteoritic component. *Meteoritic and Planetary Science*, 40(9 and 10):1493–1511.

Danuor, S. K. (2004). *Geophysical investigations of the Bosumtwi Impact Crater and comparison with terrestrial meteorite craters of similar age and size.* PhD thesis, Kwame Nkrumah University of Science and Technology, Kumasi, Ghana.

Danuor, S. K. and Menyeh, A. (2006). Results of pre-drilling potential field measurements at the Bosumtwi crater. *Meteoritics and Planetary Science*, 42:541–547.

Davis, D. W., Hirdes, W., Schaltegger, U., and Nunoo, E. A. (1994). Upb age constraints on deposition and provenance of Birimian and gold-bearing Tarkwaian sediments in Ghana, West Africa. *Precambrian Research*, 67:89–107.

Davis, J. C. (2002). *Statistics and Data Analysis in Geology*. John Wiley and Sons, 3rd edition edition.

deGroot-Hedlin deGroot-Hedlin deGroot Hedlin, C. and Constable, S. (1990). Occam's inversion to generate smooth two dimensional models from magnetotelluric data. *Geophysics*, 55:1613–1624.

Dence, M. R. (1968). *Shock zoning at Canadian craters: Petrography and structural implications, In: Shock Metamorphism of Natural Materials, edited by French, B. M., and others*. Mono Book Corp., Baltimore.

Dence, M. R., Grieve, R. A. F., and Robertson, P. B. (1977). *Terrestrial impact structures: Principal characteristics and Energy considerations, In: Impact and Explosion Cratering: Planetary and terrestrial Implications, edited by Roddy, D. J., Pepin, R. O., and Merrill, R. B.* Pergamon, New York.

Deutsch, A., Luetke, S., and Heinrich, V. (2007). The ICDP Lake Bosumtwi impact crater scientific drilling project (Ghana): Core LB-08A litho-log, related ejecta, and shock recovery experiments. *Meteoritics and Planetary Science*, 42(4/5):635–654.

Dey, A., Meyer, W. H., Morrison, H. F., and Dolan, W. M. (1975). Electric field response of two-dimensional inhomogeneities to unipolar and bipolar electrode configurations. *Geophysics*, 40(4):630–640.

Dey, A. and Morrison, H. F. (1979a). Resistivity modeling for arbitrarily shaped three dimensional shaped structures. *Geophysics*, 44:753–780.

Dey, A. and Morrison, H. F. (1979b). Resistivity modelling for arbitrary shaped two-dimensional structures. *Geophysical Prospecting*, 27:106–136.

Diaferia, I., Barchi, M., Loddo, M., Schiavone, D., and Siniscalchi, A. (2006). Detailed imaging of tectonic structures by multiscale earth resistivity tomographies: The Colfiorito normal faults (Central Italy):. *Geophysical Research Letters*, 33(9):L09305.1–L09305.4.

Donofrio, R. R. (1997). Survey of hydrocarbon-producing impact structures in North America: Exploration results to date and potential for discovery in Precambrian basement rock. *Oklahoma Geol. Survey*, Circ. 100:17–29.

Dressler, B. O., Grieve, R. A. F., and Sharpton, V. L. (1994). Large Meteorite Impacts and Planetary Evolution. *Geol. Soc. Amer*, Spec. Paper 293:348 pp.

Dressler, B. O., Sharpton, V. L., and Schuaytz, B. C. (1998). Shock metamorphism and shock barometry at a complex impact structure: Slate Islands, Canada. *Contribution to Mineralology and Petrology*, 130.

EarthImpactDatabase (Acessed 5th January, 2012). Earth Impact Database. *http://www.passc.net/EarthImpactDatabase/IntrotoImpacts.html*.

Elbra, T., Kontny, A., Pesonen, L. J., Schleifer, N., and Schell, C. (2007). Petrophysical and paleomagnetic data of drill cores from the Bosumtwi Impact Structure, Ghana. *Meteoritics and Planetary Science*, 42(4/5):829–838.

Ellis, R. G. and Oldenburg, D. W. (1994). Applied geophysical inversion. *Geophysical Journal International*, 116:5–11.

Erickson, J. (2003). *Asteroids, Comets and Meteorites. Cosmic Invaders of the Earth*. Facts On File Inc.

Fergusson, M. (1902). Lake Bosumtwi. *Geographical Journal*, 19:370–372.

Ferriére, L., Koeberl, C., and Reimold, W. U. (2006a). Shock metamorphic effects in samples from core LB-08A: First material recovered from the central uplift of the Bosumtwi Impact Structure, Ghana (abstract). In *Workshop on Impact Craters as Indicators for Planetary Environmental Evolution and Astrobiology*.

Ferriére, L., Koeberl, C., and Reimold, W. U. (2007a). Drill core LB-08A, Bosumtwi impact structure, Ghana: Petrographic and shock metamorphic studies of material from the central uplift. *Meteoritic and Planetary Science*, 42(4/5):611–633.

Ferriére, L., Koeberl, C., Reimold, W. U., and Gibson, R. L. (2006b). First mineralogical observations and chemical analyses of core LB-08A from the central uplift of the Bosumtwi Impact Structure, Ghana: Comparison with suevite from outside the crater (abstract #1845). In *37th Lunar and Planetary Science Conference*. CD-ROM.

Ferriére, L., Koeberl, C., Reimold, W. U., and Mader, D. (2007b). Drill core LB-08A, Bosumtwi Impact Structure, Ghana: Geochemistry of fallback breccia and basement samples from the central uplift. *Meteoritics and Planetary Science*, 42(4/5):689–708.

French, B. M. (1998). *Traces of Catastrophe: A Handbook of Shock-Metamorphic Effects in Terrestrial Meteorite Impact Structures*, volume LPI Contribution 954.

Gault, D. E., Quiade, W. L., and Oberbeck, V. R. (1968). *Impact cratering mechanics and structures. In: Shock Metamorphism of Natural Materials*. Mono Book Corp, Baltimore.

Gentner, W. (1966). Auf der Suche nach Kratergläsern, Tektiten und Meteoriten in Afrika. *Naturwissenschaften*, 12:285–289.

Gentner, W., Kleinmann, B., and Wagner, G. A. (1967). New K–Ar and fission track ages of impact glasses and tektites. *Earth and Planetary Science Letters*, 2:83–86.

Gentner, W., Lippolt, H. J., and Muller, O. (1964). Das Kalium-Argon-Alter des Bosumtwi Kraters in Ghana und die chemische Beschaffenheit seiner Glässer. *Zeitschrift für Naturforschung*, 19A:150–153.

Giocoli, A., Magri, C., Vannoli, P., Piscitelli, S., Rizzo, E., Siniscalchi, A., Burrato, P., Basso, C., and Nocera, C. D. (2008). Electrical resistivity tomography investigations in the Ufita Valley (Southern Italy). *Annals of Geophysics*, 51(1):213–223.

Glass, B. P. (1968). Glassy objects (microtektites?) from deep sea sediments near the Ivory Coast. *Science*, 161:891–893.

Glass, B. P. (1969). Chemical composition of Ivory Coast microtektites. *Geochimica et Cosmochimica Acta*, 33:1135–1147.

Glass, B. P., Kent, D. V., Schneider, D. A., and Tauxe, L. (1991). Ivory Coast microtektite strewn field: Description and relation to the Jaramillo geomagnetic event. *Earth and Planetary Science Letters*, 107:182–196.

Glass, B. P. and Pizzuto, J. E. (1994). Geographic variations in Australasian microtektite concentrations: Implications concerning the location and size of the source crater. *Journal of Geophysical Research*, 99:19075–19081.

Glass, B. P., Swincki, M. B., and Zwart, P. A. (1979). Australasian, Ivory Coast and North American tektite strewn field: Size, mass and correlation with geomagnetic reversals and other earth events. *Proceedings of the 10th Lunar and Planetary Science Conference*, pages 2535–2545.

Glass, B. P. and Zwart, P. A. (1979). The Ivory Coast microtektite strewn field: New data. *Earth and Planetary Science Letters*, 43:336–342.

Goderis, S., Tagle, R., Schmitt, R. T., Erzinger, J., and Claeys, P. (2007). Platinum group elements provide no indication of a meteoritic component in ICDP cores from the Bosumtwi crater, Ghana. *Meteoritics and Planetary Science*, 42(4/5):731–741.

Grieve, R. A. F. (1987). Terrestrial impact structures. *Annals Reviews Earth Planetary Science*, 15:245–270.

Grieve, R. A. F. (1991). Terrestrial impact: The record in the rocks. *Meteoritics*, 26:175–194.

Grieve, R. A. F., Dence, M. R., and Robertson, P. B. (1977). *Cratering process: As interpreted from the occurrence of impact melts. In: Impact and Explosion Cratering: Planetary and Terrestrial Impact Implications*. Pergamon, New York.

Grieve, R. A. F. and Masaitis, V. L. (1994). The economic potential of terrestrial impact craters. *Intl. Geol. Rev*, 36:105–151.

Grieve, R. A. F. and Pesonen, L. J. (1992). The terrestrial impact cratering record. *Tectonophysics*, 216:1–30.

Grieve, R. A. F. and Pilkington, M. (1996). The geophysical signature of terrestrial impacts. *AGSO Journal of Australian Geology and Geophysics*, 16:399–420.

Grieve, R. A. F., Robertson, P. B., and Dence, M. R. (1981). *Constraints on the formation of ring impact structures, based on terrestrial data. In Multi-Ring Basins: Formation and Evolution*. Pergamon, New York, 12a (p. h. schultz and r. b. merrill, eds.) edition.

Griffiths, D. H. and Barker, R. D. (1993). Two-dimensional resistivity imaging and modelling in areas of complex geology. *Journal of Applied Geophysics*, 29:211–226.

Gunther, T., Rucker, C., and Spitzer, K. (2006). Three dimensional modeling and inversion of dc resistivity data incorporating topography–ii inversion. *Geophysical Journal International*, 166:506–517.

Guy-Bray, J. V. (1972). New Developments in Sudbury Geology. *Geol. Assoc. Canada*, Spec. Paper 10:124 pp.

Hildebrand, A. R., Penfield, G. T., Kring, D. A., Pilkington, M., Camargo-Zanoguera, A., Jacobsen, S. B., and Boynton, W. V. (1991). Chicxulub crater: A possible Cretaceous- Tertiary boundary impact crater on the Yucatán Peninsula, Mexico. *Geology*, 19:867–871.

Hirdes, W., Davis, D. W., Ludtke, G., and Konan, G. (1996). Two generations of Birimian (Paleoproterozoic) volcanic belts in northeastern Cote d'Ivoire (West Africa): Consequences for the–Birimian controversy. *Precambrian Research*, 80:173–191.

Horz, F., Grieve, R. A. F., Heiken, G., Spudis, P., and Binder, A. (1991). *Lunar surface processes. In Lunar Sourcebook: A User's Guide to the Moon*. Cambridge Univ., New York.

Hunze, S. and Wonik, T. (2007). Lithological and structural characteristics of the lake Bosumtwi Impact Crater, Ghana: Interpretation of acoustic televiewer images. *Meteoritics and Planetary Science*, 42(4/5):779–792.

Inman, J. R. (1975). Resistivity inversion with ridge regression. *Geophysics*, 40:798–817.

Jannot, S., Schiano, P., and Boivin, P. (2005). Melt inclusions in scoria and associated mantle xenoliths of Puy Beaunit Volcano, Chaîne des Puys, Massif Central, France. *Spinger-Verlag*, 149:600–612.

Johnson, K. S. and Campbell, J. A. (1997). Ames structure in northwest Oklahoma and similar features: Origin and petroleum production (1995 symposium). *Oklahoma Geol. Survey*, Circ. 100:396 pp.

Jones, W. B. (1985a). Chemical analysis of Bosumtwi crater target rocks compared with Ivory Coast tektites. *Geochimica et Cosmochimica Acta*, 49:2569–2576.

Jones, W. B. (1985b). The origin of the Bosumtwi crater, Ghana – an historical review. *Proceedings of the Geological Association (London)*, 96:275–284.

Jones, W. B., Bacon, M., and Hastings, D. A. (1981). The Lake Bosumtwi Impact Crater, Ghana. *Geological Society of America Bulletin*, 92:342–349.

Junner, N. R. (1937). The geology of the Bosumtwi caldera and surrounding country. *Gold Coast Geological Survey Bulletin*, 8:1–38.

Karikari, F., Ferriére, L., Koeberl, C., Reimold, W. U., and Mader, D. (2007). Petrography, geochemistry, and alteration of country rocks from the Bosumtwi Impact Structure, Ghana. *Meteoritics and Planetary Science*, 42(4/5):513–540.

Karp, T. (2002). *Seismische Untersuchung des Lake Bosumtwi–Impaktkrater, Ghana*. PhD thesis, Universität zu Kiel.

Karp, T., Milkereit, B., Janle, P., Danuor, S. K., Pohl, J., Berckhemer, H., and Scholz, C. A. (2002). Seismic investigation of the Lake Bosumtwi impact crater: Preliminary results. *Planetary and Space Science*, 50:735–743.

Kearey, P., Brooks, M., and Hill, I. (2002). *An Introduction to Geophysical Exploration*. Blackwell Science, 3rd edition edition.

Kieffer, S. W. and Simonds, C. H. (1980). The role of volatiles and lithology in the impact cratering process. *Reviews of Geophysics and Space Physics*, 18:143–181.

Kitson, A. K. (1916). The Gold Coast: some consideration of its structure, people and natural history. *Geographical Journal*, 48:369–392.

Koeberl, C. (1994). African meteorite impact craters: Characteristics and geological importance. *Journal of African Earth Sciences*, (18):263–295.

Koeberl, C. and Anderson, R. R. (1996). The Mason Impact Structure, Iowa: Anatomy of an Impact Crater. *Geological Society of America Special Paper*, 302:468pp.

Koeberl, C., Bottomley, R. J., Glass, B. P., and Storzer, D. (1997a). Geochemistry and age of Ivory Coast tektites and microtektites. *Geochimica et Cosmochimica Acta*, 61:1745–1772.

Koeberl, C., Brandstatter, F., Glass, B. P., Hecht, L., Mader, D., and Reimold, W. U. (2007a). Uppermost impact fallback layer in the Bosumtwi crater (Ghana): Mineralogy, geochemistry, and comparison with Ivory Coast tektites. *The Meteoritical Society*, 42(4/5):709–729.

Koeberl, C., Milkereit, B., Overpeck, J. T., Scholz, C. A., Amoako, P. Y. O., Boamah, D., Danuor, S. K., Karp, T., Kueck, J., Hecky, R. E., King, J. W., and Peck, J. A. (2007b). An international and multidisciplinary drilling project into a young complex impact structure: The 2004 ICDP Bosumtwi Crater Drilling Project–An overview. *Meteoritics and Planetary Science*, 42(4/5):483–511.

Koeberl, C., Milkereit, B., Overpeck, J. T., Scholz, C. A., and Peck, J. (2005). The 2004 ICDP Bosumtwi Impact Crater, Ghana, West Africa, drilling project: A first report (abstract #1830). In *36th Lunar and Planetary Science Conference*. CD-ROM.

Koeberl, C. and Reimold, W. U. (2005). Bosumtwi Impact Crater, Ghana (West Africa): An updated and revised geological map, with explanations. *Jahrbuch der Geologischen Bundesanstalt*, 145(1):31–70.

Koeberl, C., Reimold, W. U., Blum, J. D., and Chamberlain, C. P. (1998). Petrology and geochemistry of target rocks from the Bosumtwi Impact Structure, Ghana, and comparison with Ivory Coast tektites. *Geochimica et Cosmochimica Acta*, 62:2179– 2196.

Koeberl, C., Reimold, W. U., Pesonen, L. J., and Brandt, D. (1997b). New studies of Bosumtwi Impact Structure, Ghana: The 1997 field season. *Meteoritic and Planetary Science*, 32:A72–A73 (Abstract).

Kontny, A., Elbra, T., Just, J., Pesonen, L. J., Schleicher, A. M., and Zolk, J. (2007). Petrography and shock-related remagnetization of pyrrhotite in drill cores from the Bosumtwi Impact Crater Drilling Project, Ghana. *Meteoritics and Planetary Science*, 42(4/5):811–827.

Kring, D. A. (2006). Geological effects of impact cratering.

LaBrecque, D. J., Miletto, M., Daily, W., Ramirez, A., and Owen, E. (1996). The effect of noise on Occam's inversion of resistivity tomography data. *Geophysics*, 61(2):538–548.

Lacroix, A. (1934). Sur la découverte de tectites à la Côte d'Ivoire. *Comptes Rendus Academie des Sciences Paris*, 199:1539–1542.

Lapenna, V., Lorenzo, P., Perrone, A., Piscitelli, S., Rizzo, E., and Sdao, F. (2005). Case history: 2D electrical resistivity imaging of some complex landslides in Lucanian Apennine (Southern Btaly). *Geophysics*, 70(3):B11–B18.

Lehmann, H. (1995). Potential representation by independent configurations on a multielectrode array. *Geophysical Journal International*, 120:331–338.

Lesur, V., Cuer, M., and Straub, A. (1999a). 2-D and 3-D interpretation of electrical tomography measurements, Part 1. *Geophysics*, 64(2):386–395.

Lesur, V., Cuer, M., and Straub, A. (1999b). 2-D and 3-D interpretation of electrical tomography measurements, Part 2. *Geophysics*, 64(2):396–402.

Leube, A., Hirdes, W., Mauer, R., and Kesse, G. O. (1990). The early Proterozoic Birimian Supergroup of Ghana and some aspects of its associated gold mineralization. *Precambrian Research*, 46:139–165.

Levenberg, K. (1994). A method for the solution of certain problems in least squares. *Quart. Appl. Math.*, 2:164–168.

L'Heureux, E. and Milkereit, B. (2007). Impactites as a random mediumâĂŤusing variations in physical properties to assess heterogeneity within the Bosumtwi meteorite impact crater. *Meteoritics and Planetary Science*, 42(4/5):849–858.

Li, Y. and Oldenburg, D. W. (1994). Inversion of 3-D DC resistivity data using an approximate inverse mapping. *Geophysical Journal International*, 116:527–537.

Lightfoot, P. C. and Naldrett, A. J. (1994). Proceedings of the Sudbury–Noril'sk symposium. *Ontario Geol. Survey*, Spec. Vol. 5:421 pp.

Lines, L. R. and Treitel, S. (1984). Tutorial: A review of least-squares inversion and its application to geophysical problems. *Geophysical Prospecting*, 32:159–186.

Lippolt, H. J. and Wasserburg, G. H. (1966). Rubidium-Strontium Messungen an Glässern von Bosumtwi-Krater und an Elfenbeinkusten-Tektiten. *Zeitschrift für Naturforschung*, 21A:226–231.

Livet, M., Blavoux, B., d'Arcy d'Arcy d'Arcy, D., and Mishellany, A. (2000). Capture et emmagasinement sous coulée au site volcanique de Beaunit (Puy-de-Dôme). *Earth and Planetary Sciences*, 330:47–52.

Loke, M. H. (2011). Tutorial: 2-D and 3-D Electrical Imaging Survey. *Manual*.

Loke, M. H., Acworth, I., and Dahlin, T. (2003). A comparison of smooth and blocky inversion methods in 2-D electrical imaging surveys. *Exploration Geophysics*, 34:82–187.

Loke, M. H. and Barker, R. D. (1996a). Practical techniques for 3D resistivity surveys and data inversion. *Geophysical Prospecting*, 44:499–523.

Loke, M. H. and Barker, R. D. (1996b). Rapid least-squares inversion of apparent resistivity pseudosections by a quasi-Newton method. *Geophysical Prospecting*, 44:131–152.

Lowrie, W. (2007). *Fundamentals of Geophysics*. Cambridge University Press, 2nd edition edition.

Lowry, T., Allen, M. B., and Shive, P. N. (1989). Singularity removal: A refinement of resistivity modeling techniques. *Geophysics*, 54(6):766–774.

Maclaren, M. (1931). Lake Bosumtwi, Ashanti. *Geographical Journal*, 78:270–276.

Marquardt, D. (1963). An algorithm for least-squares estimation of nonlinear parameters. *SAIM. J. Appl. Math.*, 11:431–441.

Maurer, H., Holliger, K., and Boerner, D. E. (1998). Stochastic regularization: Smoothness or similarity? *Geophysical Research Letters*, 25(15):2889–2892.

McDonald, I., Peucker-Ehrenbrink, B., L.Coney, Ferriére, L., Reimold, W. U., and Koeberl, C. (2005). Search for meteoritic component in drill cores from Bosumtwi Impact Structure, Ghana: Platinum group element contents and osmium isotopoc characteristics. *The Meteoritical Society*, 40(9 and 10):1493–1511.

McLaren, D. J. and Goodfellow, W. D. (1990). Geological and biological consequences of giant impacts. *Annu. Rev. Earth Planet. Sci*, 18:123–171.

Melosh, H. J. (1989). *Impact Cratering – A Geologic Process*. Oxford.

Menke, W. (1984). *Geophysical Data Analysis: Discrete Inverse Theory*. Academic Press, Orlando, Florida.

Milkereit, B., Ugalde, H., Karp, T., Scholz, C. A., Schmitt, D., Danuor, S. K., Artemieva, N., Kück, J., Qian, W., and L'Heureux, E. (2006). Exploring the Lake Bosumtwi crater–Geophysical surveys, predictions and drilling results (abstract #1687). In *37th Lunar and Planetary Science Conference*. CD-ROM.

Milsom, J. (2003). *Field Geophysics. The Geological Field Guide Series*. John Wiley and Sons, 3rd edition edition.

Milton, D. J., Barlow, B. C., Brett, R., Brown, A. R., Glikson, A. Y., Manwaring, E. A., Moss, F. J., Sedmik, E. C. E., Son, J. V., and Young, G. A. (1972). Gosses Bluff impact structure, Australia. *Science*, 175:1199–1207.

Milton, D. J., Barlow, B. C., Brown, A. R., Moss, F. J., Manwaring, E. A., Sedmik, E. C. E., Young, G. A., and Son, J. V. (1996a). Gosses Bluff–a latest Jurassic impact structure, central Australia. Part II: Seismic, magnetic, and gravity studies. *AGSO J. Austral. Geol. Geophys.*, 16:487–527.

Milton, D. J., Glikson, A. Y., and R.Brett (1996b). Gosses Bluff–a latest Jurassic impact structure, central Australia. Part I: Geological structure, stratigraphy, and origin. *AGSO J. Austral. Geol. Geophys.*, 16:453–468.

Møller, I., Jacobsen, B. H., and Christensen, N. B. (2001). Rapid inversion of 2-D geoelctrical data by multichannel deconvolution. *Geophysics*, 66(3):800–808.

Montanari, A. and Koeberl, C. (2000). Impact stratigraphy: The Italian Record. - lecture notes in Earth Sciences. *Heidelberg (Springer Verlag)*, 93:364 pp.

Moon, P. A. and Mason, D. (1967). The geology of 1/4° field sheets 129 and 131, Bompata S.W and N.W. *Ghana Geological Survey Bulletin*, 31:1–51.

Morgan, J., Group, M., Brittan, J., Buffler, R., Camargo, A., Christeson, G., Denton, P., Hilderbrand, A., Hobbs, R., Macintyre, H., Mackenzie, G., Maguire, P., Marin, L., Nakamura, Y., Pilkington, M., Sharpton, V. L., Snyder, D., Suarez, G., and Trejo, A. (1997). Size and morphology of the Chicxulub impact crater. *Nature*, 390:472–476.

Morris, W. A., Ugalde, H., and Clark, C. (2007a). Physical property measurements: ICDP boreholes LB-07A and LB-08A, Lake Bosumtwi Impact Structure, Ghana. *Meteoritics and Planetary Science*, 42(4/5):801–809.

Morris, W. A., Ugalde, H., Clark, C., and Miles, B. (2007b). Clast fabric examination of impact-generated breccias, borehole LB-07A, Bosumtwi, Ghana. *Meteoritics and Planetary Science*, 42(4/5):769–778.

Morrow, J. R. (2007). Shock-metamorphic petrography and microRaman spectroscopy of quartz in upper impactite interval, ICDP drill core LB-07A, Bosumtwi Impact Crater, Ghana. *Meteoritic and Planetary Science*, 42(4/5):591–609.

Mufti, I. (1976). Finite-difference resistivity modeling for arbitrarily shaped two-dimensional structures. *Geophysics*, 41(1):62–78.

Oberthür, T., Vetter, U., Davis, D. W., and Amanor, J. A. (1998). Age constraints on gold mineralization and palaeoproterozoic crustal evolution in the Ashanti belt of southern Ghana. *Precambrian Research*, 89:129–143.

O'Keefe, J. D. and Ahrens, T. J. (1982). Cometary and meteorite swarm impact on planetary surfaces. *Journal of Geophysical Research*, 87:6668–6680.

O'Keefe, J. D. and Ahrens, T. J. (1993). Planetary cratering mechanics. *Journal of Geophysical Research*, 98:107011–17028.

Olayinka, A. I. and Yaramanci, U. (2000). Use of block inversion in the 2-D interpretation of apparent resistivity data and its comparison with smooth inversion. *Journal of Applied Geophysics*, 45:63–82.

Oldenburg, D. W. and Li, Y. (1999). Estimating depth of investigation in dc resistivity and IP surveys. *Geophysics*, 64(2):403–416.

Park, S. K. and Van, G. P. (1991). Inversion of pole-pole data for 3-D resistivity structure beneath arrays of electrodes. *Geophysics*, 56(7):951–960.

Pesonen, L. J., Koeberl, C., and Hautaniemi, H. (2003). Airborne geophysical survey of the Lake Bosumtwi meteorite impact structure (Southern Ghana) – Geophysical maps with descriptions. *Jahrbuch der Geologischen Bundesanstalt (Vienna, Austria) (Yearbook of the Geological Survey of Austria)*, 143:581–604.

Pesonen, L. J., Koeberl, C., Ojamo, H., Hautaniemi, H., Elo, S., and Plado, J. (1998). Aerogeophysical studies of the Bosumtwi Impact Structure, Ghana (abstract). *Geological Society of America Abstract with Programs*, 30(7):A–190.

Pesonen, L. J., Plado, J., Koeberl, C., and Elo, S. (1999). The Lake Bosumtwi meteorite impact structure, G: Magnetic modelling (abstract). *Meteoritics and Planetary Science*, 34:A91–A92.

Petersen, M. T., Newsom, H. E., Nelson, M. J., and Moore, D. M. (2007). Hydrothermal alteration in the Bosumtwi impact structure: Evidence from 2MI-muscovite, alteration veins, and fracture fillings. *Meteoritics and Planetary Science*, 42(4/5):655–666.

Pilkington, M. and Grieve, R. A. F. (1992). The geophysical signature of terrestrial impact craters. *Reviews of Geophysics*, 30(2):161–181.

Plado, J., Pesonen, L. J., Koeberl, C., and Elo, S. (2000). The Bosumtwi meteorite impact structure, Ghana: A magnetic model. *Meteoritic and Planetary Science*, 35:723–732.

Poelchau, M. H. and Kenkmann, T. (2008). Asymmetric signatures in simple craters as an indicator for an impact direction. *Meteoritic and Planetary Science*, 43:2059–2072.

Pohl, J. (2001). Distribution of impact craters as at 1992. Personal communication.

Pridmore, D. F., Hohmann, G. W., Ward, S. H., and Sill, W. R. (1981). An investigation of finite-element modeling for electrical and electromagnetic data in three dimensions. *Geophysics*, 46:1009–1024.

Pye, E. G., Naldrett, A. J., and Giblin, P. E. (1984). The geology and ore deposits of the Sudbury structure. *Ontario Geol. Survey*, Spec. Vol. 1:603 pp.

Rattray, R. S. (1923). Ashanti. *Oxford (Clarendon Press/Oxford University Press)*, page 348 pp.

Reimold, W. U., Brandt, D., and Koeberl, C. (1997). Geological studies at Lake Bosumtwi impact crater, Ghana (abstract). *Meteoritics and Planetary Science*, 32(A107).

Reimold, W. U., Brandt, D., and Koeberl, C. (1998). Detailed structural analysis of the rim of a large, complex impact crater: Bosumtwi Crater, Ghana. *Geology*, 26(6):543–546.

Reynolds, J. M. (1997). *An Introduction to Applied and Environmental Geophysics*. John Wiley and Sons.

Robertson, P. B. and Grieve, R. A. F. (1977). *Shock attenuation at terrestrial impact structures. In: Impact and Explosion Cratering: Planetary and Terrestrial Impact Implications, edited by Roddy, D. J., Pepin, R. O., and Merrills, R. B.* Pergamon, New York.

Roddy, D. J., Pepin, R. O., and Merrill, R. B. (1977). *Impact and Explosion Cratering; Planetary and Terrestrial Implications.* Pergamon, New York.

Rohleder, H. (1936). Lake Bosumtwi, Ashanti. *Geographical Journal*, 87:51–65.

Ryder, G., Fastovsky, D., and Gartner, S. (1996). The Cretaceous- Tertiary Event and Other Catastrophes in Earth History. *Geol. Soc. Amer.*, Spec. Paper 307:569 pp.

Sasaki, Y. (1992). Resolution of resistivity tomography inferred from numerical simulation. *Geophysical Prospecting*, 40:453–464.

Sasaki, Y. (1994). 3-D resistivity inversion using the finite-element method. *Geophysics*, 59(11):1834–1848.

Saul, J. M. (1969). Field investigations at Lake Bosumtwi (Ghana) and in the Ivory Coast tektite strewn field. *National Geographic Society Research Reports*, 1964 Proj:201–212.

Scheibz, J., Haeusler, H., Kardeis, G., Kohlbeck, F., Chwatal, W., Figdor, H., and Koenig, C. (2009). Geologic interpretation of geophysical investigations in the Oslip section, Rust Range, Northern Burgenland, Austria, in European Geosciences Union: Vienna, Austria. *Geophysical Research Abstracts*, 11:10559.

Schell, C., Schleifer, N., and Elbra, T. (2007). Characterization of the log lithology of cores LB-07A and LB-08A of the Bosumtwi impact structure by using the anisotropy of magnetic susceptibility. *Meteoritics and Planetary Science*, 42(4/5):839–847.

Schmitt, D. R., Milkereit, B., Karp, T., Scholz, C. A., Danuor, S. K., Meillieux, D., and Welz, M. (2007). In situ seismic measurements in borehole LB-08A in the Bosumtwi Impact Structure, Ghana: Preliminary interpretation. *Meteoritics and Planetary Science*, 42(4/5):755–768.

Schnetzler, C. C., Philpotts, J. A., and Thomas, H. H. (1967). Rare earth and barium abundances in Ivory Coast tektites and rocks from the Bosumtwi crater area, Ghana. *Geochimica et Cosmochimica Acta*, 31:1987–1993.

Schnetzler, C. C., Pinson, W. H., and Hurley, P. M. (1966). Rubidium-strontium age of the Bosumtwi crater area, Ghana, compared with the age of the Ivory Coast tektites. *Science*, 151:817–819.

Scholz, C. A., Karp, T., Brooks, K. M., Milkereit, B., Amoako, P. Y. O., and Arko, J. A. (2002). Pronounced central uplift identified in the Bosumtwi Impact Structure, Ghana, using multichannel seismic reflection data. *Geology*, 30:939–942.

Scholz, C. A., Karp, T., and Lyons, R. P. (2007). Structure and morphology of the Bosumtwi impact structure from seismic reflection data. *Meteoritic and Planetary Science*, 42(4/5):549–560.

Sharma, P. V. (1997). *Environmental and Engineering Geophysics*. Cambridge University Press.

Sharpton, V. L., Dalrymple, G. B., Marin, L. E., Ryder, G., Schuraytz, B. C., and Urrutia-Fucugauchi, J. (1992). New links between the Chicxulub impact structure and the Cretaceous- Tertiary boundary. *Nature*, 359:819–821.

Sharpton, V. L. and Grieve, R. A. F. (1990). Meteorite impact, cryptoexplosion, and shock metamorphism: A perspective on the evidence at the K/T boundary. In: Global Catastrophes in Earth History: An Interdisciplinary Conference on impacts, Volcanism, and Mass Mortality. *Geological Society of America Special Paper*, 247:631pp.

Sharpton, V. L. and Ward, P. D. (1990). Global Catastrophes in Earth History: An Interdisciplinary Conference on Impacts, Volcanism, and Mass Mortality. *Geol. Soc. Amer.*, Spec. Paper 247:631 pp.

Shaw, H. F. and Wasserburg, G. J. (1982). Age and provenance of the target materials for tektites and possible impactites as inferred from Sm-Nd and Rb-Sr systematics. *Earth and Planetary Science Letters*, 60:155–177.

Silver, L. T. and Schultz, P. H. (1982). Geological Implications of Impacts of Large Asteroids and Comets on the Earth. *Geol. Soc. Amer.*, Spec. Paper 190:528 pp.

Silvester, P. P. and Ferrari, R. L. (1990). *Finite elements for electrical engineers*. Cambridge University Press, 2nd edition.

Smit, A. F. J. (1964). Origin of Lake Bosumtwi (Ghana). *Nature*, 203:179–180.

Smith, T., Hoversten, M., Gasperikova, E., and Morrison, F. (1999). Sharp boundary inversion of 2D magnetotelluric data. *Geophysical Prospecting*, 47:469–486.

Spitzer, K. (1995). A 3-d finite-difference algorithm for DC resistivity modelling using conjugate gradient methods. *Geophysical Journal International*, 123:903–914.

Spudis, P. D. (1993). The Geology of Multi-Ring Impact Basins: The Moon and Other Planets. *Cambridge Univ., New York*, page 263 pp.

Steeples, D. W. (2001). Engineering and environmental geophysics at the millennium. *Geophysics*, 66:31–35.

Stöffler, D. and Grieve, R. A. F. (1994). Classification and nomenclature of impact metamorphic rocks: A proposal to the IUGS subcommission on the systematics of metamorphic rocks. – In: A. MONTANARI & J. SMIT (Eds). *Post-Östersund Newsletter, European Science Foundation (ESF) Scientific Network on Impact Cratering and Evolution of Planet Earth, Strasbourg*, pages 9–15.

Storzer, D. and Wagner, G. A. (1977). Fission track dating of meteorite impacts. *Meteoritics*, 12:368–369.

Stummer, P., Maurer, H., and Green, A. (2004). Experimental design: Electrical resistivity data sets that provide optimum subsurface information. *Geophysics*, 69:120–139.

Suzuki, K., Toda, S., Kusunoki, K., Fujimitsu, Y., Mogi, T., and Jomori, A. (2000). Case studies of electrical and electromagnetic methods applied to mapping active faults beneath the thick Quaternary. *Engineering Geology*, 56(1-2):29–45.

Tarantola, A. (1987). Inverse Problem Theory. *Elsevier*.

Telford, W. M., Geldart, L. P., and Sheriff, R. E. (1990). *Applied Geophysics*. Cambridge University Press, 2nd edition edition.

Tong, C. H., Elis, V. R., Lana, C., and Marangoni, Y. R. (2012). Electrical Imaging of Impact Structures.

Tong, C. H., Lana, C., Marangoni, Y. R., and Elis, V. R. (2010). Geoelectric evidence for centripetal resurge of impact melt and breccias over central uplift of Araguainha impact structure. *Geology*, 38:91–94.

Ugalde, H., Danuor, S. K., and Milkereit, B. (2007a). Integrated 3-D model from gravity and petrophysical data at the Bosumtwi Impact Structure, Ghana. *Meteoritics and Planetary Science*, 42(4/5):859–866.

Ugalde, H., Morris, W. A., Pesonen, L. J., and Danuor, S. K. (2007b). The Lake Bosumtwi meteorite impact structure, Ghana– Where is the magnetic source? *Meteoritics and Planetary Science*, 42(4/5):867–882.

Villemant, B., Joron, J. L., Jaffrezic, H., Treuil, M., Maury, R., and Brousse, R. (1980). Cristallisation fractionnée d'un magma basaltique alcalin: la série de la Chaîne des Puys (Massif Central, France). *Géochim Bull Minéral*, 103:267–286.

Wagner, R., Reimold, W. U., and Brandt, D. (2002). Bosumtwi Impact Crater, Ghana: A remote sensing investigation. in Meteorite impacts in Precambrian shields. *Impact Studies, Heidelberg: Springer-Verlag*, 2:189–210.

Watkins, A. P., Iliffe, J. E., and Sharp, W. E. (1993). The effects of extensional and transpressional tectonics upon the development of the Birimian sedimentary facies in Ghana, W. Africa: Evidence from the Bomfa/Beposo District, near Konongo. *Journal of African Earth Sciences*, 17:457–478.

Wolke, R. and Schwetlick, H. (1988). Iteratively reweighted least squares algorithms, convergence analysis, and numerical comparisons. *SIAM Journal of Scientific and Statistical Computations*, 9:907–921.

Woodfield, P. D. (1966). The geology of the 1/4° field sheet 91, Fumso, N.W. Ghana. *Ghana Geological Survey Bulletin*, 30:1–66.

Wright, J. B., Hastings, D. A., Jones, W. B., and Williams, H. R. (1985). Geology and Mineral Resources of West Africa. *Geology and Mineral Resources of West Africa. Allen and Unwin.*

Yang, C. H., Chang, P. H., You, J. I., and Tsai, L. L. (2002). Significant resistivity changes in the fault zone associated with the 1999 Chi-Chi earthquake, west-central Taiwan. *Tectonophysics*, 350:299–313.

Zhao, S. and Yedlin, M. J. (1996). Some refinements on the finite-difference method for 3-D dc resistivity modeling. *Geophysics*, 61(5):1301–1307.

Zhou, B. and Dahlin, T. (2003). Properties and effects of measurement errors on 2D resistivity imaging surveying. *Near Surface Geophysics*, 1:105–117.

Appendices

Appendix A

STUDIES AT BEAUNIT, FRANCE

A.1 Abstract

2D electrical resistivity imaging technique has been used to map the maar of Beaunit. The survey was performed using the Wenner array of 5 m electrode spacing and the L_1–norm (robust) inversions technique. The lacustrian sediments, peats and the scories are characterized by their resistivity ranges. Faults were also mapped on the profiles. The 2D imaging technique and the L_1–norm has proved to be an efficient combination in mapping the sediments and other crater related structures at the crater area.

A.2 Introduction

Maar craters are produced by phreatomagmatic explosion caused by the coming into contact of hot lava/magma with groundwater. The largest magmatic region of the West European Rift system is the Massif Central area which is made up of intraplate alkaline series. The Massif Central comprises of many individual volcanic provinces as shown in Figure A.2. On top of the horst overhanging the Limange basin is the Chaîne des Puys which consists of hundred young well-preserved volcanoes (Aubert et al., 1984; Villemant et al., 1980). The most northerly volcano of the main Chaîne des Puys is the Maar of Beaunit (Figure A.1) and the Puy Gonnard strombolian cone is located in the crater. The crater is 1.1 km in diameter at its widest point and the Ambène river flows across it and lying in a marshy plain. The crater is filled with 14 m of clay and beneath it lies 66 m of permeable scoria. A crescent of pyroclastic breccias borders nearly half of its north-eastern side. A recent hawaïte lava flow from the Puy Thiollet located about 1.5 km to the south covers the southern half of this structure (Aubert et al., 1984; Livet et al., 2000).

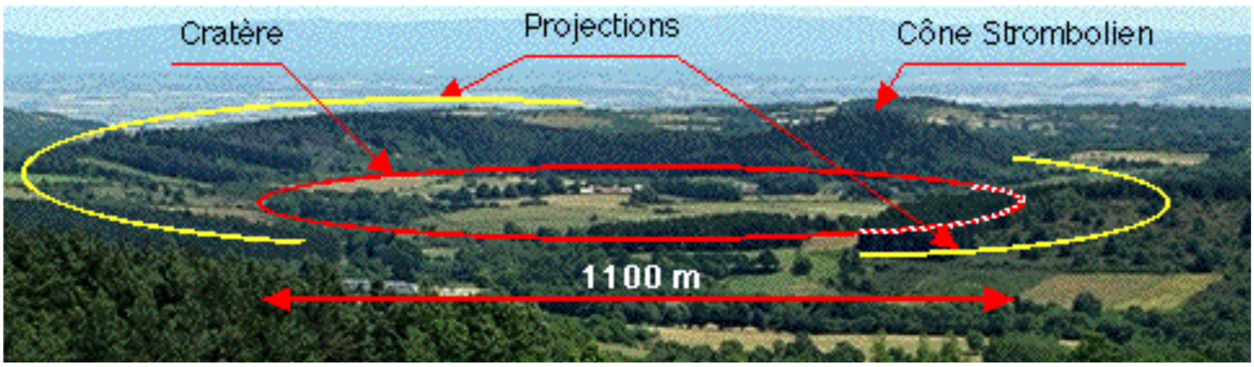

Figure A.1 – Beaunit crater

The order of events at the volcanic system at Beaunit is;

- formation of the maar
- strombolian activity, creating the Puy Gonnard immediately following the maar activity
- lacustrian sedimentation and
- lava flow from Puy Thiollet emission (Camus, 1975)

The objective of this study was to use the 2D Electrical resistivity tomography (ERT) technique to map the sediment and bedrock contact and any other volcanic related feature(s) at the maar of Beaunit. The successful delineation of the subsurface structures at the 1.1 km Beaunit volcanic cater which is a miniature of the 10.5 km Bosumtwi impact crater was thus very crucial for this thesis.

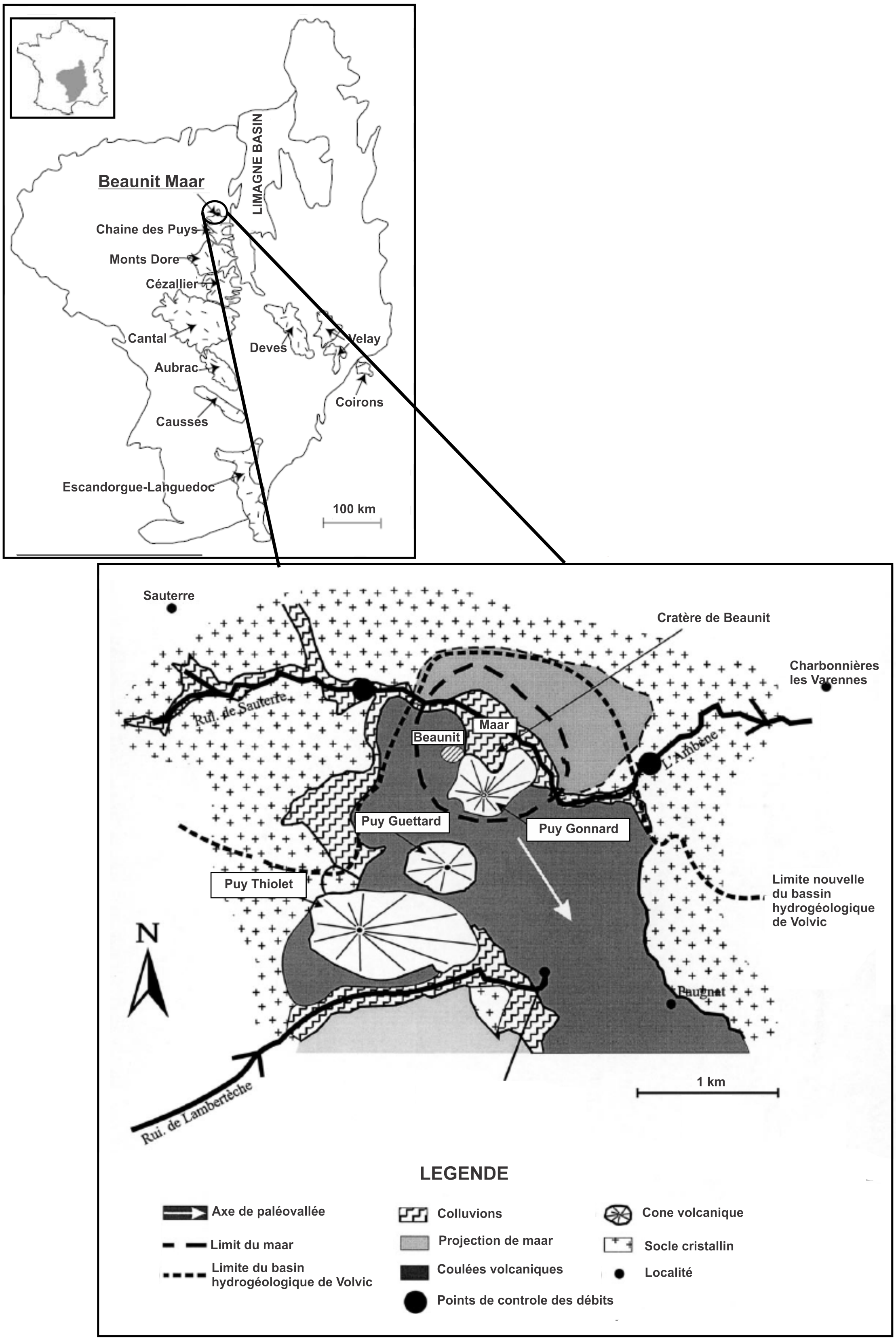

Figure A.2 – Location and geological map of maar of Beaunit, modified after (Livet et al., 2000) and (Jannot et al., 2005)

A.3 Methodology

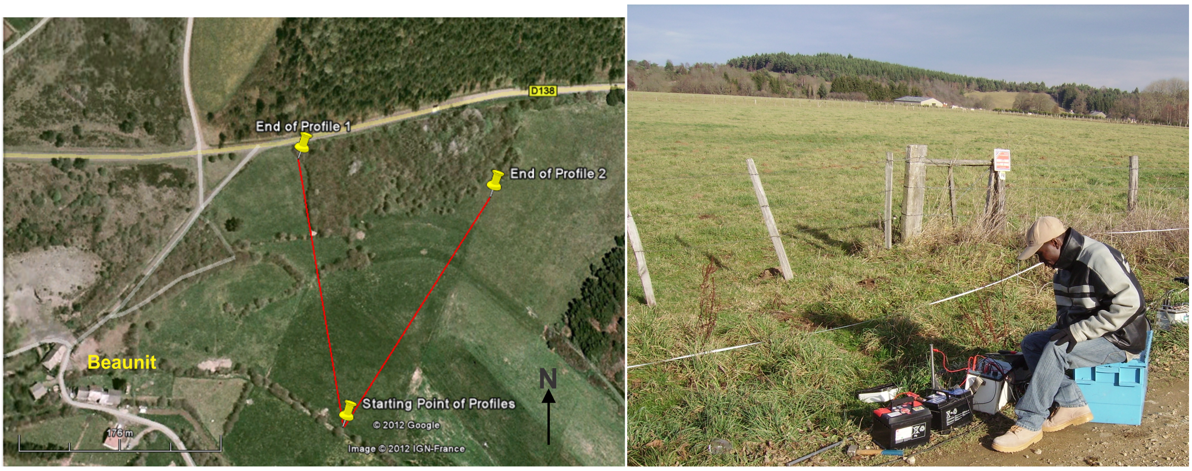

(a) (b)

Figure A.3 – 2D electrical resistivity image, (a) profile 1 and 2 and (b) set-up

The ERT has proven to be a very powerful technique in mapping shallow subsurface structures (Griffiths and Barker, 1993; Yang et al., 2002). The ERT is carried out by using two electrodes to inject current into the subsurface and measuring the resulting potential difference with two additional electrodes (Figure 4.4).

The ERT was performed using the SYSCAL R1 PLUS with the Wenner configuration. The data were collected using 48 electrodes and an electrode separation of 5 meters resulting in a profile length of 235 m. The system consisted of an information storage system, a switching unit to select the geometry of the arrays, three multinodes with 16 electrode connectors each, and a remote control multiplexer. The data were inverted using Res2dinv (version 3.59.03), and the L_1–norm (robust) inversions was used (Loke et al., 2003). The effect of topography was taken into account during the inversion because of significant changes in the elevation of the ground surface. For the details of the theory and methodology, the reader is kindly referred to Chapters 4 and 5.

A.4 Results and Discussion

The electrical resistivity tomographies display a variation of resistivity both horizontally and vertically showing that the subsurface rocks have different electrical properties resulting from their lithologies and the intensity of fracturing/faulting. Three distinctly different resistivity zones were distinguished on the two profiles: first the thin moderately high resistivity zone near the surface. This region with resistivity 150 Ωm $< \rho <$ 400 Ωm was interpreted as peat. Second, underlying this peat zone are the lacustrian sediments which have resistivities below 150 Ωm. The third zone is area getting to the end of the profiles with resistivities $>$ 400 Ωm, and which have been interpreted as scories (pyroclastics). The solid white lines on the images are the inferred faults.

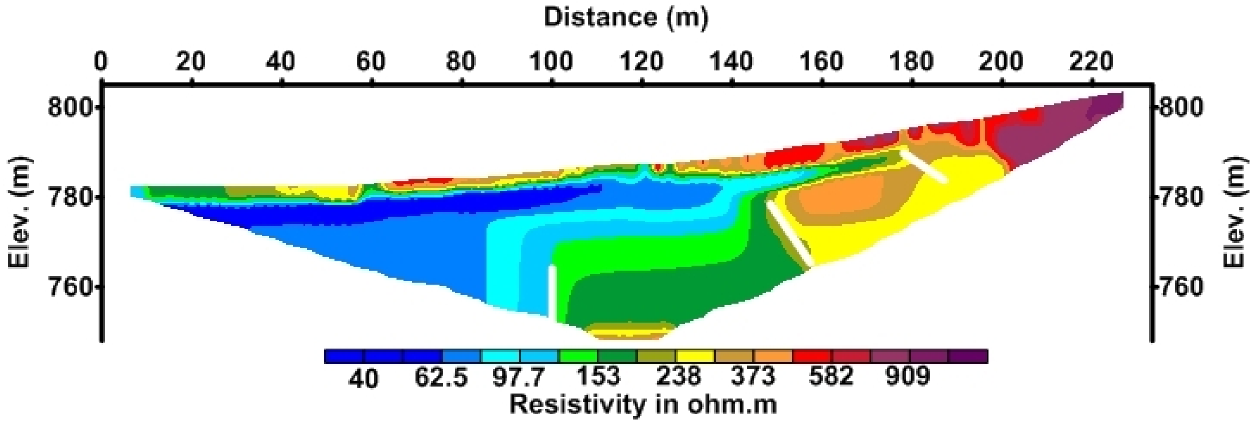

(a)

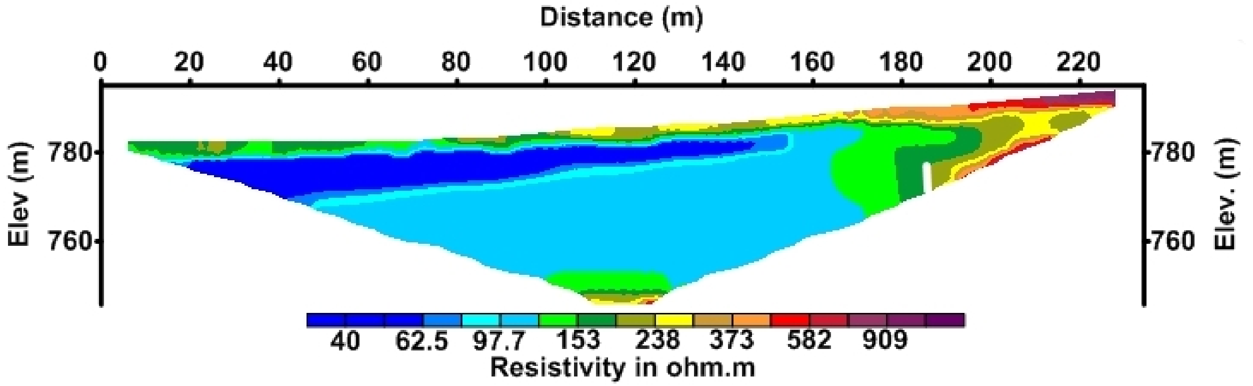

(b)

Figure A.4 – 2D electrical resistivity image, (a)profile 1 and (b)profile 2

A.5 Conclusion

2D electrical resistivity imaging survey has been carried out at the maar of Beaunit. The objective was to test the effectiveness of the electrical resistivity tomography in mapping the sediment/bedrock contact and other structures related to the crater in order to use the technique to study the Bosumtwi impact crater. At the site the resistivity method shows the low resistivity layers that was interpreted to be the lacustrian sediments. The resistivities of the sediments were lower than the overlying peats and the scories (pyroclastics) at the rim of the crater.

The results has shown that the ERT and the L_1–norm (robust) inversions techniques can play an important role in mapping the sediment and bedrock contact and other structures at crater sites.

Appendix B

B.1 Example of measurement setup files

Table B.1 – Converted .S4K file using GRAD4LX8 and GRAD4S8 gradient array protocols in .AMP file format

Filename: D: \lrboskon.s4k
Instrument ID: SAS4000 2082810
Date and Time: 22/12/2012 04: 39: 35
Base station: 0.00 0.00 0.00 0.00 0.00
Rows header/data/topography: 27 1298 0
Acquisition mode: 2
Measurement method: Section
Electrode layout: 15 Untitled Unt
Co-ordinate type: Index
Smallest electrode spacing: 5.00
Protocol ♯1: GRAD4LX8
Protocol ♯2: GRAD4S8
Operator: AKWASI ACHEAMPONG ANING
Client: PHD WORK
Comment ♯1: BOSUMTWI CRATER
Comment ♯2: KONKOMA

No.	Time	T_x	R_x	D_x	I (mA)	Voltage (V)	App. R. ($\Omega.m$)	Error (%)
1	712392	nan	nan	nan	200	0.031357	98.512098	0.004805
2	712392	nan	nan	nan	200	0.054873	86.732279	0.064470
3	712392	nan	nan	nan	200	0.054873	86.732279	0.006331
4	712392	nan	nan	nan	200	0.139899	74.166811	0.064470
5	712417	nan	nan	nan	200	0.012029	22.060817	0.491347
6	712417	nan	nan	nan	200	0.006565	57.748620	0.876056
7	712417	nan	nan	nan	200	0.009310	105.298393	0.970173
8	712417	nan	nan	nan	200	0.021399	109.299077	3.203418
9	712433	nan	nan	nan	200	0.006239	31.868002	0.891545
10	712433	nan	nan	nan	200	0.007815	88.390738	0.989743
11	712433	nan	nan	nan	200	0.014081	123.863756	1.797184
12	712433	nan	nan	nan	200	0.061374	112.561188	0.118694
13	712448	nan	nan	nan	200	0.034183	41.794354	0.000259

Continued on next page

Table B.1 – continued from previous page

No.	Time	T_x	R_x	D_x	I (mA)	Voltage (V)	App. R. ($\Omega.m$)	Error (%)
14	712448	nan	nan	nan	200	0.012449	73.001988	0.008578
15	712448	nan	nan	nan	200	0.013922	104.971519	0.220642
16	712448	nan	nan	nan	200	0.030748	104.700024	0.036050
17	712461	nan	nan	nan	200	0.015752	53.636115	0.019129
18	712461	nan	nan	nan	200	0.013405	101.069305	0.034521
19	712461	nan	nan	nan	200	0.017907	105.011160	0.119143
20	712461	nan	nan	nan	200	0.088397	108.080540	0.001505
.	.	.	.	.	.	.	.	.
.	.	.	.	.	.	.	.	.
.	.	.	.	.	.	.	.	.
1287	731531	nan	nan	nan	100	0.053664	91.365012	0.018992
1288	731531	nan	nan	nan	100	0.033152	124.979980	0.017985
1289	731531	nan	nan	nan	100	0.032232	94.510047	0.022247
1290	731531	nan	nan	nan	100	0.113504	69.389410	0.106487
1291	731543	nan	nan	nan	100	0.130244	79.622739	0.000000
1292	731543	nan	nan	nan	100	0.035638	104.494960	0.015731
1293	731543	nan	nan	nan	100	0.030879	116.409503	0.007167
1294	731543	nan	nan	nan	100	0.062429	106.288135	0.003125
1295	731554	nan	nan	nan	100	0.059342	101.032683	0.009857
1296	731554	nan	nan	nan	100	0.029860	112.570712	0.022053
1297	731554	nan	nan	nan	100	0.040099	117.575870	0.014129
1298	731554	nan	nan	nan	100	0.145469	88.930843	0.033101

Table B.2 – GRAD4LX8 and GRAD4S8 measurement log

Measurement order	Protocol name	File type	No. of measu- ments	Measurement station (x) (m)	Measurement station (y) (m)	Measurement station (z) (m)
0	GRAD4LX8.ORG	0	150	200.0	0.0	0.0
1	GRAD4S8.ORG	0	62	200.0	0.0	0.0
0	GRAD4LX8.UP	1	83	300.0	0.0	0.0
1	GRAD4S8.UP	1	40	300.0	0.0	0.0
0	GRAD4LX8.UP	1	83	400.0	0.0	0.0
1	GRAD4S8.UP	1	40	400.0	0.0	0.0
0	GRAD4LX8.UP	1	83	500.0	0.0	0.0
1	GRAD4S8.UP	1	40	500.0	0.0	0.0

Table B.3 – Converted .S4K file using GRAD4LX8 and GRAD4S8 gradient array protocols with topography

\FIELDW~\BOS\BOS1\lrboskon.s4k
5.000
11
15
Type of resistivity data (1=resistance, 0=resistivity)
0
1200
2
0

No. of Channels	Position of C_1 (m)	Elevation of C_1 (m)	Position of C_2 (m)	Elevation of C_2 (m)	Position of P_1 (m)	Elevation of P_1 (m)	Position of P_2 (m)	Elevation of P_2 (m)	Apparent Resistivity ($\Omega.m$)
4	0.000	100.000	50.000	103.000	5.000	100.000	10.000	100.000	15.716
4	10.000	100.000	60.000	105.000	15.000	100.000	20.000	100.000	15.225
4	15.000	100.000	65.000	106.500	20.000	100.000	25.000	100.000	14.083
.	.	.	.	.	.	.	.	.	.
.	.	.	.	.	.	.	.	.	.
.	.	.	.	.	.	.	.	.	.
4	180.000	139.000	480.000	210.000	360.000	199.000	390.000	202.000	105.426
4	190.000	143.000	490.000	210.000	370.000	200.000	400.000	204.000	114.708
4	200.000	146.000	500.000	210.000	380.000	201.000	410.000	206.000	123.460
4	0.000	100.000	330.000	189.000	80.000	110.000	250.000	163.000	84.616
4	10.000	100.000	340.000	192.000	90.000	113.000	260.000	166.000	78.156
4	20.000	100.000	350.000	195.000	100.000	115.000	270.000	170.000	87.236
4	30.000	101.000	360.000	199.000	110.000	117.000	280.000	173.000	90.430

Continued on next page

Table B.3 – continued from previous page

No. of Channels	Position of C_1 (m)	Elevation of C_1 (m)	Position of C_2 (m)	Elevation of C_2 (m)	Position of P_1 (m)	Elevation of P_1 (m)	Position of P_2 (m)	Elevation of P_2 (m)	Apparent Resistivity ($\Omega.m$)
4	40.000	102.000	370.000	200.000	120.000	120.000	290.000	176.000	95.634
4	50.000	103.000	380.000	201.000	130.000	123.000	300.000	179.000	98.708
.	.	.	.	.	.	.	.	.	.
.	.	.	.	.	.	.	.	.	.
.	.	.	.	.	.	.	.	.	.
4	100.000	115.000	460.000	212.000	260.000	166.000	300.000	179.000	127.030
4	120.000	120.000	480.000	210.000	280.000	173.000	320.000	185.000	135.260
4	130.000	123.000	490.000	210.000	290.000	176.000	330.000	189.000	134.290
4	140.000	126.000	500.000	210.000	300.000	179.000	340.000	192.000	136.500
0									
0									
0									
0									

Appendix C

C.1 Statistical tables

Table C.1 – Critical values of F for ν_1 and ν_2 degrees of freedom and 5% ($\alpha = 0.05$) level of significance. From (Davis, 2002)

dF	1	2	3	4	5	10	20	∞
15	4.54	3.68	3.29	3.06	2.90	2.54	2.33	2.25
16	4.49	3.63	3.24	3.01	2.85	2.49	2.28	2.19
17	4.45	3.59	3.20	2.96	2.81	2.45	2.23	2.15
18	4.41	3.55	3.16	2.93	2.77	2.41	2.19	2.11
19	4.38	3.52	3.13	2.90	2.74	2.38	2.16	2.07
20	4.35	3.49	3.10	2.87	2.71	2.35	2.12	2.04
21	4.32	3.47	3.07	2.84	2.68	2.32	2.10	2.01
22	4.30	3.44	3.05	2.82	2.66	2.30	2.07	1.98
23	4.28	3.42	3.03	2.80	2.64	2.27	2.05	1.96
24	4.26	3.40	3.01	2.78	2.62	2.25	2.03	1.94
25	4.24	3.39	2.99	2.76	2.60	2.24	2.01	1.92
30	4.17	3.32	2.92	2.69	2.53	2.16	1.93	1.84
100	3.94	3.09	2.70	2.46	2.31	1.93	1.68	1.57
∞	3.84	3.00	2.61	2.37	2.22	1.84	1.58	1.47

Table C.2 – Maximum likelihood estimates of the concentration parameter κ for calculated values of $\bar{R}$ (adapted from Batschelet, 1965; and Gumbel, Greenwood, and Durand 1953)

$\bar{R}$	κ	$\bar{R}$	κ	$\bar{R}$	κ
0.00	0.00000	0.35	0.74783	0.70	2.01363
.01	.02000	.36	.77241	.71	2.07685
.02	.04001	.37	.79730	.72	2.14359
.03	.06003	.38	.82253	.73	2.21425
.04	.08006	.39	.84812	.74	2.28930
.05	.10013	.40	.87408	.75	2.36930
.06	.12022	.41	.90043	.76	2.45490
.07	.14034	.42	.92720	.77	2.54686
.08	.16051	.43	.95440	.78	2.64613
.09	.18073	.44	.98207	.79	2.75383
.10	.20101	.45	1.01022	.80	2.87129
.11	.22134	.46	1.03889	.81	3.00020
.12	.24175	.47	1.06810	.82	3.14262
.13	.26223	.48	1.09788	.83	3.30114
.14	.28279	.49	1.12828	.84	3.47901
.15	.30344	.50	1.15932	.85	3.68041
.16	.32419	.51	1.19105	.86	3.91072
.17	.34503	.52	1.22350	.87	4.17703
.18	.36599	.53	1.25672	.88	4.48876
.19	.38707	.54	1.29077	.89	4.85871
.20	.40828	.55	1.32570	.90	5.3047
.21	.42962	.56	1.36156	.91	5.8522
.22	.45110	.57	1.39842	.92	6.5394
.23	.47273	.58	1.43635	.93	7.4257
.24	.49453	.59	1.47543	.94	8.6104
.25	.51649	.60	1.51574	.95	10.2716
.26	.53863	.61	1.55738	.96	12.7661
.27	.56097	.62	1.60044	.97	16.9266
.28	.58350	.63	1.64506	.98	25.2522
.29	.60625	.64	1.69134	.99	50.2421
.30	.62922	.65	1.73945	1.00	∞
.31	.65242	.66	1.78953		
.32	.67587	.67	1.84177		
.33	.69958	.68	1.89637		
.34	.72356	.69	1.95357		

Table C.3 – Critical values of $\bar{R}$ for Rayleigh's test for the presence of a preferred trend with Level of Significance, α. From Mardia (1972)

α	.10	.05	.025	.01
Sample size,				
n = 4	0.768	0.847	0.905	0.960
5	.677	.754	.816	.879
6	.618	.690	.753	.825
7	.572	.642	.702	.771
8	.535	.602	.660	.725
9	.504	.569	.624	.687
10	.478	.540	.594	.655
11	.456	.516	.567	.627
12	.437	.494	.544	.602
13	.420	.475	.524	.580
14	.405	.458	.505	.560
15	.391	.443	.489	.542
16	.379	.429	.474	.525
17	.367	.417	.460	.510
18	.357	.405	.447	.496
19	.348	.394	.436	.484
20	.339	.385	.425	.472
21	.331	.375	.415	.461
22	.323	.367	.405	.451
23	.316	.358	.397	.441
24	.309	.351	.389	.432
25	.303	.344	.381	.423
30	.277	.315	.348	.387
35	.256	.292	.323	.359
40	.240	.273	.302	.336
45	.226	.257	.285	.318
50	.214	.244	.270	.301

Appendix D

D.1 Used Softwares

- LaTeX : typesetting and layout
- Res2DINV: for data processing
- Golden Software Surfer 10 : for further data processing
- Golden Software Grapher 8 : for ploting of graphs
- Golden Software Didger 3 : for ploting of maps
- Corel Draw Suite X5: for drawings
- MapInfo Professional 10.5 : for ploting of maps
- Adobe Photoshop CS5: for making the background of the resistivity images transparent

Appendix E

RÉSUMÉ EN FRANÇAIS

E.1 Introduction

Le cratère d'impact de Bosumtwi (Figure E.1a) est localisé à 30 km au SE de Kumasi dans la région d'Ashanti du Ghana. De coordonnées géographiques (06° 30′ N, 01° 25′ O), ce cratère est le plus jeune (1,07 millions d'années) et le mieux préservé des 95 structures d'impacts terrestres observées avec une morphologie de cratère qui n'a subi aucune modification (Karp et al., 2002). Son diamètre bord-à-bord est de 10,5 km et il est presque complètement rempli par le lac Bosumtwi qui lui - même a un diamètre de 8,5 km et un profondeur maximum de 75 m (Scholz et al., 2002). Le cratère est entouré par une légère dépression circulaire irrégulière, ainsi que par un anneau externe légèrement surélevé.

L'origine du cratère Bosumtwi (Figure E.1b) était sujet à discussion pour Junner (1937) et Jones (1985a) car il manquait une bonne compréhension des cratères d'impact à cette époque (Bampo, 1963; Smit, 1964). Plusieurs hypothèses ont été avancées pour expliquer l'origine du cratère: Fergusson (1902) dément une origine volcanique, Kitson (1916) l'analyse comme un résultat de subsidence, Rohleder (1936) privilégie une explication endogénique (explosion) et, finalement, Maclaren (1931) est la première personne à proposer que le cratère soit un cratère d'impact.

Le champ d'éjectat de tektite de la Côte d'Ivoire associé au cratère d'impact Bosumtwi (Koeberl et al., 1997a) fut décrit pour la première fois par Lacroix (1934), et 35 ans plus tard, d'autres échantillons ont été trouvés ((Gentner, 1966; Saul, 1969). Des microtektites ont aussi été trouvées au larges des côtes ouest africaines (Glass, 1968; 1969) et mises en relation avec les textites trouvées à terre. La distribution géographique des forages en mer profonde au large des côtes ouest africaine (09° N - 15° S et 00° - 23° O) a été utilisée pour déterminer l'extension spatial du cône d'éjectat (Glass and Zwart, 1979; Glass et al., 1979; 1991), et la teneur en microtektite et sa distribution granulométrique a permis de prédire avec précision la taille de la source du cratère d'impact au lake Bosumtwi (Glass and Pizzuto, 1994; Glass et al., 1991).

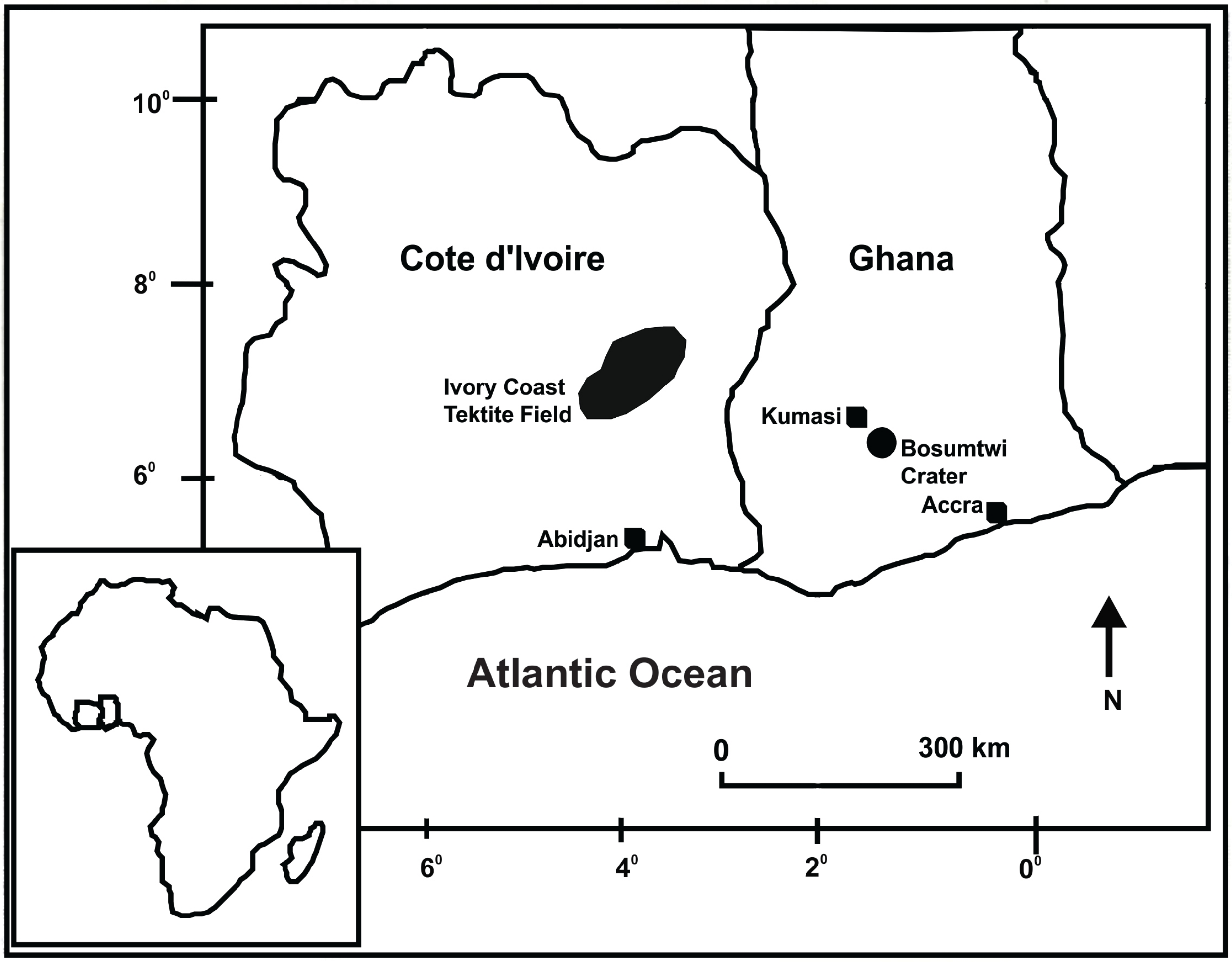

(a)

(b)

Figure E.1 – (a) Localisation du cratère d'impact de Bosumtwi impact en relation avec le champ de tektite de Côte d'Ivoire et (Koeberl et al., 1998) (b) vue panoramique (Koeberl and Reimold, 2005)

E.2 Géology and structure

Le cratère de Bosumtwi (Figure E.2) s'est creusé dans des roches supra-crustales à faciés shiste vert d'âge 2.1 à 2.2 milliard d'années, du groupe Birimien. Ces roches sont principalement métamorphiques d'origine sédimentaire et volcanique (Wright et al., 1985; Leube et al., 1990; Davis et al., 1994; Hirdes et al., 1996; Oberthür et al., 1998; Watkins et al., 1993; Koeberl and Reimold, 2005; Karikari et al., 2007; Coney et al., 2007a). Les roches du Birimien sont constituées de micaschiste et schiste en bande avec des couches de mica et de feldpaths quartziques, phyllite, metagrauwacke, quartzite et grès, slate ainsi que meta-tuffs. Les roches du Birimien d'origine

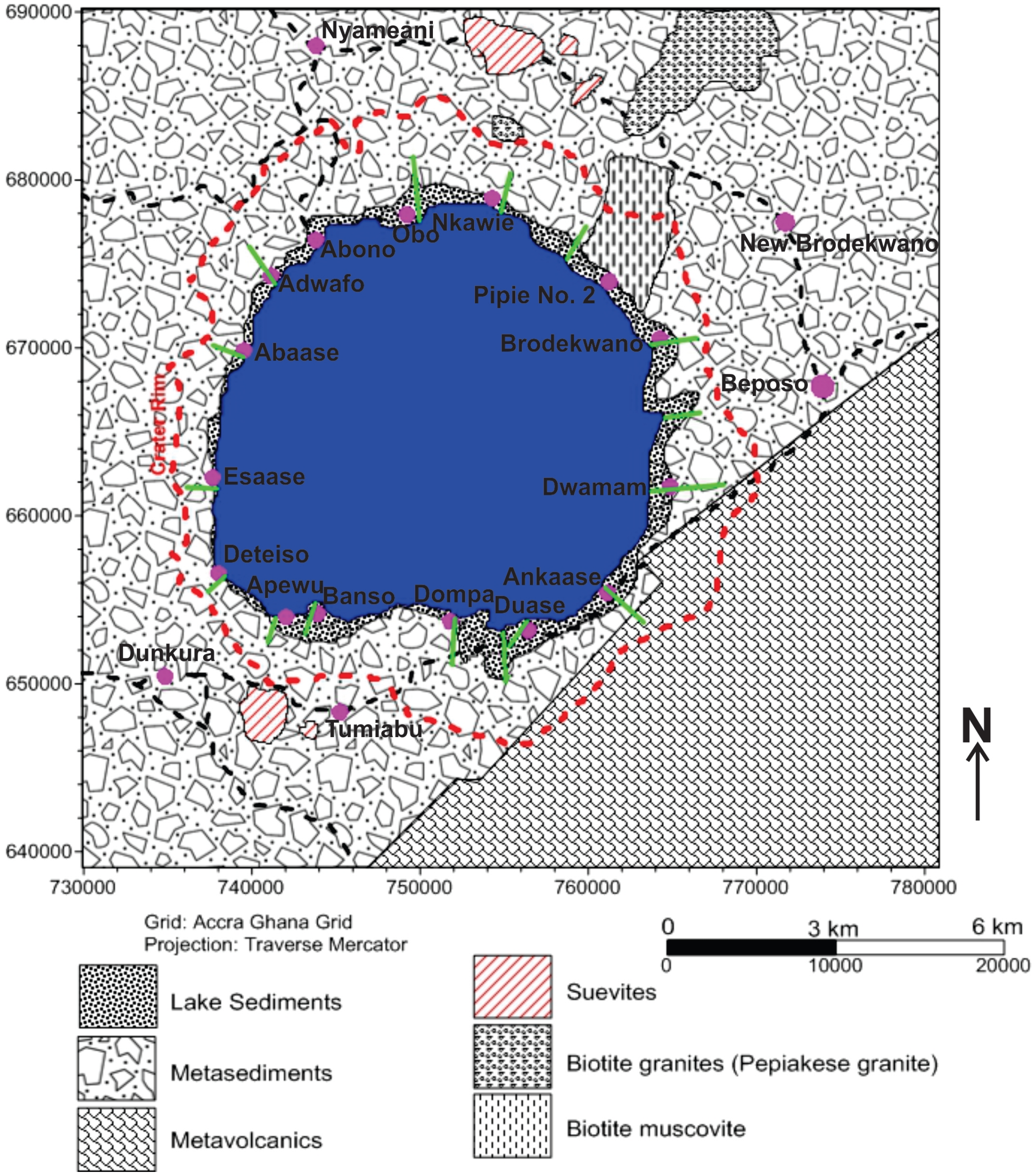

Figure E.2 – Carte géologique de Bosumtwi montrant la localisation des profils électriques en vert. Modifié à partir de (Koeberl and Reimold, 2005)

volcanique (roches intrusives basiques intercalées avec des méta-sédiments) sont présentes au SE du secteur de Bosumtwi. Le grauwacke prédomine sur les affleurements de surface et constitue l'élément le plus abondant dans les échantillons de Suévites. Des brèches à dominante de grauwacke et de phyllite sont présentes dans les régions proches du pourtour du cratère avec des intrusions granitiques (Junner, 1937; Moon and Mason, 1967; Reimold et al., 1998; Koeberl and Reimold, 2005).

Des roches carbonatées (calcite) inconnues ont été identifiées en abondance dans l'analyse de carotte de forage et leur origine est antérieure à l'impact (Coney et al., 2007a; Deutsch et al., 2007; Ferriére et al., 2007b). Le cratère a d'abord été interprété comme une caldera (Smit, 1964). Koeberl and Reimold (2005) a groupé les brèches de Bosumtwi en trois types basés sur leur composition et leur texture: autochtones (brèches monomictes), allochtones (brèches polymictes lithiques) et suévites qui sont uniquement au Nord et au Sud du cratère. Les suévites de Bosumtwi sont localisées dans une zone de 1,5 km^2 au Nord du cratère, environ à 2,5 km de la rive du lac 01° 23.5′ - 01° 24.5′ O et 06° 33.5′ - 06° 34.2′ N).

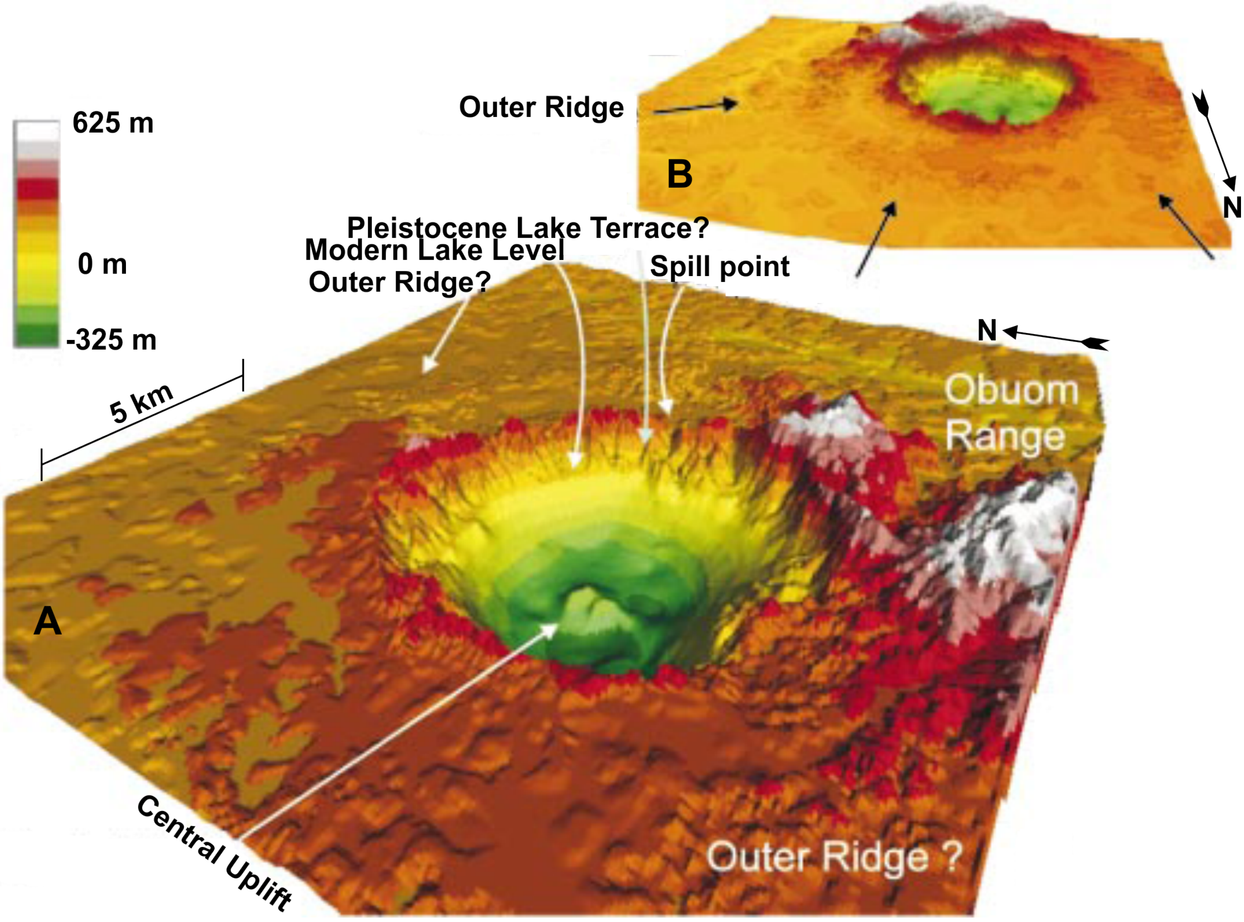

Figure E.3 – Modèle numérique de terrain du cratère d'impact de Bosumtwi, **(A)** éclairé par un soleil bas sur l'horizon pour mettre en évidence le point central haut, le point de rupture de pente, le lac actuel, et la terasse marquant la position du lac au Pleistocene, et **(B)** éclairé par un point haut pour mettre en évidence la rive externe du cratère (Scholz et al., 2002)

Des études géophysiques, des forages et des analyses de données satellites montrent que le cratère de Bosumtwi est une structure compliquée d'impact (Figure E.3). Le cratère présente un surélèvement central et est pratiquement rempli par le lac Bosumtwi de 8,5 km de diamètre et de profondeur maximum 75 m (Plado et al., 2000; Karp et al., 2002; Scholz et al., 2002; Wagner et al., 2002; Pesonen et al., 2003; Koeberl et al., 2005; Milkereit et al., 2006). Le lac a une morphologie simple en forme de bol, qui provient de l'accumulation de sédiments lacustres et alluvionnaires post-impact.

Les bord extérieurs du cratère s'élévent de 250 à 300 m au dessus du niveau de la surface du lac ce qui correspond à 80-100 m en dessous du terrain extérieur. Le cratère a une profondeur apparente d'environ 550 m (Koeberl and Reimold, 2005; Karp et al., 2002; Scholz et al., 2002; 2007). Figure E.3 montre les données du modèle numérique de terrain du cratère de Bosumtwi et de l'anneau externe d'environ 18 à 20 km de diamètre, qui peut être tracé depuis la chaine Obuom au Sud du lac. L'anneau externe a une altitude moyenne inférieure à 30 m et l'altitude de la surface cible est

150 m. L'épaisseur de roche brèche allochtone est d'environ 600 m dans la partie centrale. Le surèlevement central a une largeur de 1,9 km dans la direction NO-SE et une hauteur maximum de 130 m et est entourée d'un couche de sédiments lacustres post-impact d'environ 300 m. Cette partie surélevée a une surface irrégulière avec une petite structure de graben de 15 m de profondeur avec des failles qui s'étendent d'environ 120 m dans les sédiments. Cette partie est décentrée d'environ 1 km au nord du centre géométrique du cratère (Karp et al., 2002; Scholz et al., 2007).

E.3 Théorie and méthode

Les méthodes de mesures de résistivité électrique sont basées sur l'analyse de courants générés naturellement ou artificiellement dans le sol. Elles utilisent soit des courants continus (DC), soit du courant alternatif (AC) basse fréquence pour étudier les propriétés électriques du sous-sol. Elles sont basées sur la loi d'Ohm, qui contrôle le flux de courant dans un milieu conducteur. Il existe plusieurs géométries d'acquisition qui dépendent des arrangements et/ou de la séparation des électrodes : Wenner, Schlumberger, dipôle-dipôle, dipôle-pôle, pôle-pôle et les gradients. Pour une description détaillée des méthodes de résistivité, le lecteur est renvoyé à des sources telles que (Telford et al., 1990; Reynolds, 1997; Kearey et al., 2002; Milsom, 2003; Lowrie, 2007; Sharma, 1997) pour plus d'informations.

La tomographie électrique (TRE) est un système multi-électrodes où les électrodes sont équidistantes mais la distance entre les paires mesurant les différences de potentiel et celles mesurant le courant électrique varie en fonction de la configuration d'électrodes choisies. Les électrodes sont disposées sur une ligne et sont reliées par des cables à un multiplexeur puis à un résistivimètre. Le système enregistre l'intensité du courant électrique entre chaque paire d'électrodes correspondant à la différence de potentiel créé entre une autre paire d'électrodes de manière automatique. En prenant en compte les distances et les positions des électrodes, l'appareil en déduit une mesure de résistivité apparente au point milieu de chaque paire d'électrodes utilisées

Pour cette étude, nous avons utilisé un appareil de mesure de la marque ABEM LUND permettant l'installation de 4 lignes de 21 electrodes espacées de 2 m. Les mesures ont été faites avec les 4 lignes mises bout-à-bout, résultant en un profil de 160 m de long avec une profondeur d'investigation de 30 m. Pour allonger l'espacement entre les électrodes à 5 m, nous avons modifié les cables de connections ABEM nous -même (Figures E.4a and E.4b). Avec l'équipement modifié nous pouvons acquérir des profils de 400 m de long avec une profondeur d'investigation de 75 m. La longueur des cables ajoutés aux cables ABEM initiaux est détaillé dans les tableaux E.1 et E.2. Un enrouleur a été fabriqué pour une manipulation aisée des cables sur le terrain. Pour toutes les modifications (enrouleur et extension de cablage), je me suis appuyé sur mon expérience du système SYSCAL-R1 PLUS lors d'un travail de terrain sur le maar de Beaunit dans la chaîne des Puys en France.

Nous avons utilisé une configuration multi-electrodes avec mesure de gradient. Pour cela, les électrodes sont disposées en ligne avec un espacement a. La s-ième mesure de différence de potentiel se fait entre une paire d'électrodes espacées de la distance a, toujours située au milieu des deux électrodes utilisées pour injecter le courant électrique, espacées de la distance $(s + 2)a$. Les protocoles GRAD4LX8 (dispositif long) et GRAD4S8 (dispositif court) ont été utilisés. Pour GRAD4LX8, seulement une électrode sur deux est utilisé (l'espacement inter-électrode est donc de 10 m), comme montré sur les Figures E.4b and E.5b. Pour GRAD4S8, seules les 42 électrodes du milieu de profil sont utilisées avec un espacement de 5 m (Figures E.4a and E.5b).

Seize profils de tomographie électrique ont été acquis radialement autour du lac (Figure E.2), en montant des rives du lac jusqu'au bord du cratère. Les premières 21 électrodes (Cable 1) ne sont pas connectées pour le premier jeu de mesures. Le "terrameter" avec le sélectionneur d'électrodes ES 10-64C utilise les 31 électrodes du milieu de la ligne (Cables 2 et 3). Le système fonctionne grace à une batterie de voiture de 12 V. Un premier test de résistance de chaque électrode est fait pour s'assurer du bon montage (Figure E.5a). Dans quelques cas, les Ãľlectrodes doivent être arrosées avec de l'eau et renfoncer au marteau pour assurer un meilleur contact avec le sol pour permettre de passer le test de résistance. La même protocole est utilisé pour l'acquisition des longs profils avec GRAD4S8. Des tests utilisant seulement 41 électrodes espacées de 5 m (soit 200 m de profil) ont été faits avant les longs profils.

Table E.1 – Longueur rajoutées aux cables intérieurs 2 et 3

Prise de connection du cable 3	Prise de connection du cable 2	Distance inter-connections (m)	Position des l'électrodes (m)	Différence de longueur (m)	Vrai longueur (m)
1	21	0	0	0	0
2	20	2	5	3	4
3	19	4	10	6	7
4	18	6	15	9	10
5	17	8	20	12	13
6	16	10	25	15	16
7	15	12	30	18	19
8	14	14	35	21	22
9	13	16	40	24	25
10	12	18	45	27	28
11	11	20	50	30	31
12	10	22	55	33	34
13	9	24	60	36	37
14	8	26	65	39	40
15	7	28	70	42	43
16	6	30	75	45	46
17	5	32	80	48	49
18	4	34	85	51	52
19	3	36	90	54	55
20	2	38	95	57	58
21	1	40	100	60	61

Table E.2 – Longueur rajoutées aux cables extérieurs 1 et 4

Prise de connection du cable 4	Prise de connection du cable 1	Distance inter-connections (m)	Position des l'électrodes (m)	Différence de longueur (m)	Vrai longeur (m)
1	21	40	100	60	61
3	19	44	110	66	67
5	17	48	120	72	73
7	15	52	130	78	79
9	13	56	140	84	85
11	11	60	150	90	91
13	9	64	160	96	97
15	7	68	170	102	103
17	5	72	180	108	109
19	3	76	190	114	115
21	1	80	200	120	121

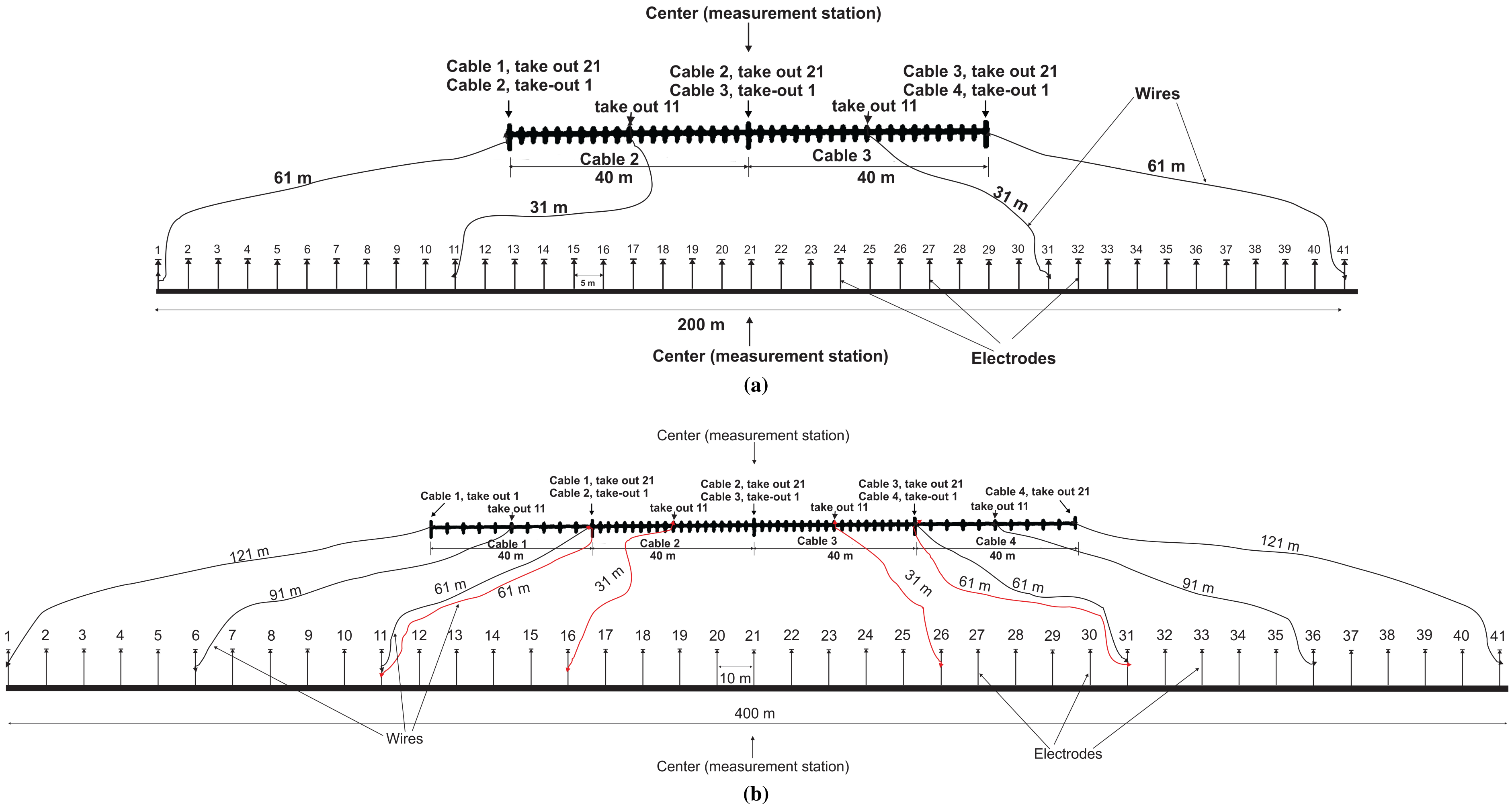

Figure E.4 – Schéma des connections pour (a) dispositif court (GRAD4S8) et (b) dispositif long (GRAD4LX8). Les cables en rouges sont utilisés dans les deux dispositifs

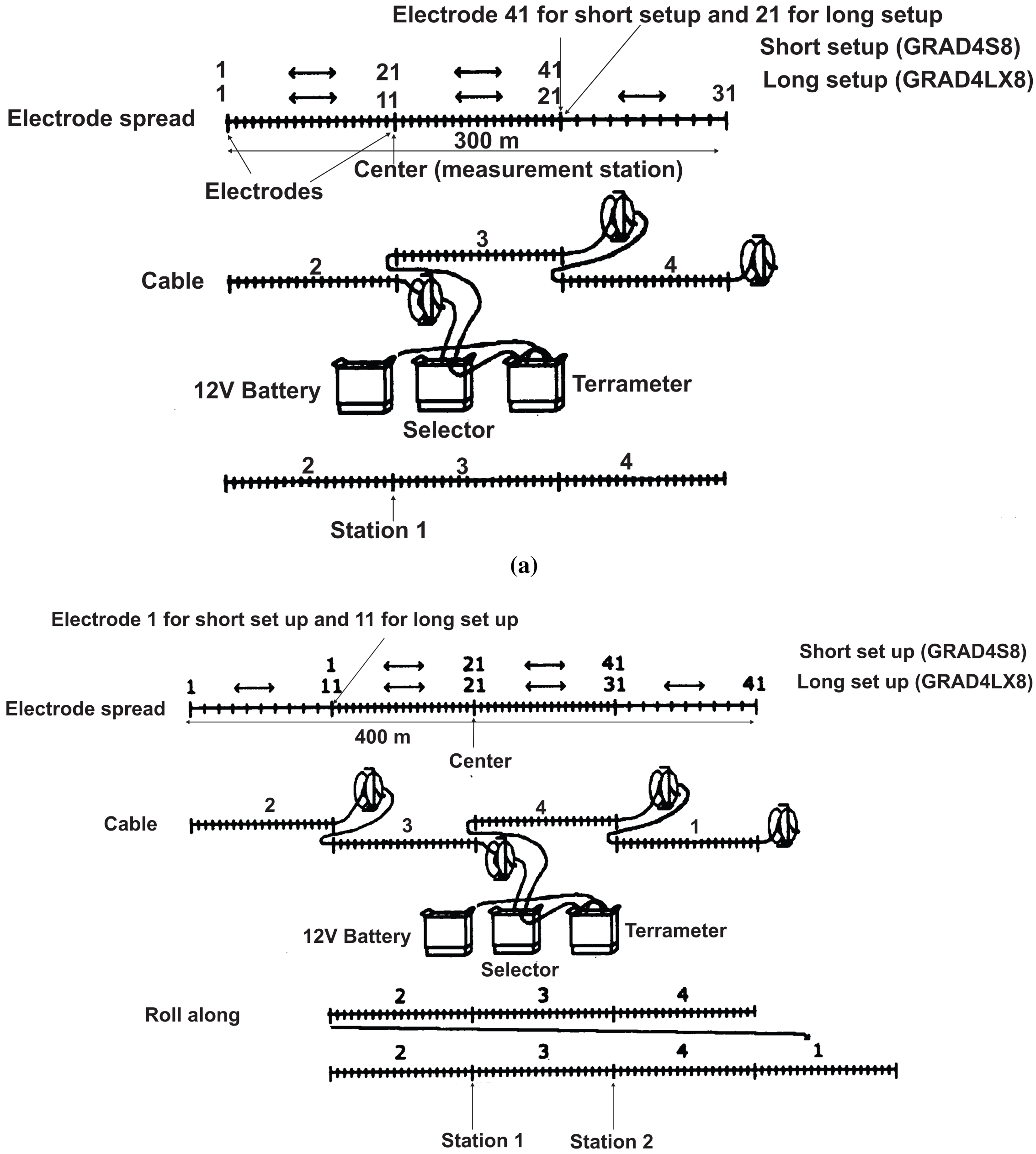

(b)

Figure E.5 – Schéma des connections pour (a) premier et (b) deuxième station de mesures. Modifié à partir de (ABEM, 2008)

La technique de "roll-along" (Figure E.5b) est employée sur les 16 profils pour les étendre horizontalement. Les cables modifiés ont compliqué un peu le protocole. Les cables 2 et 3 ont des extensions de longueur comprises entre 4 et 61 m (Table E.1) alors que les cables 1 et 4, externes, ont 11 extensions de longueurs comprises entre 61 et 121 m (Table E.2). À chaque rallongement de profil, il a donc fallu tout démonter pour le remonter dans l'alignement du profil précédent, vers le bord extérieur du cratère.

Le logiciel "Terrameter SAS4000/SAS1000" a été utilisé pour charger les données sur un ordinateur et les convertir au format lisible par RES2DINV (fichier .DAT) pour leur traitement, et à un format ABEM (ficher .AMP) pour la documentation. Les mesures négatives ont été effacées avant la conversion des données. Les mesures de topographie ont été ajoutées aux données. Les données ont alors été inversées en utilisant le logiciel Res2DInv (version 3.59.106) avec la norme L1 considéré plus robuste (Loke and Barker, 1996b; Loke, 2011; Loke and Barker, 1996a).

Les modèles de distribution de résistivité électrique obtenus par inversion ont mis en évidence des failles. Les coordonnées des failles interprétées sur chaque profil ont été enregistrées et l'utilisation de "Grapher " et "Surfer" ont permis leur visualisation en carte. Une méthode statistique pour déterminer la direction moyenne des failles trouvées et calculer les intervalle de confiance a été appliquée. Nous avons utilisé la distribution de von Misses et la statistique de Fisher car elles sont applicables pour étudier une distribution de vecteurs dispersés symétriquement autour d'un vecteur "vrai". Le traitement statistique de Fischer permet la détermination d'intervalles de confiance et la comparaison de direction moyenne et de dispersion (Davis, 2002; Butler, 1992).

E.4 Résultats and discussion

En utilisant la méthode de tomographie électrique (TRE), il a été possible de définir clairement l'étendue des sédiments lacustres post-impact ainsi que celle des limites du cratère sur chaque profil et délimiter d'autres discontinuités: les dikes, les brèches allochtones et parautochtones, les fractures et les failles, comme montrés sur la Figure E.6. Cette partie se concentre sur comment les discontinuités sont reliées, en les juxtaposant comme elles apparaissent au sein du cratère.

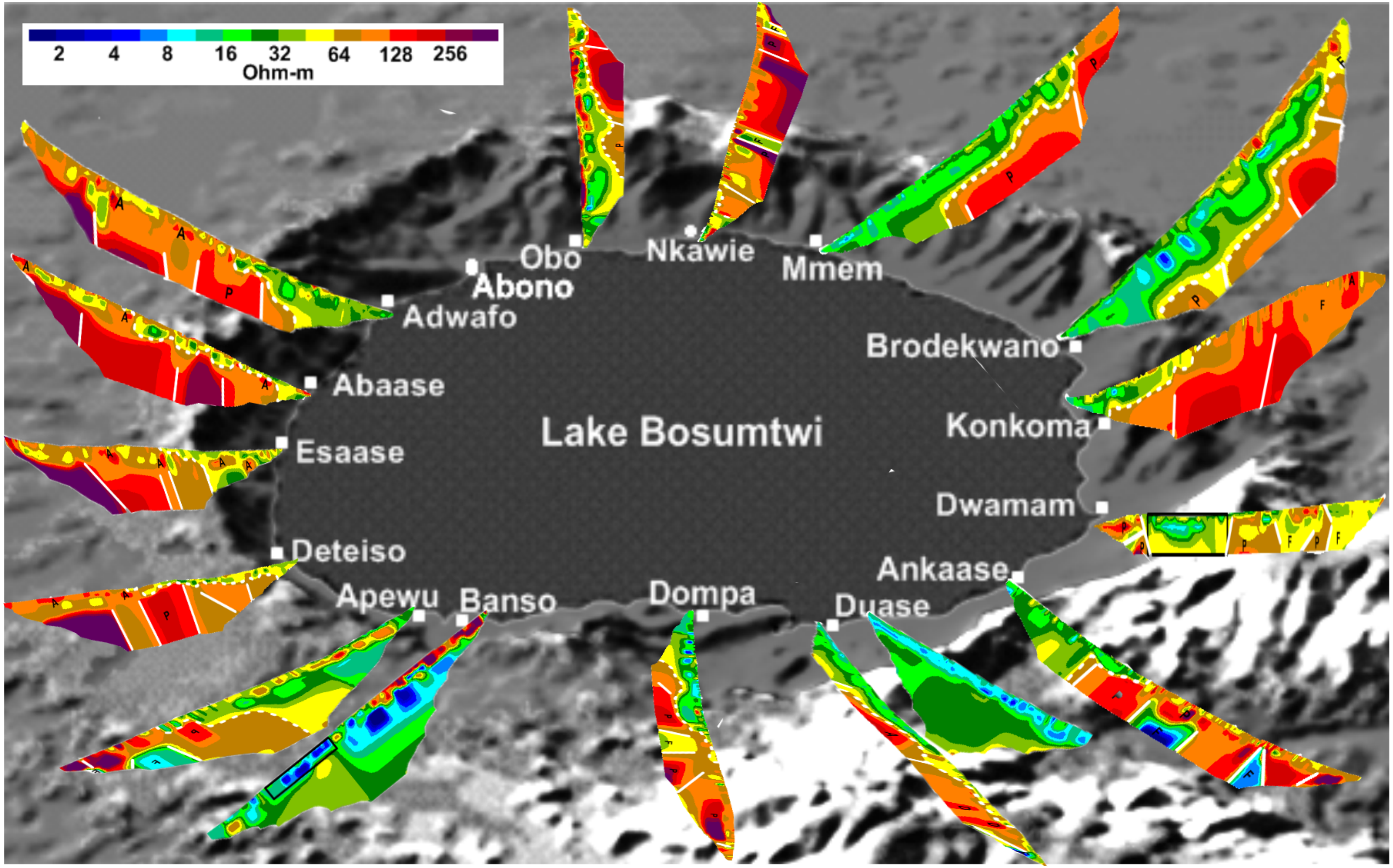

Figure E.6 – Le cratère d'impact de Bosumtwi avec les tomographies électriques

Pour tous les transects, les résultats montrent des zones de faible résistivité (< 64 Ω.m) entre la rive du lac et le bord du cratère. Ces zones, biens définies, sont interprétées comme étant les sédiments lacustres. Elles s'amincissent en remontant vers les bords du cratère. L'étendue des sédiments autour du lac est asymétrique (Figure E.6). Les portions à l'Est et au Sud étant plus larges et profondes, et celle de l'ouest étant la plus petite et la plus fine. Afin d'avoir une meilleur vision des limites sédimentaires autour du lac, le graphe X-Y fut converti en coordonnées polaires (Figure E.7). Attention, sur cette figure, le lac de 8.5 km de diamètre est résumé au point central du graphique pour ne montrer que la partie entre les rives du lac et le bord du cratère.

La pente intérieure est plus forte proche du bord et diminue doucement vers l'intérieur du lac dans la zones est et quelques parties de la zone méridionale, alors qu'au contraire elle est très forte dans la partie occidentale. La pente de l'interface sédiments/roche mère varie entre 16^{o} au NE, sa valeur la plus basse, et 36^{o} au SO, sa valeur la plus haute, comme présenté dans le tableau Table E.3.

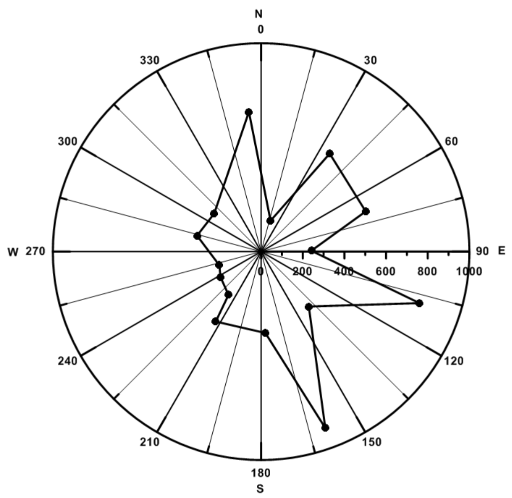

Figure E.7 – Représentation angulaire de l'extension des sédiments autour du centre du lac

Les zones de résistivité > 64 Ω.m, furent considérées comme la roche basale, composée de métagrauwackes, phyllites et slate. Tous les profils mais plus particulièrement celui de Dwamam montrent clairement les sédiments et la limite surfacique du cratère d'impact. Ils mettent aussi en lumière le fait que le pendage de la roche basale est la même que celle des sédiments. Toujours grâce au profil de resistivité de Dwaman, il apparaît de nombreux rejets et failles entre 200 et 500 m. Le fond de la zone a été bréchifié et faillé tout autour de ce dernier, cependant le degré de fracturation est plus faible dans la partie ouest du cratère.

La partie non bréchique de la subsurface (> 256 Ω.m) est remarquable dans la section ouest du cratère. Cela pourrait vouloir dire que le corps qui s'est écrasé obliquement (Artemieva et al., 2004) venait du nord-est ou de l'est et que le front des ondes de choc est en dessous de la limite de profondeur de détection des image de resisitivité 2D, qui est aux alentours de 75 m.

Cette zone de haute resistivité est clairement identifiable du nord au sud-ouest. Les profils de Nkawie, Obo, Adwafo et Abaase montrent des zones intéressantes: à approximativement 300 m de la rive du lac, on remarque une zone fortement électriquement résistante, que l'on retrouve à 200 m pour le profil d'Abaase. On remarque aussi la présence d'une zone de forte résistivité entre 400 et 500 m sur les profils de Nkawie, Obo et Adwafo, cependant avant 100 m pour ceux d'Adwafo et Obo, et inexistant sur toutes les images de Abaase. Se pourrait t'il que la portion soit faillée et affaisée comme dans le cas d'Adwafo et en dessous de la limite de résolution de l'appareil de résistivité? De plus, une autre ceinture de haute résistivité est visible sur les images de la fin du profil, il s'agit probablement de la même région de haute résistivité au delà des 300 m présente sur les transects de Esase et Deteiso. Ce n'est pas très visible sur le transect de Obo, mais pourrait être vu émergeant en dessous de 600 m.

La découverte de la symétrie bilatérale est essentielle pour la détermination de l'angle d'impact. Le gradient de la surface de la roche mère suit un modèle dont l'axe de symétrie est NE-SO, comme le tableau E.3 le montre. La partie nord et sa symétrie à l'est ont des valeurs de pendage de 19^o et 17^o respectivement, le NO et le SE ont une valeur de 19^o et 20^o, enfin l'est et le sud ont un pendage de 27^o et 25^o respectivement. Ces observations sont en parfait accords avec Artemieva et al. (2004) qui proposa que l'objet impactant provenait du N-NE.

Toutes les tomographies, exceptée celle de Banso, ont de fortes valeurs de rÃl'sistivités relatives, qui furent interprétées en tant que brèches, soit allochtones ou parautochtones, selon leurs géométrie et/ou leur extension latérale. Les éventuels dikes furent identifiés uniquement par leur géométrie sur le profil de Duase.

Hormis le profil de Banso, qui était dans les sédiments lacustres, des failles sont identifiées sur tous les profils (Figure E.6). En règle générale, les failles du coté ouest du cratère s'enfoncent à pic (quasi verticalement) contrairement à celles de l'est. Afin de relier les profils correctement en les juxtaposant, les données sont aussi présentées dans un graphe X-Y, X étant l'azimut et Y la distance radiale à partir du bord du lac. Les failles inverses (failles s'enfonçant en direction opposée du centre du cratère) furent cartographiées au Nord-Est, Sud-Est et Sud-Ouest. Une ligne de faille est présente aux alentours de 240 m sur les profils de Adwafo, Abaase et Esaase. Il s'agit probablement de la même faille en ligne formant une faille 'concentrique' dans la partie ouest et nord-ouest du cratère. Une autre de ces particularités est visible à 200 et 300 m sur les transects de Esaase et Deteiso ainsi que sur ceux de Deteiso et Apewu. Toutes ces failles pourrait être reliées en elles. Cependant, il n'y a aucune lien notable entre ces failles dans la partie est du cratère.

Table E.3 – Les pendages du contact sédiment/roche basale autour du cratère

Section du cratère	Pendage du contact sédiments/roche basale (^{o})
Nord-est	16
Est	17
Sud-est	20
Sud	25
Sud-ouest	36
Ouest	27
Nord-ouest	19
Nord	19

La distribution de von Mises et le coefficient de Fisher sont utilisés pour caractériser le pendage des failles identifiées dans les parties est et ouest du cratère (Table E.4). La valeur moyenne de la longueur résultante, $\bar{R}$ (la direction moyenne) et l'écart type, s_e, sont calculés. Les valeurs des paramètres de concentration du nuage de points, ont été estimés par détermination du maximum de la fonction de semblance (Davis, 2002). Les mesures de dispersion (test stochastiques) des valeurs de $\bar{R}$ est forte à l'ouest, ce qui indique que la direction des mesures dans cette section est très proche de la direction moyenne.

Direction moyenne et écart-type des failles

Table E.4 – Direction moyenne et écart-type des failles

Section du cratère	n	$\bar{\theta}$	R	$\bar{R}$	$\bar{R}_c$	κ	s_e
Est	10	60.33	9.32	0.93	0.54	7.43	6.85
Ouest	16	79.62	15.67	0.98	0.43	25.25	2.88

Table E.5 – Résultats des lignes de faille échantillonnées et combinées

Section du cratère	N	R_T	R_p	$\bar{R}_p$	κ	F_T	F_c
Est–Ouest	26	24.98	24.64	0.95	10.27	7.78	4.26

Les coefficients de Fisher sont utilisées pour la comparaison des deux directions moyennes (Est et Ouest). La valeur du coefficient de test, F_T, la longueur résultante R et la résultante normalisée par l'écart type $\bar{R}_p$, de l'ensemble des vecteurs sont aussi calculés (Davis, 2002). Les valeurs critiques F_c à 5% ont été estimées à partir du tableau de F-statistique.

A partir du Tableau E.5, la valeur F_T obtenue statistiquement n'est pas dans l'intervalle de confiance à 5%. Cela indique que les deux directions moyennes sont différentes. Des simulations numériques effectuées par Artemieva et al. (2004) suggérent que le cratère fut crée par un objet de dimension 0.75-1 km, ayant un vitesse de 15 kms^{-1} et qui s'écrasa avec un angle entre 30^o – 45^o du N-NE vers le S-SO.

L'interprétation des lignes de failles dans le cratère indique que l'objet venait du NE, car le maximum d'énergie (quantité de mouvement) se trouve dans la direction SO, cette portion du cratère étant très fortement faillée. La direction principale des failles nous permet de conclure quant à la direction des matériaux et renseigne sur le vecteur d'impact. L'analyse des pentes sur la roche mère permet aussi de conclure sur la provenance NE de l'objet.

E.5 Conclusion

La tomographie électrique a été utilisée avec succès à Bosumtwi pour cartographier à l'intérieur du cratère d'impact les limites sédiment / roche basale, et d'autres structures liées á l'inpact comme des brèches en dykes, autochtones, allochtones, des failles et des fractures. Seize profils ont été acquis radiallement des rives du lac vers les bords du cratère. Il s'agit de la première prospection géophysique de ce type effectuée dans cette région. Cette zone se divise en trois zones principales. D'abord, une zone de faible résistivité électrique (< 64 Ω.m) interprétée comme les sédiments lacustres. Puis une une zone de résistivité électrique moyenne (entre 128 et 200 Ω.m), interprétée comme des roches bréchiques liées à l'impact. Finalement un zone de haute résistivité (> 128 Ω.m) interprétée comme les roches métamorphiques. Les tomographies électriques ont aussi mis en évidence de nombreuses failles et fractures, surtout dans la zone SE du cratère. Des affleurements observés à Dwamam ont permis de confirmer l'interprétation des zones de faibles rÃl'sistivités comme des sédiments.

Le contact sédiments/roche basale n'est pas présent sur les profils acquis à l'est et au sud du cratère contrairement aux profils acquis au nord et à l'ouest. Il y a deux explications possibles: le contact est plus profond que la profondeur maximum d'investigation, et/ou, la zone de contact est trop fracturée et la résolution de la méthode électrique est insuffisante pour la détecter.

Quand il est détecté, ce contact présente un surface symétrique par rapport à un axe de direction NE-SO. Des failles concentriques, de pendage moyen entre 51^{o} et 80^{o}, ont été cartographiées sur les profils de l'ouest. Une analyse statistique a révélé que les directions moyennes des failles étaient différentes à l'est par rapport à l'ouest mais pouvaient se résumer à une direction moyenne.

La morphologie du contact sediment/roche basale, les directions de failles, la localisation des tektites de Côte d'Ivoire et les micro-tektites des forages de pleine mer indiquent que l'objet est arrivé probablement du NE.

E.6 Bibliography

ABEM, A. I. (2008). Instruction manual, Terrameter SAS4000/SAS1000.

Artemieva, N., Karp, T., and Milkereit, B. (2004). Investigating the Lake Bosumtwi impact structure: Insight from numerical modeling. Geochemistry, Geophysics and Geosystems: An Electronic Journal of the Earth Sciences, 5(11).

Bampo, S. O. (1963). Kumasi conference on the Lake Bosumtwi Crater. Nature, 198:1150–1151.

Butler, R. F. (1992). Paleomagnetism: Magnetic Domains to Geologic Terranes. Blackwell Science Publications.

Coney, L., Gibson, R. L., Reimold, W. U., and Koeberl, C. (2007a). Lithostratigraphic and petrographic analysis of ICDP drill core LB–07A, Bosumtwi Impact Structure, Ghana. Meteoritic and Planetary Science, 42(4/5):569–589.

Davis, D. W., Hirdes, W., Schaltegger, U., and Nunoo, E. A. (1994). Upb age constraints on deposition and provenance of Birimian and gold-bearing Tarkwaian sediments in Ghana, West Africa. Precambrian Research, 67:89–107.

Davis, J. C. (2002). Statistics and Data Analysis in Geology. John Wiley and Sons, 3rd edition edition.

Deutsch, A., Luetke, S., and Heinrich, V. (2007). The ICDP Lake Bosumtwi impact crater scientific drilling project (Ghana): Core LB–08A litho-log, related ejecta, and shock recovery experiments. Meteoritics and Planetary Science, 42(4/5):635–654.

Fergusson, M. (1902). Lake Bosumtwi. Geographical Journal, 19:370–372.

Ferriére, L., Koeberl, C., Reimold, W. U., and Mader, D. (2007b). Drill core LB–08A, Bosumtwi

Impact Structure, Ghana: Geochemistry of fallback breccia and basement samples from the central uplift. Meteoritics and Planetary Science, 42(4/5):689–708.

Gentner, W. (1966). Auf der Suche nach Kratergläsern, Tektiten und Meteoriten in Afrika. Naturwissenschaften, 12:285–289.

Glass, B. P. (1968). Glassy objects (microtektites?) from deep sea sediments near the Ivory Coast. Science, 161:891–893.

Glass, B. P. (1969). Chemical composition of Ivory Coast microtektites. Geochimica et Cosmochimica Acta, 33:1135–1147.

Glass, B. P., Kent, D. V., Schneider, D. A., and Tauxe, L. (1991). Ivory Coast microtektite strewn field: Description and relation to the Jaramillo geomagnetic event. Earth and Planetary Science Letters, 107:182–196.

Glass, B. P. and Pizzuto, J. E. (1994). Geographic variations in Australasian microtektite concentrations: Implications concerning the location and size of the source crater. Journal of Geophysical Research, 99:19075–19081.

Glass, B. P., Swincki, M. B., and Zwart, P. A. (1979). Australasian, Ivory Coast and North American tektite strewn field: Size, mass and correlation with geomagnetic reversals and other earth events. Proceedings of the 10th Lunar and Planetary Science Conference, pages 2535–2545.

Glass, B. P. and Zwart, P. A. (1979). The Ivory Coast microtektite strewn field: New data. Earth and Planetary Science Letters, 43:336–342.

Hirdes, W., Davis, D. W., Ludtke, G., and Konan, G. (1996). Two generations of Birimian (Paleoproterozoic) volcanic belts in northeastern Cote d'Ivoire (West Africa): Consequences for the–Birimian controversy. Precambrian Research, 80:173–191.

Jones, W. B. (1985a). Chemical analysis of Bosumtwi crater target rocks compared with Ivory Coast tektites. Geochimica et Cosmochimica Acta, 49:2569–2576.

Junner, N. R. (1937). The geology of the Bosumtwi caldera and surrounding country. Gold Coast Geological Survey Bulletin, 8:1–38.

Karp, T., Milkereit, B., Janle, P., Danuor, S. K., Pohl, J., Berckhemer, H., and Scholz, C. A. (2002). Seismic investigation of the Lake Bosumtwi impact crater: Preliminary results. Planetary and Space Science, 50:735âĂŞ743.

Kearey, P., Brooks, M., and Hill, I. (2002). An Introduction to Geophysical Exploration. Blackwell Science, 3rd edition edition.

Kitson, A. K. (1916). The Gold Coast: some consideration of its structure, people and natural history. Geographical Journal, 48:369–392.

Koeberl, C., Bottomley, R. J., Glass, B. P., and Storzer, D. (1997a). Geochemistry and age of Ivory Coast tektites and microtektites. Geochimica et Cosmochimica Acta, 61:1745–1772.

Koeberl, C. and Reimold, W. U. (2005). Bosumtwi Impact Crater, Ghana (West Africa): An updated and revised geological map, with explanations. Jahrbuch der Geologischen Bundesanstalt, 145(1):31–70.

Koeberl, C., Reimold, W. U., Blum, J. D., and Chamberlain, C. P. (1998). Petrology and geochemistry of target rocks from the Bosumtwi Impact Structure, Ghana, and comparison with Ivory Coast tektites. Geochimica et Cosmochimica Acta, 62:2179–2196.

Lacroix, A. (1934). Sur la découverte de tectites à la Côte d'Ivoire. Comptes Rendus Academie des Sciences Paris, 199:1539–1542.

Leube, A., Hirdes, W., Mauer, R., and Kesse, G. O. (1990). The early Proterozoic Birimian Supergroup of Ghana and some aspects of its associated gold mineralization. Precambrian Research, 46:139–165.

Loke, M. H. (2011). Tutorial: 2-D and 3-D Electrical Imaging Survey. Manual.

Loke, M. H. and Barker, R. D. (1996a). Practical techniques for 3D resistivity surveys and data inversion. Geophysical Prospecting, 44:499–523.

Loke, M. H. and Barker, R. D. (1996b). Rapid least-squares inversion of apparent resistivity pseudosections by a quasi-Newton method. Geophysical Prospecting, 44:131–152.

Lowrie, W. (2007). Fundamentals of Geophysics. Cambridge University Press, 2nd edition edition.
Lowry, T., Allen, M. B., and Shive, P. N. (1989). Singularity removal: A refinement of resistivity modeling techniques. Geophysics, 54(6):766–774.

Maclaren, M. (1931). Lake Bosumtwi, Ashanti. Geographical Journal, 78:270–276.

Milkereit, B., Ugalde, H., Karp, T., Scholz, C. A., Schmitt, D., Danuor, S. K., Artemieva, N., Kück, J., Qian, W., and L'Heureux, E. (2006). Exploring the Lake Bosumtwi crater–Geophysical surveys, predictions and drilling results (abstract No. 1687). In 37th Lunar and Planetary Science Conference. CD–ROM.

Milsom, J. (2003). Field Geophysics. The Geological Field Guide Series. John Wiley and Sons, 3rd edition edition.

Moon, P. A. and Mason, D. (1967). The geology of 1/4° field sheets 129 and 131, Bompata S.W and N.W. Ghana Geological Survey Bulletin, 31:1–51.

Oberthür, T., Vetter, U., Davis, D. W., and Amanor, J. A. (1998). Age constraints on gold mineralization and palaeoproterozoic crustal evolution in the Ashanti belt of southern Ghana. Precambrian Research, 89:129–143.

Plado, J., Pesonen, L. J., Koeberl, C., and Elo, S. (2000). The Bosumtwi meteorite impact structure, Ghana: A magnetic model. Meteoritic and Planetary Science, 35:723–732.

Reimold, W. U., Brandt, D., and Koeberl, C. (1998). Detailed structural analysis of the rim of a large, complex impact crater: Bosumtwi Crater, Ghana. Geology, 26(6):543–546.

Reynolds, J. M. (1997). An Introduction to Applied and Environmental Geophysics. John Wiley and Sons.

Rohleder, H. (1936). Lake Bosumtwi, Ashanti. Geographical Journal, 87:51–65.

Saul, J. M. (1969). Field investigations at Lake Bosumtwi (Ghana) and in the Ivory Coast tektite strewn field. National Geographic Society Research Reports, 1964 Proj:201–212.

Scholz, C. A., Karp, T., Brooks, K. M., Milkereit, B., Amoako, P. Y. O., and Arko, J. A. (2002). Pronounced central uplift identified in the Bosumtwi Impact Structure, Ghana, using multichannel seismic reflection data. Geology, 30:939–942.

Scholz, C. A., Karp, T., and Lyons, R. P. (2007). Structure and morphology of the Bosumtwi impact structure from seismic reflection data. Meteoritic and Planetary Science, 42(4/5):549–560.

Sharma, P. V. (1997). Environmental and Engineering Geophysics. Cambridge University Press.

Smit, A. F. J. (1964). Origin of Lake Bosumtwi (Ghana). Nature, 203:179–180.

Telford, W. M., Geldart, L. P., and Sheriff, R. E. (1990). Applied Geophysics. Cambridge University Press, 2nd edition edition.

Wagner, R., Reimold, W. U., and Brandt, D. (2002). Bosumtwi Impact Crater, Ghana: A remote sensing investigation. in Meteorite impacts in Precambrian shields. Impact Studies, Heidelberg: Springer-Verlag, 2:189–210.

Watkins, A. P., Iliffe, J. E., and Sharp, W. E. (1993). The effects of extensional and transpressional tectonics upon the development of the Birimian sedimentary facies in Ghana, W. Africa: Evidence from the Bomfa/Beposo District, near Konongo. Journal of African Earth Sciences, 17:457–478.

Wright, J. B., Hastings, D. A., Jones, W. B., and Williams, H. R. (1985). Geology and Mineral Resources of West Africa. Geology and Mineral Resources of West Africa. Allen and Unwin.